Surface Immobilization and Electrochemical Studies of Molecular Lanthanide and Actinide Complexes

By

Katie Jo Johnson

B.S. Biochemistry, University of Oklahoma, 2015

Submitted to the graduate degree program in Chemistry and the Graduate Faculty of the University of Kansas in partial fulfillment of the requirements for the degree of Master of Science.

Committee Members

_____

Dr. James D. Blakemore, Chair

_____

Dr. Kristin Bowman-James

_____

Dr. Mikhail V. Barybin

Date Defended: 03/27/2019

The Thesis Committee for Katie J. Johnson certifies that this is the approved version of the

following thesis:

Surface Immobilization and Electrochemical Studies of Molecular Lanthanide and Actinide Complexes

Committee Members

_____

Dr. James D. Blakemore, Chair

_____

Dr. Kristin Bowman-James

_____

Dr. Mikhail V. Barybin

Date Approved: 04/04/2019

Abstract

Due to their unique properties and emerging applications in materials, the chemistry of the lanthanides and actinides has become a thriving area of research. While much work has been done to probe the electronic, magnetic, luminescent, and catalytic properties of molecular lanthanide and actinide species, one area that has received less attention than it deserves is that of surface immobilization. The ability to successfully and selectively immobilize complexes on surfaces is crucial to the advancement of materials in fields such as sensor technologies, separations science, and catalysis. While most surface immobilized complexes contain *d*-block metals, this work focuses on the surface immobilization of complexes containing metals from the *f*-block.

While Chapter 1 serves as a broad overview of the field of surface immobilization, Chapter 2 of this thesis discusses the synthesis and characterization of four new tripodal lanthanide complexes (Ln = Ce, Nd, Sm, Eu) capable of undergoing immobilization on graphitic surfaces. Characterization by NMR and XPS support that these lanthanide complexes retain their molecular structure in solution and after immobilization. Electrochemical studies of the redox active cerium complex allowed for the surface stability and interfacial electron transfer rates of the immobilized complex to be directly quantified.

Chapter 3 of this thesis discusses the synthesis and characterization of two new molecular actinide species capable of noncovalent surface immobilization. Specifically, two new uranyl ($[UO_2]^{2+}$) complexes have been synthesized and characterized by methods such as NMR and XRD. Following immobilization, electrochemical methods were used to probe the immobilized properties of these uranyl complexes using the presence of the U(VI/V) redox couple. These complexes demonstrated enhanced surface stabilities compared to the tripodal lanthanide complexes, as well as high rates of interfacial electron transfer.

Table of Contents

List of Figures

List of Schemes

List of Tables

Abbreviations

Al   aluminum

An   actinide

BDD   boron-doped diamond

BE   binding energy

Ce   cerium

CH_3CN acetonitrile

CNTs   carbon nanotubes

Cp η^5-cyclopentadienyl, C_5H_5

CVD   chemical vapor deposition

CV   cyclic voltammetry

DCM   dichloromethane

DFT   density functional theory

DMF   dimethylformamide

DOE   Department of Energy

DOTA   1,4,7,10-tetraazadodecane-1,4,7,10-tetraacetic acid

DTPA   diethylenetriamine pentaacetate

EDTA   ethylenediaminetetraacetic acid

Eu	europium
$Fc^{+/0}$	ferrocenium/ferrocene redox couple
GC	glassy carbon
HLW	high-level waste
HOPG	highly oriented pyrolytic graphite
ILW	intermediate-level waste
IR	infrared spectroscopy
KB	ketjen black
KE	kinetic energy
k_{ET}	heterogeneous electron transfer rate
LLW	low-level waste
Ln	lanthanide
LTP	ligand tripodal *para*
LTO	ligand tripodal *ortho*
Mg	magnesium
MWCNTs	multi-walled carbon nanotubes
Nd	neodymium
NMR	nuclear magnetic resonance

NSF   National Science Foundation

PCAH   polycyclic aromatic hydrocarbon

Pt   platinum

RE   rare earth

Sm   samarium

SMM   single molecule magnet

SWCNTs   single-walled carbon nanotubes

TBAPF$_6$ tetra-butyl ammonium hexafluorophosphate

Th   thorium

TREN   tris(2-aminoethyl)amine

U   uranium

UO_2^{2+} uranyl cation

XAFS   X-ray absorption fine structure

XANES   X-ray absorption near edge structure

XP/XPS   X-ray photoelectron spectroscopy

XRD   X-ray diffraction

Chapter 1

Introduction

1.1 *An Overview of Surface Immobilization*

In recent years, surface immobilization has emerged as an effective strategy to probe various chemical, electronic, and physical properties of both surfaces and immobilized species. Utilizing spectroscopic and electrochemical techniques to interrogate immobilized species, researchers can gain valuable insights into the structure, surface area, conductivity, and electron transfer properties of an electrode surface. Additional information on the stability and the activity of the immobilized species can also be obtained through these methods, the importance of which is relevant to the study of catalysts, sensors, next-generation metal separations systems, and other applications. While a variety of surfaces have been used for immobilization studies, graphitic materials have attracted perhaps the most considerable interest in the past decade due to their unique structural and electronic properties and low cost.[1-4]

Although graphitic materials had been studied long before 2004 when Novoselov and Geim first reported the electrochemical properties of graphene,[5] fundamental innovations from recent work with graphene have led to the accelerated advancement of many disciplines that seek to utilize these materials for relevant applications.[6-8] Specifically, much work has focused on the understanding and development of the many different allotropes of carbon such as graphite, diamond, and fullerenes,[9] each of which can be used to synthesize a variety of materials that possess unique electronic and physical properties. Some examples of these materials are highly oriented pyrolytic graphite (HOPG),[1, 10] glassy carbon (GC),[11-12] carbon nanotubes (CNTs),[13-15] and boron doped diamond (BDD).[16-17] Despite the similarities in their elemental compositions, each of these materials possesses unique properties that tailor them for specific applications.[9, 18-19] For example, as a result of their wide potential windows in both aqueous and non-aqueous media, chemical inertness, and relatively low cost, carbon materials like HOPG and GC electrode

2

materials have been used for electrochemical studies since the late 1960s.[20-22] In recent years, the use of BDD electrodes has received considerable attention for applications in biosensor technologies and biocatalytic studies.[16, 23-24] Compared to HOPG and GC electrodes, BDD electrodes possess greater biocompatibility, increased resistivity to adsorption and electrode fouling, and increased sensitivity to trace concentrations.[17, 23, 25-26] Finally, CNT materials have been utilized as electrodes and similar materials, but also possess interesting conductive properties that make CNTs attractive for applications in supercapacitors, batteries, and photovoltaics.[27-30]

The ability to strategically modulate the various properties of carbon-based materials has received considerable interest in recent years.[31-33] While a number of excellent techniques have been developed for the chemical modification of carbon-based materials, such as p- and n-type doping[34-35] and chemical vapor deposition (CVD),[36-37] the focus of this chapter will be covalent and noncovalent functionalization techniques. Both covalent and noncovalent methods have been quite successful for a variety of applications and have received considerable attention in the literature as a result.[3, 33, 38-39] The most common methods for covalent functionalization of graphitic surfaces involve the formation of chemical bonds between the sp^2 hybridized carbon atoms present on the surface and free radicals or dienophiles.[1-2, 40] This method has proven advantageous for attaching various inorganic and organic functionalities onto graphitic surfaces, and enhanced surface stability of the attached functionalities is observed due to the presence of strong chemical bonds. However, the formation of chemical bonds between the surface and a given functionality leads to changes in the intrinsic properties of the surface material as a result of changes in hybridization from sp^2 to sp^3.[32] Additionally, harsh conditions are often necessary to achieve covalent functionalization and can cause unanticipated decomposition of the surface or

immobilized species.[41-42] Work to optimize the covalent functionalization of graphitic materials is ongoing and remedies to the challenges presented are still being pursued.[33, 43-44]

While covalent strategies rely on the formation of chemical bonds, non-covalent surface functionalization strategies are governed by the strength of the π interactions between a graphitic surface and a molecule of interest.[3, 45-46] While there are many different types of π interactions, such as H-π, cation-π, and anion-π, this work will focus on π-π stacking interactions in aromatic systems (**Scheme 1.1**).[47-51] These π-π stacking interactions are facile and reversible interactions that rely on quadrupole interactions among the delocalized electrons in π orbitals (**Scheme 1.2**).[47, 52-53] Aromatic systems are typically utilized to achieve these π-π stacking interactions; specifically, polycyclic aromatic hydrocarbons (PCAHs) such as anthracene, naphthalene, azulene, and pyrene have become popular for immobilizing functional moieties of interest onto graphitic surfaces.[3, 31, 54]

The work in this thesis will focus predominantly on the use of the pyrene moiety for the noncovalent surface immobilization of core molecular fragments onto carbonaceous surfaces. Due to its synthetic versatility and its ability to engage in strong π-π stacking interactions with a variety of graphitic surfaces, the pyrene moiety has become an effective means of achieving noncovalent surface immobilization.[55-58] Additionally, studies have shown that complexes appended with pyrene moieties display greater surface stabilities than those appended with other PCAH systems, such as phenanthrene or naphthalene, the details of which will be discussed later in this chapter.[59] For these reasons, the pyrene group has become an effective and popular strategy for immobilizing metal complexes,[43-44] molecular catalysts,[57, 60] and enzymes[61] onto graphitic surfaces
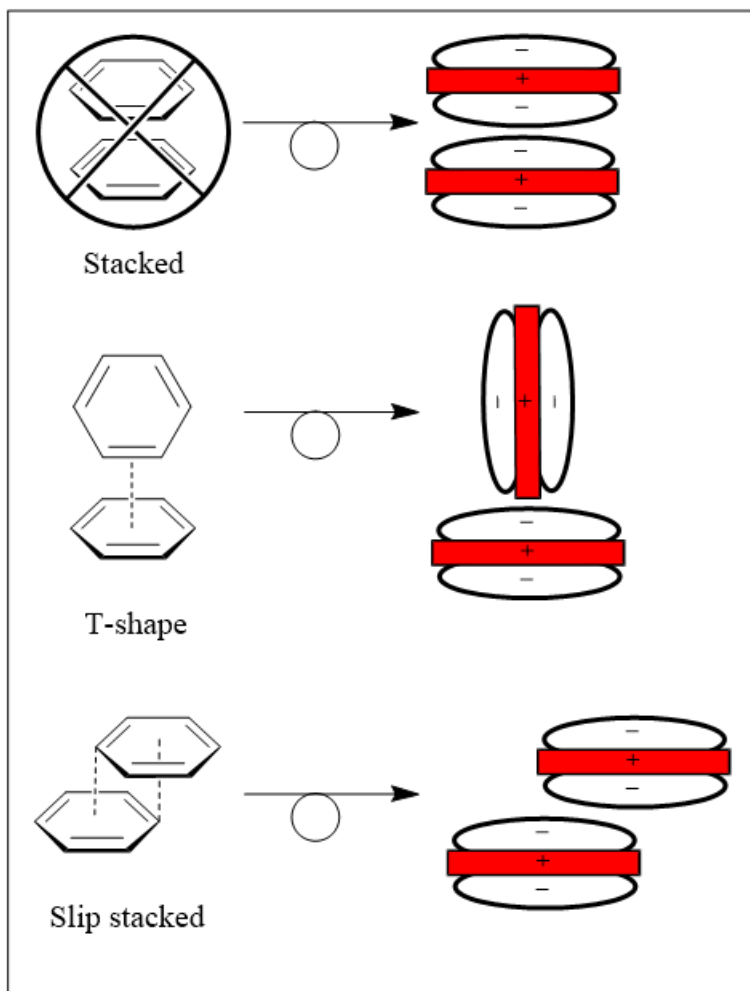
Scheme 1.1. Depiction of aromatic-aromatic interactions that give rise to π-π stacking geometries. Scheme adapted from reference 51.
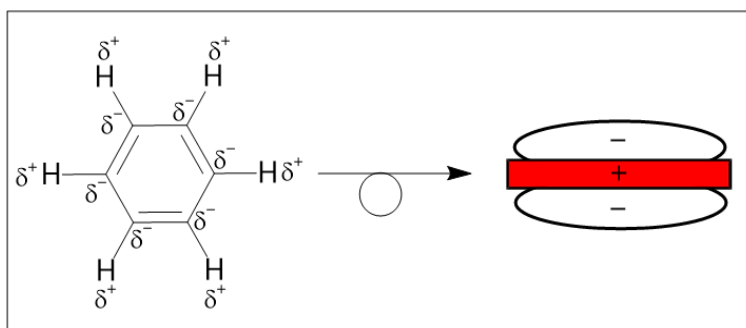
Scheme 1.2. Depiction of the relationship between the dipoles and quadrupoles of a benzene molecule. The six bond dipole moments of the benzene molecule give rise to a molecular quadrupole moment. Scheme adapted from reference 51.

1.2 *Applications and Studies of Noncovalent Surface Immobilization*

As a result of their ability to catalyze reactions related to organic transformations and small molecule activation, there have been many examples of surface-immobilized *d*-block metal complexes. The ability to immobilize a molecular catalyst onto a surface has several advantages that relate to catalytic activity and stability. The immobilization of an electrocatalyst onto an electrode surface can, in principle, promote faster electron transfer and higher catalytic activity by alleviating mass transport limitations.[62-63] By immobilizing an electrocatalyst onto the surface of an electrode, the performance of the system is no longer dependent on the diffusion of the electrocatalyst to the surface from the bulk solution, which can influence the overall rate of catalysis.[64] The ability to heterogenize molecular catalysts also holds considerable promise in industrial applications, where homogeneous catalytic processes are often plagued by difficult product separations. By attaching molecular catalysts onto solid supports, products, which are often formed in solution, can be easily removed from the catalyst without the use of distillation, filtration, or advanced chromatographic techniques.[65] Thus, one method of achieving surface immobilization that has received growing interest in the past decade is noncovalent surface immobilization. For example, the Artero and Jousselme groups examined a pyrene-appended nickel complex (**Scheme 1.3**) capable of performing hydrogen (H$_2$) evolution and H$_2$ oxidation.[66] Data obtained from X-ray photoelectron spectroscopy (XPS) and X-ray absorption near-edge structure (XANES) support the successful immobilization and molecular retention of the pyrene-appended
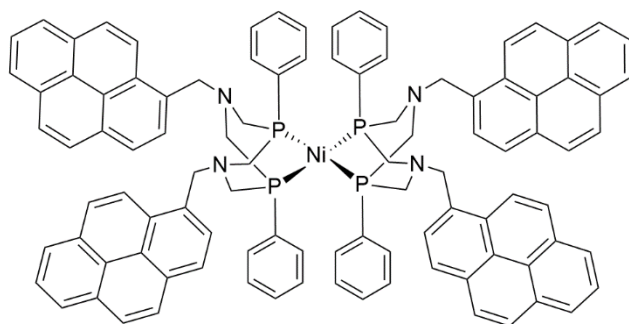
Scheme 1.3. Depiction of the pyrene-appended nickel complex studied by the Artero and Jousselme groups from reference 64.

6

nickel complex on multi-walled carbon nanotubes (MWCNTs). Electrocatalytic experiments of the pyrene appended nickel complex showed catalytic rates similar to analogous un-appended nickel complexes and a turnover number of 8.5×10^4 over a 6 hour period at modest overpotentials. In addition to H_2 evolution and H_2 oxidation catalysts,[67-68] much work has been carried out in the area of immobilization of molecular catalysts for the reduction of carbon dioxide (CO_2)[69-71] and oxygen (O_2),[58, 72] as well as the oxidation of water (H_2O).[57]

While significant advancements have been made to be able to successfully immobilize a variety of molecular catalysts using the pyrene moiety, there are still many challenges to overcome. Developing new methods to characterize catalytic mechanisms for immobilized species and understanding the driving forces of surface stability are two crucial areas that are necessary for continued progress in the field of surface immobilization. Homogeneous molecular catalysts are often advantageous for studying catalytic mechanisms due to a plethora of available spectroscopic techniques, such as NMR, IR, XANES, XAFS, XRD, and many others. These techniques can provide valuable mechanistic information related to a catalyst's kinetic and thermodynamic parameters, substrate and product selectivity, and catalytic efficiency.[65] The information obtained from these experiments is crucial to understanding, developing, and modulating molecular catalysts in order to improve their catalytic properties. However, once a molecular catalyst is immobilized onto a surface, the number of techniques available for mechanistic investigations become limited.[73] As a result of these limitations, many researchers often obtain the parameters for catalysis from a homogeneous model complex and then compare that data with the information obtained after the complex was immobilized.[71, 74-77] However, observed changes in the activity of the immobilized complex, such as catalytic enhancement or attenuation upon immobilization, cannot be sufficiently explained without spectroscopic evidence. Recent work in the field of

heterogeneous catalysis has focused on developing novel techniques to probe the mechanistic workings of an immobilized catalyst, such as transient absorption spectroscopy (TAS) investigations for catalysts immobilized on semiconductor materials.[76, 78-80] Additionally, density functional theory (DFT) has been implemented in numerous studies[81-83] to provide reasonable and compelling arguments about the mechanism and reactivity of heterogeneous catalytic materials.

Other challenges in the field of noncovalent surface immobilization utilizing pyrene are understanding the driving forces of surface stability in order to maintain long-term surface stability. Compared to the strength of the chemical bonds formed in covalent immobilization, the π-interactions between the surface and pyrene moiety are weaker.[3, 33, 84] As a result, catalysts immobilized using the pyrene moiety have often displayed limited surface stabilities,[57, 60, 85-86] a phenomenon that is not advantageous if such catalysts are to be developed for use on an industrial scale. To remedy the stability issues that revolve around noncovalent immobilization techniques, much work has focused on studying noncovalently immobilized metal complexes in order to gain more insight into the π-interactions between pyrene and a carbonaceous surface.

In addition to their prowess as molecular catalysts, many d-block metal complexes possess the ability to quickly and reversible undergo redox cycling. Many studies have utilized the electrochemical properties of various d-block metal complexes, such as their fast electron transfer rates and Nernstian electrochemical profile, as probes to examine various surface properties. By examining the electrochemical profile of these metal complexes when immobilized, information on a complex's heterogeneous electron transfer rate, adsorption thermodynamics, and desorption kinetics can be obtained. Each of these values have proven crucial to the understanding of surface immobilization and will be discussed in depth in later Chapters.

Some of the first detailed studies on the kinetic and thermodynamic binding parameters of aromatic systems on graphene were carried out by Dichtel and co-workers. Utilizing both tripodal and monopodal pyrene-appended Co *bis*-terpyridyl complexes ([Co(typ)$_2$]$^{n+}$) (**Scheme 1.4**) and cyclic voltammetry to probe a quasi-reversible Co(III/II) redox event, the Dichtel group was able to obtain crucial

Scheme 1.4. Depiction of the Co *bis*-terpyridyl complexes studied by the Dichtel group. Scheme adapted from reference 59.

information related to adsorption and electron transfer rates for an immobilized species.[55-56, 59] By utilizing the Langmuir isotherm model governed by the equation $\Gamma = \Gamma_s K c (K c + 1)^{-1}$ (where Γ is the surface loading, Γ_s is the saturation coverage, K is the equilibrium constant of binding, and c is the concentration of adsorbate in solution),[87] the free energy of adsorption (ΔG_{ads}) for the tripodal and the monopodal [Co(typ)$_2$]$^{2+}$ complexes was found for both to be around -9.3 kcal mol^{-1}.[59] In addition to probing the adsorption properties of the mono- and tripodal complexes, the Dichtel group also examined the desorption kinetics of these species utilizing cyclic voltammetry. By integrating the charge, Q, of the resulting Co(III/II) couple at designated time intervals, the surface coverage, Γ, could be calculated using the equation $\Gamma = Q(nFA)^{-1}$,[64] where n is the number of electrons, F is Faraday's constant, and A is the area of the electrode. The resulting plot of the data obtained from this analysis is shown in **Figure 1.1**. As one might expect, the tripodal Co complex has a significantly greater surface stability than that of the monopodal Co complex, suggesting that the presence of more pyrene groups leads to a greater surface stability. Finally, utilizing Laviron analysis,[88] which will be discussed in greater detail in Chapter 2, Dichtel

and co-workers were able to obtain heterogeneous electron transfer rate constants (k_{ET}) for both complexes as well: $k_{ET} = 13.5$ s^{-1} for the tripodal complex and $k_{ET} = 18$ s^{-1} for the monopodal complex.[59] The greater k_{ET} value obtained for the monopodal complex suggests that the Co metal center is in a closer proximity to the electrode surface than the tripodal complex. This interpretation is likely correct, as the heterogeneous electron transfer rate constant is a measurement of the rate of electron transfer between the electrode and the immobilized species. In comparison with the tripodal Co complex, the structure of the monopodal complex is slightly truncated due to the lack of the alkyne bridge, suggesting that the Co metal center of the monopodal complex could be in greater proximity to the surface of the electrode.

Figure 1.1. Plot of the fractional coverage (Γ) versus time for the monopodal (**2•3PF₆**, red) and tripodal (**1•2PF₆**, blue) complexes. Complexes were adsorbed onto graphene electrodes and then transferred into a blank electrolyte solution of 0.1 M NH₄PF₆ in THF. Resulting surface coverage was determined by integration of the Co(III/II) redox event to obtain charge, Q. Reprinted with permission from Mann, J. A.; Dichtel, W. R., *J. Am. Chem. Soc.* **2011,** *133*, 17614-17617. Copyright 2011 American Chemical Society.
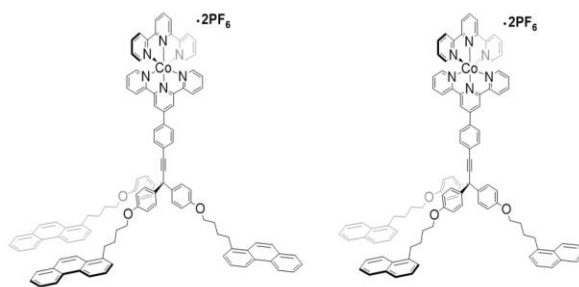
Scheme 1.5. Depiction of the phenanthrene (left) and naphthalene (right) appended Co complexes reported on by the Dichtel group in reference 56.

Later work from the Dichtel group sought to expand this family of Co complexes to study the properties of other PCAH-appended species. Complementing their work on pyrene, the Dichtel group also reported on the properties of analogous tripodal naphthalene- and phenanthrene-appended Co complexes (**Scheme 1.5**).[56] The adsorption properties of the naphthalene- and

phenanthrene-appended Co complexes were examined utilizing the same Langmuir isotherm model used in the earlier work done on pyrene.[87] Surprisingly, the free energies of adsorption for the pyrene-, naphthalene-, and phenanthrene-appended complexes all displayed roughly the same values for the free energies of adsorption ($\Delta G_{ads} \approx -9.3$ kcal mol^{-1}) (**Figure 1.2**). Despite the similarities in the free energy of adsorption for these complexes, there were significant differences in their surface coverages and stabilities. The resulting saturation coverages for the pyrene-, phenanthrene-, and naphthalene-appended complexes were 74 pmol cm^{-2}, 106 ± 6

Figure 1.2. Langmuir binding isotherms calculated from cyclic voltammetry measurements for surface coverage of all Co complexes at varying concentrations. The solution concentrations of the pyrene- (red), phenanthrene- (blue), and naphthalene-appended (yellow) tripodal Co complexes and the monopodal Co complex (purple) are plotted versus the coverage calculated from voltammetry measurements. All electrochemical experiments were run in 0.1 M NH$_4$PF$_6$ in THF and were performed in triplicated to determine error bars. Reprinted with permission from Mann, J. A.; Dichtel, W. R., *ACS Nano* **2013,** *7*, 7193-7199. Copyright 2013 American Chemical Society.

pmol cm^{-2}, and 114 ± 3 pmol cm^{-2} respectively. These values were calculated utilizing the previously mentioned equation, $\Gamma = \Gamma_s Kc(Kc + 1)^{-1}$, and the data obtained from the Langmuir isotherm analysis. The values obtained for the saturation coverage of the complexes show an inverse correlation between the size of the PCAH appendage and the surface coverage, where naphthalene would be expected to have the smallest footprint and largest surface coverage, pyrene the largest footprint and smallest surface coverage, and naphthalene somewhere in-between the two. Further investigation of these phenomena using cyclic voltammetry revealed a strong dependence on the size of the anchoring group and the surface stability of the complex. The reported desorption kinetics of these complexes shows that utilizing pyrene as an anchoring group

is advantageous over phenanthrene and naphthalene due to its ability to remain on the surface for longer time periods (**Figure 1.3**). This behavior was attributed to the size of the PCAH group and the ability for larger groups to achieve high surface-area contacts with a given surface in order to form stable monolayers.

While the work done by the Dichtel group has served as an important foundation for studying noncovalently immobilized species, many researchers have worked to expand beyond mono- and tripodal complexes to examine the properties of pyrene adsorption in added depth. Related work done by Haga, Ozawa, and co-workers[89-90] utilized a family of pyrene-appended ruthenium complexes

Figure 1.3. Plot of the fractional coverage (Γ/Γ_0) versus time for the family of Co complexes in reference 56. The pyrene- (red), phenanthrene- (blue), and naphthalene-appended (yellow) tripodal Co complexes and the monopodal Co complex (purple) are plotted. Complexes were adsorbed onto graphene electrodes and subsequently transferred into a blank electrolyte solution of 0.1 M NH_4PF_6 in THF. Cyclic voltammograms were taken at designated time intervals and resulting surface coverages were determined by integration of the Co(III/II) redox event. Reprinted with permission from Mann, J. A.; Dichtel, W. R., *ACS Nano* **2013,** *7*, 7193-7199. Copyright 2013 American Chemical Society.

(**Scheme 1.6**) to examine a variety of properties on highly oriented pyrolytic graphite (HOPG), single-walled carbon nanotubes (SWCNTs), and multi-walled carbon nanotubes (MWCNTs). Similar to the methods used by Dichtel and co-workers, a quasi-reversible Ru(III/II) redox couple was used as a means to extract pertinent electrochemical and thermodynamic parameters. Similar to the results observed in Dichtel's work, the desorption kinetics of the complexes revealed a direct relationship between the number of pyrene groups in the ruthenium complex and the resulting

Scheme 1.6. Depiction of the pyrene-appended Ru complexes synthesized by Haga, Ozawa, and co-workers from references 73 and 74.

surface stability (**Figure 1.4**). Complex **1** maintains nearly 60% of its surface coverage over the course of 10 hours while complex **2** maintains only 30%, and complexes **3** and **4** are completely lost to the solution after 8 hours and 30 minutes, respectively. These results directly correlated with the number of pyrene groups on each complex, supporting the conclusion that increasing the number of pyrene groups results in an increase in surface stability.

Additional electrochemical analysis of electrodes functionalized with these complexes examined the dependence of the heterogeneous electron transfer rate constants (k_{ET}) on the identity of the substrate material. Perhaps surprisingly, electrochemical determination of the heterogeneous electron transfer rate constants utilizing Laviron analysis[56, 59, 88] suggests a strong dependence on the subtrate (HOPG, MWCNTs, SWCNTs). The fastest calculated value for k_{ET} came
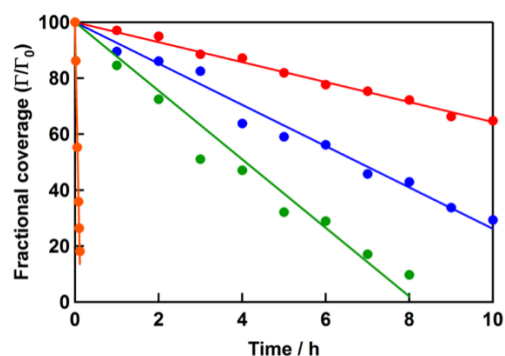
Figure 1.4. Desorption kinetics of the pyrene appended Ru complexes on HOPG electrodes. Complexes **1**, **2**, **3**, and **4** are color coded red, blue, green, and orange, respectively. To immobilize the Ru complexes, clean HOPG electrodes were submerged in 1 mM solution of a given complex and subsequently rinsed with neat solvent. Electrochemical experiments were performed in a solution of 0.1 M TBAPF$_6$ in CH$_3$CN. Reprinted with permission from . Kohmoto, M.; Ozawa, H.; Yang, L.; Hagio, T.; Matsunaga, M.; Haga, M.-a., *Langmuir* **2016**, *32*, 4141-4152.

13

from the studies done on basal plane HOPG (110 s^{-1}) followed by 14.9 s^{-1} for MWCNTs (tube diameter = 110-170 nm), 4.0 s^{-1} for MWCNTs (tube diameter = 6-9 nm), and finally 1.3 s^{-1} for SWCNTs. These k_{ET} values can be attributed to the intrinsic properties of the electrode materials. Of significance are the values measured for SWCNTs and MWCNTs considering the mesoscopic similarities between these two graphitic materials. The results from these studies have contributed valuable insights into the properties of graphitic materials and have been crucial to the understanding and the development of novel carbon nanomaterials utilizing noncovalent immobilization.

1.3 *Surface Immobilization of the f-Elements*

While there has been a steadily increasing number of reports of surface-immobilized *d*-block metal complexes over the years, there are very few reports of surface-immobilized molecular complexes of the *f*-elements. This observation is not completely surprising since *f*-element chemistry is still a maturing field that is rich in possibilities. From smartphones[91-92] and catalysts[93-95] to magnets[96-97] and medical applications,[98-99] *f*-block elements have served as important building-blocks for modern technological advances. The unique electronic,[100-101] magnetic,[96, 102] and structural[103-105] properties of the *f*-elements, which will be discussed in greater depth in Chapter 2, coupled with their broad applications in materials has prompted an interest in the idea of immobilizing *f*-element complexes on surfaces. The ability to immobilize and study complexes of the *f*-elements onto surfaces avoids the need for liquid solution and has the potential to advance the development of magnetic materials,[106-107] molecular sensors,[101, 108-109] and even lanthanide (Ln) and actinide (An) separations technologies.[110-112]

In recent years, covalent methods have become an increasingly popular way to immobilize *f*-elements on surfaces.[101, 113-114] Functionalization of silicon (Si), silver (Ag), and gold (Au) nanoparticles (NPs) with calixarenes, dendrimers, tripodands, or tetraazamacrocycles has been especially successful in the fields of Ln/An separations,[110, 115] biosensor technologies,[108, 113, 116] and luminescent materials (**Scheme 1.7**).[110, 115, 117-120] By comparison, there are far fewer examples of immobilized *f*-elements utilizing noncovalent methods. A notable early example of a pyrene-appended lanthanide compound was a Tb(III) complex that was examined as a single molecular magnet (SMM) by the Ruben and Bogani groups (**Scheme 1.8**).[106] Noncovalent immobilization was chosen for this work due to the fact that the Tb(III) complex was to be immobilized on SWCNTs. As discussed previously, covalent methods often perturb the intrinsic properties of a surface due to resulting changes in hybridization of the surface atoms caused by the formation of chemical bonds. Using noncovalent immobilization, the electronic properties of the SWCNTs remained intact, and immobilization

Scheme 1.7. Schematic representation of two systems used to immobilize lanthanide and actinide ions. Complex **1** is an adaptation from reference 102 and was probed as a new type of lanthanide luminescent material immobilized on mesoporous silica nanoparticles (SiNPs). The ligand in compound **2** is of the 2,9-bis(1,2,4-triazin-3-yl)-1,10-phenanthroline (BTPhen) family from reference 94. Ligands of the BTPhen family have shown promising properties for separations in liquid-liquid extraction studies with lanthanide and actinide species. Recent work discussed in reference 99 has focused on attaching these ligands onto solid supports.

Scheme 1.8. Schematic representation of the Tb(III) complex synthesized by the Ruben and Bogani groups from reference 90.

of the Tb(III) SMM complex could be achieved without harsh conditions that could lead to decomposition of the complex. The SWCNTs were functionalized with the Tb(III) complex by sonicating the SWCNTs in a solution of the complex overnight. The authors used transmission electron microscopy (TEM), energy-dispersive X-ray (EDX) spectroscopy, and atomic force microscopy (AFM) to probe the surface of the SWCNTs before and after functionalization with the Tb(III) complex. The combined methods showed excellent agreement with one another and indicated that, on average, one molecule of the Tb(III) complex was present per 7-8 nm of SWCNT length and the complex maintains its molecular integrity upon immobilization. To analyze the Tb(III) complex's magnetic properties, micro-SQUID experiments were done on the complex in solution and after functionalization on the SWCNT surface. The results of these experiments demonstrated that the magnetic properties of the Tb(III) complex are retained and even improved after immobilization. While this work represents an important step forward for the application of noncovalent surface immobilization in *f*-element science, much work remains in order to address the potential challenges related to the surface stability of such complexes. Recently, Blakemore and co-workers have reported a family of molecular lanthanide complexes capable of noncovalent immobilization using the pyrene moiety, the results of which will be discussed in greater detail in Chapter 2.[121] Additionally, recent work has focused exclusively on lanthanide-containing complexes, leaving the possibility of immobilizing actinide-containing species completely unexplored.

1.4 *Concluding Remarks*

In recent years, many researchers have devoted significant effort to understanding and improving surface immobilization techniques to meet the needs of various disciplines. Much work has focused on the development of novel, immobilized catalysts that can perform catalysis at enhanced rates while allowing for facile product separation. Other efforts have focused on utilizing surface immobilized species as probes for studying the properties of various graphitic surfaces. Within the field of noncovalent immobilization, much work has focused on understanding the strength and stability of the π-type interactions between a surface and a complex of interest. The insights provided by these studies have served as crucial foundations for applications in industrial and materials sciences.

d-block metal complexes have almost exclusively been used in surface immobilization studies due to their well-known catalytic properties along with the ability for some *d*-metals to reversibly redox cycle. The information obtained from the study of immobilized *d*-metal complexes has inspired our efforts in expansion of the field into studies of immobilized *f*-block metal complexes. The elements of the *f*-block have numerous intriguing properties that researchers are still seeking to understand, such as molecular magnetism and luminescence. Thus, the many applications of the *f*-block elements in everyday life motivate studies of surface immobilization, as the field of *f*-element chemistry is still in its adolescence.

1.5 *Thesis*

This thesis discusses the noncovalent surface immobilization of molecular lanthanide and actinide complexes. The first chapter of this thesis has already highlighted the opportunities and challenges of using noncovalent surface immobilization, by reviewing prior work that serves as an important foundation for examining immobilized species. Many studies discussed in Chapter 1, such as the work from the Dichtel,[56, 59] Haga,[89-90] and Ozawa groups,[89-90] have been crucial to the understanding, development, and interpretation of the work that will be discussed in Chapters 2 and 3.

The second chapter of this thesis discusses the synthesis and characterization of novel tripodal lanthanide complexes for immobilization onto graphitic surfaces. In recent years, much work has been done to immobilize lanthanide-containing complexes onto solid supports to enable incorporation of these complexes into materials. While there are many examples of lanthanide-containing species immobilized by covalent attachment methods, noncovalent methods have received less attention than it deserves. This work has been motivated by the observation that there are few examples of molecular lanthanide complexes immobilized by noncovalent methods; specifically, there are limited reports of lanthanide complexes immobilized on conducting substrates, such as graphene. The use of such substrates enables collection of electrochemical data, and such studies will form an important component of the work described in Chapter 2.

The work in Chapter 3 was motivated by the desire to develop immobilized molecular frameworks for the selective extraction of actinides from lanthanides. Discussed in Chapter 3 is the synthesis and characterization of two new uranyl ($[UO_2]^{2+}$) complexes capable of noncovalent immobilization on a graphitic surface. To our knowledge, these complexes are the first molecular uranium-containing complexes capable of noncovalent surface immobilization. These complexes

18

also have little company within field of surface immobilization, as there are no examples of immobilized molecular uranium complexes in the literature. Given this, the work in Chapter 3 provides the groundwork for new, exploratory chemistry that has possible relevance to nuclear waste separation and remediation technologies. Electrochemical work in Chapter 3 examines the properties of the immobilized uranyl complex using the well-known U(VI/V) redox couple as a probe. The electrochemistry of uranyl complexes has been of considerable interest in the field of *f*-element chemistry for quite some time and potentially hold valuable information for future work in U—O bond activation.

Chapter 4 of this thesis serves as a summary chapter and discusses selected results and insights obtained from Chapters 2 and 3. Additionally, Chapter 4 of this thesis discusses ongoing and future work related to the projects presented in Chapters 2 and 3. Specifically, Chapter 4 briefly discusses future experiments for the lanthanide and actinide projects in Chapters 2 and 3, as well as some preliminary spectroscopic data of a new U(IV) complex.

1.6 *References*

1. Ambrosi, A.; Chua, C. K.; Bonanni, A.; Pumera, M., *Chem. Rev.* **2014,** *114*, 7150-7188.

2. Pumera, M., *Chem. Soc. Rev.* **2010,** *39*, 4146-4157.

3. Georgakilas, V.; Otyepka, M.; Bourlinos, A. B.; Chandra, V.; Kim, N.; Kemp, K. C.; Hobza, P.; Zboril, R.; Kim, K. S., *Chem. Rev.* **2012,** *112*, 6156-6214.

4. Allen, M. J.; Tung, V. C.; Kaner, R. B., *Chem. Rev.* **2010,** *110*, 132-145.

5. Novoselov, K. S.; Geim, A. K.; Morozov, S. V.; Jiang, D.; Zhang, Y.; Dubonos, S. V.; Grigorieva, I. V.; Firsov, A. A., *Science* **2004,** *306*, 666-669.

6. Murray, R. W., *Molecular Design of Electrode Surfaces*. Wiley: New York, 1992; p 48.

7. Katz, E., *J. Electroanal. Chem.* **1994,** *365*, 157-164.

8. D'Souza, F.; Ito, O., *Chem. Soc. Rev.* **2012,** *41*, 86-96.

9. McCreery, R. L., *Chem. Rev.* **2008,** *108*, 2646-2687.

10. Axet, M. R.; Dechy-Cabaret, O.; Durand, J.; Gouygou, M.; Serp, P., *Coord. Chem. Rev.* **2016,** *308*, 236-345.

11. Van der Linden, W. E.; Dieker, J. W., *Anal. Chim. Acta* **1980,** *119*, 1-24.

12. Pocard, N. L.; Alsmeyer, D. C.; McCreery, R. L.; Neenan, T. X.; Callstrom, M. R., *J. Mater. Chem.* **1992,** *2*, 771-784.

13. Tasis, D.; Tagmatarchis, N.; Bianco, A.; Prato, M., *Chem. Rev.* **2006,** *106*, 1105-1136.

14. Karousis, N.; Tagmatarchis, N.; Tasis, D., *Chem. Rev.* **2010,** *110*, 5366-5397.

15. Schnorr, J. M.; Swager, T. M., *Chem. Mater.* **2011,** *23*, 646-657.

16. Macpherson, J. V., *Phys. Chem. Chem. Phys.* **2015,** *17*, 2935-2949.

17. Xu, J.; Granger, M. C.; Chen, Q.; Strojek, J. W.; Lister, T. E.; Swain, G. M., *Anal. Chem.* **1997,** *69*, 591A-597A.

18.   Zhang, W.; Zhu, S.; Luque, R.; Han, S.; Hu, L.; Xu, G., *Chem. Soc. Rev.* **2016,** *45*, 715-752.

19.   Sharma, S.; Singh, N.; Tomar, V.; Chandra, R., *Biosens. Bioelectron.* **2018,** *107*, 76-93.

20.   Yang, N.; Swain, G. M.; Jiang, X., *Electroanal.* **2016,** *28*, 27-34.

21.   Zittel, H. E.; Miller, F. J., *Anal. Chem.* **1965,** *37*, 200-203.

22.   Yang, N.; Waldvogel, S. R.; Jiang, X., *ACS Appl. Mater. Interfaces* **2016,** *8*, 28357-28371.

23.   Suzuki, A.; Ivandini, T. A.; Yoshimi, K.; Fujishima, A.; Oyama, G.; Nakazato, T.; Hattori, N.; Kitazawa, S.; Einaga, Y., *Anal. Chem.* **2007,** *79*, 8608-8615.

24.   Wächter, N.; Munson, C.; Jarošová, R.; Berkun, I.; Hogan, T.; Rocha-Filho, R. C.; Swain, G. M., *ACS Appl. Mater. Interfaces* **2016,** *8*, 28325-28337.

25.   Haymond, S.; Babcock, G. T.; Swain, G. M., *J. Am. Chem. Soc.* **2002,** *124*, 10634-10635.

26.   Smirnov, W.; Yang, N.; Hoffmann, R.; Hees, J.; Obloh, H.; Müller-Sebert, W.; Nebel, C. E., *Anal. Chem.* **2011,** *83*, 7438-7443.

27.   Maligaspe, E.; Sandanayaka, A. S. D.; Hasobe, T.; Ito, O.; D'Souza, F., *J. Am. Chem. Soc.* **2010,** *132*, 8158-8164.

28.   Arnold, M. S.; Blackburn, J. L.; Crochet, J. J.; Doorn, S. K.; Duque, J. G.; Mohite, A.; Telg, H., *Phys. Chem. Chem. Phys.* **2013,** *15*, 14896-14918.

29.   Clancy, A. J.; Bayazit, M. K.; Hodge, S. A.; Skipper, N. T.; Howard, C. A.; Shaffer, M. S. P., *Chem. Rev.* **2018,** *118*, 7363-7408.

30.   Meng, X.; Zhang, Z., *Catal. Today* **2018,** *315*, 2-8.

31. Rao, R.; Pint, C. L.; Islam, A. E.; Weatherup, R. S.; Hofmann, S.; Meshot, E. R.; Wu, F.; Zhou, C.; Dee, N.; Amama, P. B.; Carpena-Nuñez, J.; Shi, W.; Plata, D. L.; Penev, E. S.; Yakobson, B. I.; Balbuena, P. B.; Bichara, C.; Futaba, D. N.; Noda, S.; Shin, H.; Kim, K. S.; Simard, B.; Mirri, F.; Pasquali, M.; Fornasiero, F.; Kauppinen, E. I.; Arnold, M.; Cola, B. A.; Nikolaev, P.; Arepalli, S.; Cheng, H.-M.; Zakharov, D. N.; Stach, E. A.; Zhang, J.; Wei, F.; Terrones, M.; Geohegan, D. B.; Maruyama, B.; Maruyama, S.; Li, Y.; Adams, W. W.; Hart, A. J., *ACS Nano* **2018**.

32. Bottari, G.; Herranz, M. Á.; Wibmer, L.; Volland, M.; Rodríguez-Pérez, L.; Guldi, D. M.; Hirsch, A.; Martín, N.; D'Souza, F.; Torres, T., *Chem. Soc. Rev.* **2017,** *46*, 4464-4500.

33. Greenwood, J.; Phan, T. H.; Fujita, Y.; Li, Z.; Ivasenko, O.; Vanderlinden, W.; Van Gorp, H.; Frederickx, W.; Lu, G.; Tahara, K.; Tobe, Y.; Uji-i, H.; Mertens, S. F. L.; De Feyter, S., *ACS Nano* **2015,** *9*, 5520-5535.

34. Xue, Y.; Wu, B.; Bao, Q.; Liu, Y., *Small* **2014,** *10*, 2975-2991.

35. Geim, A. K., *Science* **2009,** *324*, 1530-1534.

36. Cai, Z.; Liu, B.; Zou, X.; Cheng, H.-M., *Chem. Rev.* **2018,** *118*, 6091-6133.

37. Ibrahim, I.; Gemming, T.; Weber, W. M.; Mikolajick, T.; Liu, Z.; Rümmeli, M. H., *ACS Nano* **2016,** *10*, 7248-7266.

38. Bottari, G.; de la Torre, G.; Guldi, D. M.; Torres, T., *Chem. Rev.* **2010,** *110*, 6768-6816.

39. Niyogi, S.; Bekyarova, E.; Itkis, M. E.; Zhang, H.; Shepperd, K.; Hicks, J.; Sprinkle, M.; Berger, C.; Lau, C. N.; deHeer, W. A.; Conrad, E. H.; Haddon, R. C., *Nano Lett.* **2010,** *10*, 4061-4066.

40. Downard, A. J., *Electroanal.* **2000,** *12*, 1085-1096.

41. Binding, S. C.; Pernik, I.; Gonçales, V. R.; Wong, C. M.; Webster, R. F.; Cheong, S.; Tilley, R. D.; Garcia-Bennett, A. E.; Gooding, J. J.; Messerle, B. A., *Organometallics* **2018**.

42. Bekyarova, E.; Itkis, M. E.; Ramesh, P.; Berger, C.; Sprinkle, M.; de Heer, W. A.; Haddon, R. C., *J. Am. Chem. Soc.* **2009,** *131*, 1336-1337.

43. Hanna, C. M.; Sanborn, C. D.; Ardo, S.; Yang, J. Y., *ACS Appl. Mater. Interfaces* **2018,** *10*, 13211-13217.

44. Lydon, B. R.; Germann, A.; Yang, J. Y., *Inorg. Chem. Frontiers* **2016,** *3*, 836-841.

45. Britz, D. A.; Khlobystov, A. N., *Chem. Soc. Rev.* **2006,** *35*, 637-659.

46. Zhao, Y.-L.; Stoddart, J. F., *Acc. Chem. Res.* **2009,** *42*, 1161-1171.

47 .Hunter, C. A.; Sanders, J. K. M., *J. Am. Chem. Soc.* **1990,** *112*, 5525-5534.

48. Thakuria, R.; Nath, N. K.; Saha, B. K., *Cryst. Growth Des.* **2019**.

49. Seth, S. K.; Manna, P.; Singh, N. J.; Mitra, M.; Jana, A. D.; Das, A.; Choudhury, S. R.; Kar, T.; Mukhopadhyay, S.; Kim, K. S., *Cryst. Eng. Comm.* **2013,** *15*, 1285-1288.

50. Cozzi, F.; Ponzini, F.; Annunziata, R.; Cinquini, M.; Siegel, J. S., *Angew. Chem.* **1995,** *34*, 1019-1020.

51. Anslyn, E. V. D., D. A., *Modern Physical Organic Chemistry*. University Science Books: Mill Valley, 2006.

52. Hwang, J. w.; Li, P.; Shimizu, K. D., *Org. Biomol. Chem.* **2017,** *15*, 1554-1564.

53. Chen, T.; Li, M.; Liu, J., *Cryst. Growth Des.* **2018,** *18*, 2765-2783.

54. Georgakilas, V.; Tiwari, J. N.; Kemp, K. C.; Perman, J. A.; Bourlinos, A. B.; Kim, K. S.; Zboril, R., *Chem. Rev.* **2016,** *116*, 5464-5519.

55. Mann, J. A.; Dichtel, W. R., *J. Phys. Chem. Lett.* **2013,** *4*, 2649-2657.

56.   Mann, J. A.; Dichtel, W. R., *ACS Nano* **2013,** *7*, 7193-7199.

57.   Li, T.-T.; Qian, J.; Zhou, Q.; Lin, J.-L.; Zheng, Y.-Q., *Dalton Trans.* **2017,** *46*, 13020-13026.

58.   Lei, H.; Liu, C.; Wang, Z.; Zhang, Z.; Zhang, M.; Chang, X.; Zhang, W.; Cao, R., *ACS Catal.* **2016,** *6*, 6429-6437.

59.   Mann, J. A.; Rodríguez-López, J.; Abruña, H. D.; Dichtel, W. R., *J. Am. Chem. Soc.* **2011,** *133*, 17614-17617.

60.   Reuillard, B.; Le Goff, A.; Cosnier, S., *Chem. Commun.* **2014,** *50*, 11731-11734.

61.   Hoarau, M.; Badieyan, S.; Marsh, E. N. G., *Org. Biomol. Chem.* **2017,** *15*, 9539-9551.

62.   Bullock, R. M.; Das, A. K.; Appel, A. M., *Chem. Eur. J.* **2017,** *23*, 7626-7641.

63.   Savéant, J.-M., *Chem. Rev.* **2008,** *108*, 2348-2378.

64.   Bard, A. J.; Faulkner, L. R., *Electrochemical Methods: Fundamentals and Applications*. 2 ed.; John Wiley & Sons: New York, 2001.

65.   Cole-Hamilton, D. J., *Science* **2003,** *299*, 1702-1706.

66.   D., T. P.; Alan, L. G.; Jonathan, H.; Bruno, J.; Nicolas, G.; Serge, P.; Holger, D.; Marc, F.; Vincent, A., *Angew. Chem.* **2011,** *50*, 1371-1374.

67.   Blakemore, J. D.; Gupta, A.; Warren, J. J.; Brunschwig, B. S.; Gray, H. B., *J. Am. Chem. Soc.* **2013,** *135*, 18288-18291.

68.   Krawicz, A.; Yang, J.; Anzenberg, E.; Yano, J.; Sharp, I. D.; Moore, G. F., *J. Am. Chem. Soc.* **2013,** *135*, 11861-11868.

69.   Kang, P.; Cheng, C.; Chen, Z.; Schauer, C. K.; Meyer, T. J.; Brookhart, M., *J. Am. Chem. Soc.* **2012,** *134*, 5500-5503.

70.   Kang, P.; Zhang, S.; Meyer, T. J.; Brookhart, M., *Angew. Chem.* **2014,** *53*, 8709-8713.

71. Reuillard, B.; Ly, K. H.; Rosser, T. E.; Kuehnel, M. F.; Zebger, I.; Reisner, E., *J. Am. Chem. Soc.* **2017,** *139*, 14425-14435.

72. Gentil, S.; Serre, D.; Philouze, C.; Holzinger, M.; Thomas, F.; Le Goff, A., *Angew. Chem.* **2016,** *55*, 2517-2520.

73. Zaera, F., *J. Phys. Chem. B* **2002,** *106*, 4043-4052.

74. Rosser, T. E.; Windle, C. D.; Reisner, E., *Angew. Chem.* **2016,** *55*, 7388-7392.

75. del Pozo, C.; Iglesias, M.; Sánchez, F., *Organometallics* **2011,** *30*, 2180-2188.

76. Schreier, M.; Luo, J.; Gao, P.; Moehl, T.; Mayer, M. T.; Grätzel, M., *J. Am. Chem. Soc.* **2016,** *138*, 1938-1946.

77. Orchanian, N. M.; Hong, L. E.; Skrainka, J. A.; Esterhuizen, J. A.; Popov, D. A.; Marinescu, S. C., *ACS Appl. Energy Mater.* **2019,** *2*, 110-123.

78. Bahnemann, D.; Henglein, A.; Lilie, J.; Spanhel, L., *J. Phys. Chem.* **1984,** *88*, 709-711.

79. Barroso, M.; Mesa, C. A.; Pendlebury, S. R.; Cowan, A. J.; Hisatomi, T.; Sivula, K.; Grätzel, M.; Klug, D. R.; Durrant, J. R., *Proc. Natl. Acad. Sci. U.S.A.* **2012,** *109*, 15640-15645.

80. Tang, J.; Durrant, J. R.; Klug, D. R., *J. Am. Chem. Soc.* **2008,** *130*, 13885-13891.

81. Jystad, A.; Caricato, M., *Chem. Mater.* **2018,** *30*, 7813-7822.

82. Ge, A.; Rudshteyn, B.; Zhu, J.; Maurer, R. J.; Batista, V. S.; Lian, T., *J. Phys. Chem. Lett.* **2018,** *9*, 406-412.

83. Nørskov, J. K.; Abild-Pedersen, F.; Studt, F.; Bligaard, T., *Proc. Natl. Acad. Sci. U.S.A.* **2011,** *108*, 937-943.

84. Unwin, P. R.; Güell, A. G.; Zhang, G., *Acc. Chem. Res.* **2016,** *49*, 2041-2048.

85. Lalaoui, N.; Rousselot-Pailley, P.; Robert, V.; Mekmouche, Y.; Villalonga, R.; Holzinger, M.; Cosnier, S.; Tron, T.; Le Goff, A., *ACS Catal.* **2016,** *6*, 1894-1900.

86. Maurin, A.; Robert, M., *J. Am. Chem. Soc.* **2016,** *138*, 2492-2495.

87. Langmuir, I., *J. Am. Chem. Soc.* **1918,** *40*, 1361-1403.

88. Laviron, E., *J. Electroanal. Chem.* **1979,** *101*, 19-28.

89. Kohmoto, M.; Ozawa, H.; Yang, L.; Hagio, T.; Matsunaga, M.; Haga, M.-a., *Langmuir* **2016,** *32*, 4141-4152.

90. Ozawa, H.; Katori, N.; Kita, T.; Oka, S.; Haga, M.-a., *Langmuir* **2017,** *33*, 11901-11910.

91. R, S. K.; Kumar, S. K. A.; Vijayakrishna, K.; Sivaramakrishna, A.; Brahmmananda Rao, C. V. S.; Sivaraman, N.; Sahoo, S. K., *Inorg. Chem.* **2018**.

92. Chakhmouradian, A. R.; Wall, F., *Elements* **2012,** *8*, 333-340.

93. Halter, D. P.; Palumbo, C. T.; Ziller, J. W.; Gembicky, M.; Rheingold, A. L.; Evans, W. J.; Meyer, K., *J. Am. Chem. Soc.* **2018,** *140*, 2587-2594.

94. Shibasaki, M.; Yoshikawa, N., *Chem. Rev.* **2002,** *102*, 2187-2210.

95. Gagne, M. R.; Stern, C. L.; Marks, T. J., *J. Am. Chem. Soc.* **1992,** *114*, 275-294.

96. Rinehart, J. D.; Long, J. R., *Chem. Sci.* **2011,** *2*, 2078-2085.

97. Sessoli, R.; Powell, A. K., *Coord. Chem. Rev.* **2009,** *253*, 2328-2341.

98. Comby, S.; Surender, E. M.; Kotova, O.; Truman, L. K.; Molloy, J. K.; Gunnlaugsson, T., *Inorg. Chem.* **2014,** *53*, 1867-1879.

99. Bottrill, M.; Kwok, L.; Long, N. J., *Chem. Soc. Rev.* **2006,** *35*, 557-571.

100. Moore, E. G.; Samuel, A. P. S.; Raymond, K. N., *Acc. Chem. Res.* **2009,** *42*, 542-552.

101. Feng, J.; Zhang, H., *Chem. Soc. Rev.* **2013,** *42*, 387-410.

102. Woodruff, D. N.; Winpenny, R. E. P.; Layfield, R. A., *Chem. Rev.* **2013**, *113*, 5110-5148.

103. Nielsen, L. G.; Junker, A. K. R.; Sørensen, T. J., *Dalton Trans.* **2018,** *47*, 10360-10376.

104. Piro, N. A.; Robinson, J. R.; Walsh, P. J.; Schelter, E. J., *Coord. Chem. Rev.* **2014,** *260*, 21-36.

105. Molloy, J. K.; Philouze, C.; Fedele, L.; Imbert, D.; Jarjayes, O.; Thomas, F., *Dalton Trans.* **2018**, *47*, 10742-10751.

106. Kyatskaya, S.; Galán Mascarós, J. R.; Bogani, L.; Hennrich, F.; Kappes, M.; Wernsdorfer, W.; Ruben, M., *J. Am. Chem. Soc.* **2009,** *131*, 15143-15151.

107. Layfield, R. A., *Organometallics* **2014,** *33*, 1084-1099.

108. Wang, Q.-X.; Xue, S.-F.; Chen, Z.-H.; Ma, S.-H.; Zhang, S.; Shi, G.; Zhang, M., *Biosens. Bioelectron.* **2017,** *94*, 388-393.

109. Rocha, J.; Carlos, L. D.; Paz, F. A. A.; Ananias, D., *Chem. Soc. Rev.* **2011,** *40*, 926-940.

110. Leoncini, A.; Huskens, J.; Verboom, W., *Chem. Soc. Rev.* **2017,** *46*, 7229-7273.

111. Hudson, M. J.; Harwood, L. M.; Laventine, D. M.; Lewis, F. W., *Inorg. Chem.* **2013,** *52*, 3414-3428.

112. Patterson, M. G.; Mulville, A. K.; Connor, E. K.; Henry, A. T.; Hudson, M. L.; Tissue, K.; Biros, S. M.; Werner, E. J., *Dalton Trans.* **2018,** *47*, 14318-14326.

113. Zhang, D.; Wang, X.; Qiao, Z.-a.; Tang, D.; Liu, Y.; Huo, Q., *J. Phys. Chem. C* **2010,** *114*, 12505-12510.

114. Lee, S. Y.; Lin, M.; Lee, A.; Park, Y. I., *Nanomaterials* **2017,** *7*, 411.

115.	zur Loye, H.-C.; Besmann, T.; Amoroso, J.; Brinkman, K.; Grandjean, A.; Henager, C. H.; Hu, S.; Misture, S. T.; Phillpot, S. R.; Shustova, N. B.; Wang, H.; Koch, R. J.; Morrison, G.; Dolgopolova, E., *Chem. Mater.* **2018,** *30*, 4475-4488.

116.	Eliseeva, S. V.; Bünzli, J.-C. G., *Chem. Soc. Rev.* **2010,** *39*, 189-227.

117.	Cousinié, S.; Gressier, M.; Reber, C.; Dexpert-Ghys, J.; Menu, M.-J., *Langmuir* **2008,** *24*, 6208-6214.

118.	Duarte, A. P.; Gressier, M.; Menu, M.-J.; Dexpert-Ghys, J.; Caiut, J. M. A.; Ribeiro, S. J. L., *J. Phys. Chem. C* **2012,** *116*, 505-515.

119.	Zhang, D.; Tang, D.; Wang, X.; Qiao, Z.-a.; Li, Y.; Liu, Y.; Huo, Q., *Dalton Trans.* **2011,** *40*, 9313-9319.

120.	de Bettencourt-Dias, A.; Rossini, J. S. K., *Inorg. Chem.* **2016,** *55*, 9954-9963.

121.	Lionetti, D.; Day, V. W.; Blakemore, J. D., *Dalton Trans.* **2017,** *46*, 11779-11789.

Chapter 2

Noncovalent Immobilization of Molecular Lanthanide Complexes

2.1 *Abstract*

Much work has been done in the field of *f*-element chemistry to understand and develop the unique magnetic, electronic, and catalytic properties of the lanthanides. In recent years, there has been significant focus on the development of novel sensor-technologies,[1-2] single-molecule magnets,[3-4] and catalysts for organic transformations[5-6] and small molecule activation[7] utilizing lanthanide complexes. While the field of lanthanide chemistry and its applications is increasing in vibrancy and variety, one area that has received less attention than it deserves is that of surface immobilization. While there are multiple reports in the literature of surface-immobilized metals from the *d*-block,[8-10] there are relatively few for immobilized lanthanide complexes. The ability to tightly bind and immobilize lanthanide-containing complexes is especially challenging due to the complex coordination chemistry of the lanthanides. Driven by these motivations, this chapter discusses the design and synthesis of a novel ligand framework that can bind and encapsulate Ln^{3+} ions and engage in noncovalent surface immobilization on carbon surfaces. Additional work examines the impact of ligand structure on the surface stability for a family of immobilized lanthanide complexes.

The first reported organolanthanide complexes were reported in
1954 by Wilkinson and Birmingham for a series of Cp_3Ln complexes (Ln
= Sc, Y, La, Ce, Pr, Nd, Sm, Gd) (**Scheme 2.1**).[11] In 1956, a follow-up
report by Wilkinson and Birmingham discussed some of the physical
properties of these Cp_3Ln complexes, such as their magnetic
susceptibility.[12] These initial reports were followed by contributions from
Fischer *et al* in the mid-1960s and their work on Cp_2Ln complexes (Ln =
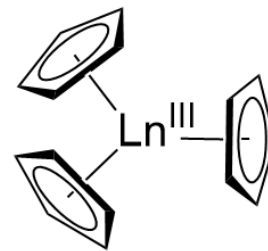
Scheme 2.1. Cp_3Ln
complexes first
synthesized by
Wilkinson and
Birmingham in
reference 11.

Eu, Yb)[13-14] as well as work done by other groups in the early 1970s on Ln sandwich complexes

using cyclooctatetraenyl dianion ($C_8H_8^{2-}$) ligand systems.[15-17] Although these contributions have

proven crucial to the fundamental understanding of organometallic lanthanide chemistry, their

importance was not immediately recognized as lanthanides were perceived as mere curiosities that

possessed no relevant applications. However, over the past two decades, numerous studies of the

lanthanides have demonstrated that these elements possess many unique properties with potential

applications in a variety of fields.[18-20] In today's world, smartphones,[21] wind turbines,[22] medical

diagnostic agents,[23] and car batteries[24] are just a few of the places one can find lanthanides.

Their tendency to adopt stable +3 oxidation states coupled with their large ionic radii makes

the coordination chemistry of the lanthanides quite different from those of *d*-transition metals.[25-26]

The large size of the trivalent lanthanide ions (103.2 pm for La^{3+} to 86.1 pm for Lu^{3+} assuming 6-

coordinate[27]) requires significantly higher coordination numbers (CN $\geq$ 7), while their 4*f* orbitals

are considered core-like and unable to participate in bonding due to shielding by the 5*s* and 5*p*

orbitals.[28] As a result, the interactions between Ln^{3+} ions and their corresponding ligands are purely

electrostatic and the coordination geometries of these complexes are exclusively determined by
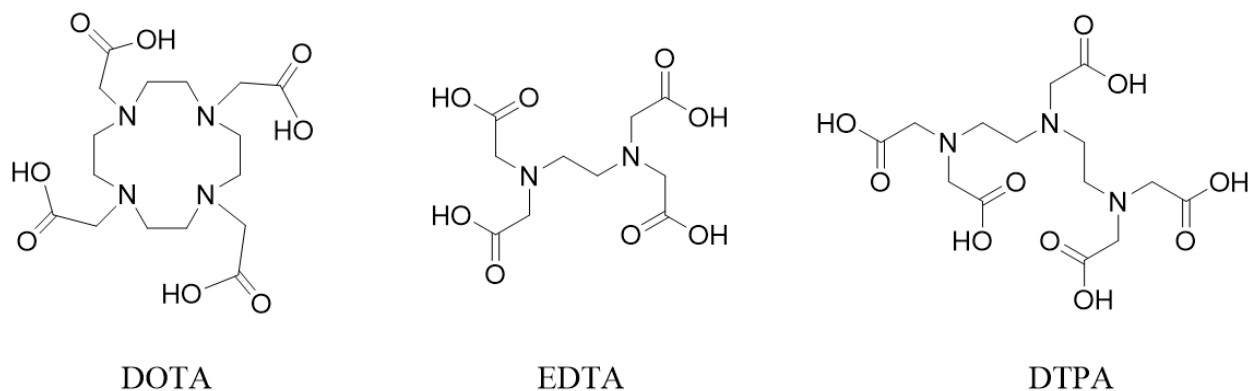
Scheme 2.2. Schematic representation of common ligands used to encapsulate Ln^{3+} ions.

ligand structure and steric effects.[25] Due to the ionic nature of the metal-ligand interaction, Ln^{3+} complexes are considerably more labile than those of *d*-block metals and can participate in rapid, facile ligand exchange.[29] To achieve stable, kinetically inert Ln^{3+} complexes, ligands containing more than 6 anionic "hard" donating groups (N or O donor atoms) such as DOTA, EDTA, and DTPA have been proven quite successful (**Scheme 2.2**).[25-26, 29-30] The work done to further the understanding of lanthanide coordination chemistry has provided an important foundation for all fields of *f*-element chemistry; however, much work is still necessary to improve the stability of lanthanide complexes to prevent potential decomposition and metal-leaching.[31]

In addition to their coordination chemistry, lanthanide ions are well known for their magnetic and luminescent properties.[32-34] The anisotropic magnetic properties of the trivalent lanthanides are significant compared with metals of the *d*-block due to the presence of strong orbital contributions to the ground state.[3] These features have made lanthanides enticing targets within the field of molecular magnetism, with considerable promise in the field of single-molecule magnets (SMMs).[3-4, 34-35]

The absorption and emission properties of the lanthanides arise from Laporte forbidden f-f transitions and have made them attractive for a variety of applications.[33, 36] As previously

mentioned, the 4*f* orbitals of the lanthanides are considerably shielded from the coordination environment by the 5*s* and 5*p* orbitals. Because of this shielding, the f-f transitions are relatively independent of coordination effects, resulting in emission colors that are unique to each lanthanide ion while maintaining long-lived (µs to ms) excited-state lifetimes and narrow, line-like emission bands.[23, 31-32, 36-37] The unusual spectroscopic properties of the lanthanides have inspired a myriad of intense studies of these elements and have led to significant advancement in the fields of fluorescence imaging and sensing,[2, 31, 38] biological assays,[1, 33] and electronic display technologies.[39]

Given their broad applications in materials, enhancing the capability to incorporate lanthanide metals and their complexes onto solid supports has become an increasingly active area of research.[40-42] However, achieving surface-immobilization of molecular lanthanide species is often difficult due to their size and coordination chemistry. For these reasons, this work discusses the design, synthesis, and immobilization of molecular lanthanide complexes. Previous work from the Blakemore group[43] reported the synthesis and characterization of a small family of lanthanide complexes, referred to in this work as **M(LTO)** (**L***igand* **T***ripodal* **O***rtho-position*) where M = Ce, Nd, Sm, Eu (**Scheme 2.3**). The complexes were synthesized utilizing a pyrene-appended tripodal ligand motif that is capable of noncovalent immobilization on a carbon surface, followed by characterization by various electrochemical and spectroscopic techniques. Integration of the peak data obtained from X-ray photoelectron spectroscopy (XPS) supports that the molecular integrity of the **M(LTO)** complexes is maintained upon surface-immobilization, the details of which will be discussed later in this chapter. Experiments utilizing cyclic voltammetry also support successful

M(LTO)   **M(LTP)**
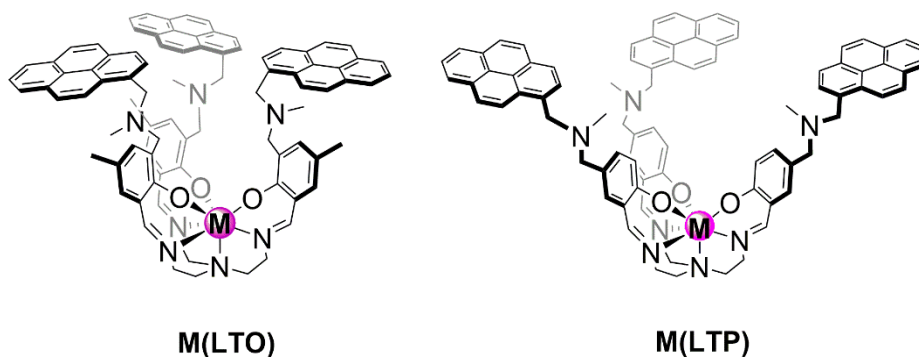
Scheme 2.3. Representation of pyrene-appended metal complexes discussed in this work. **M** = Ce, Nd, Sm, Eu, **LTO** = Ligand tripodal *ortho* position, **LTP** = Ligand tripodal *para* position.

immobilization of the **Ce(LTO)** complex due to the presence of a single quasi-reversible Ce(IV/III) couple at –0.34 V versus the Fc$^{+/0}$ couple.

Despite the ability to successfully immobilize these complexes on a graphitic surface, time-dependent electrochemical studies of the **Ce(LTO)** complex showed limited surface stability. Cyclic voltammetry measurements showed significant loss of the **Ce(LTO)** complex from the surface over the course of an hour. Given the *ortho*-positioning of the pyrene moieties combined with pyrene's tendency to engage in π-π stacking interactions with itself, the observed instability of the **Ce(LTO)** complex was hypothesized to arise from aggregation-effects between the pyrene appendages of the tripodal ligand scaffold. Aggregation of the pyrene moieties would result in a diminished interaction with the graphitic surface, resulting in overall loss of the complex from the surface. To further investigate this behavior, an analogous tripodal ligand scaffold was developed and synthesized with hopes of disfavoring the aggregation behavior of the pyrene groups. The rest of this chapter will discuss the synthesis and characterization of the modified tripodal lanthanide complexes, **M(LTP)** (**L***igand* **T***ripodal* **P***ara-position*) (**Scheme 2.3**), as well as a more quantitative analysis of the surface behavior of the **M(LTO)** and **M(LTP)** complexes probed by various electrochemical methods.

2.3 *Results and Discussion*

Since their initial discovery in 1864, Schiff base ligands have been a popular means to coordinate numerous metals of various oxidation states.[44] These Schiff base ligand frameworks often feature four coordination sites for the desired metal: two imine groups and two other groups (typically phenol groups). As discussed previously, lanthanide ions tend to adopt significantly higher coordination numbers due to their large ionic radii. For this reason, tripodal Schiff base ligand frameworks have been used in the field of lanthanide chemistry due to their ability to successfully encapsulate and stabilize Ln^{+3} ions by providing numerous (≥ 7) donor atoms.[25, 45] Previous work from the Blakemore group features a tripodal $[N_4O_3]$-trisaryloxide-trisimine scaffold decorated with pyrene moieties that are *ortho-* to the phenoxide oxygen.[43] For this work, an analogous tripodal framework was designed and synthesized that moved the pyrene 'arm' groups from the *ortho-* to the *para*-position. Compared to other ligand frameworks, these tripodal scaffolds are quite modular, in that changing the functionality on each of the tripod's 'arm' components is readily accomplished by using the appropriate aldehyde precursor.

2.3.1 *Ligand Synthesis*

The desired pyrene group can be readily synthesized according to adapted literature procedures by reacting commercially available pyrene carboxaldehyde with gaseous methylamine.[46] Produced *in situ* is an imine compound that is readily reduced with sodium borohydride to generate *N*-methyl-1-(pyren-1-yl)methanamine. The selected benzylic chloride was synthesized following literature procedure by reacting salicylaldehyde with paraformaldehyde in concentrated hydrochloric acid.[47] The resulting pyrene moiety was then installed in the *para-*
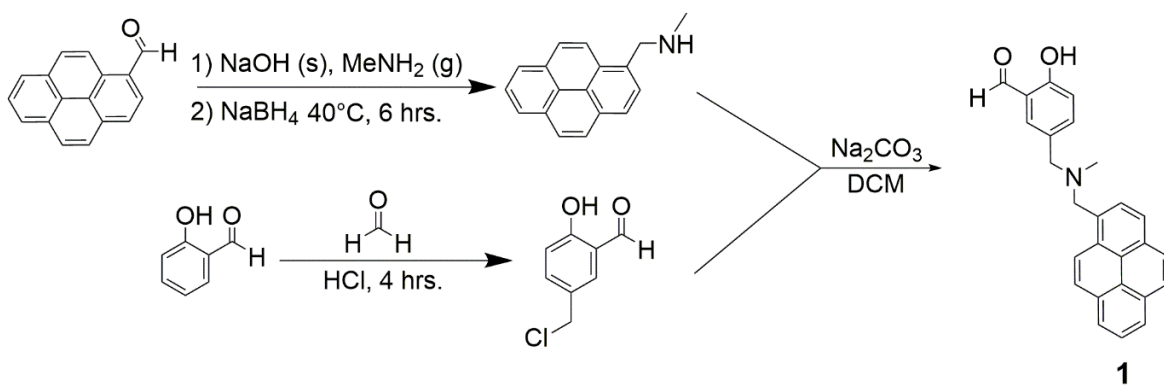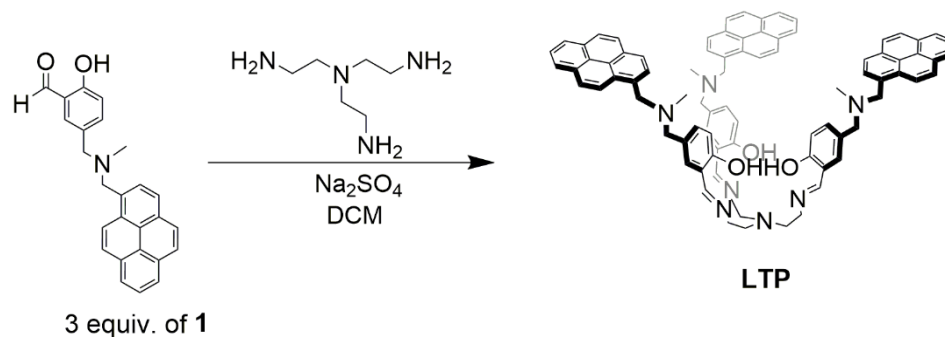
Scheme 2.4. Synthetic scheme for the synthesis of compound **1**.

position by reacting the *N*-methyl-1-(pyren-1-yl)methanamine with the desired benzylic chloride

to generate the 'arm' component **1** (**Scheme 2.4**).[47-48] Once isolated and characterized by ^{1}H NMR

(**Appendix A, Figure A29**), compound **1** can be subsequently dried and installed *via* a

condensation reaction with tris(2-aminoethyl)amine (TREN) to generate the desired tripodal

Schiff-base framework, **LTP** (**L**igand **T**ripodal *Para*-substituted) (**Scheme 2.5**).[45]

The **LTP** ligand framework was cleanly isolated from the reaction mixture and

characterized by ^{1}H NMR, as well as X-ray photoelectron spectroscopy (XPS) which will be

discussed in detail in a later section. The ^{1}H NMR (**Appendix A**, **Figure A30**) spectra show one

set of peaks, indicating that the tripodal ligand exhibits C_{3v} symmetry in solution on the NMR

timescale.

2.3.2 *Synthesis and Characterization of M(LTP) Complexes*

Subsequent metalation of the **LTP** is achieved *via* a standard protonolysis by reacting the

desired *f*-block **M**$^{3+}$ of choice with a stoichiometric amount of **LTP**. Utilizing **M(N(SiMe₃)₂)₃**

compounds, where **M** = Ce, Nd, Sm, Eu (**Scheme 2.6**),[49] the desired metal of choice can reliably

be installed into the **LTP** framework. Isolation of the **M(LTP)** complexes is readily achieved by

Scheme 2.5. Synthetic scheme for the synthesis of the complete, tripodal **LTP** ligand.

filtration, as the **M(LTP)** complexes are insoluble in common, polar organic solvents (tetrahydrofuran, acetonitrile). This behavior was also observed for the **M(LTO)** complexes and is attributable to the strong intramolecular forces among the pyrene groups. The **M(LTP)** complexes were examined by ^{1}H NMR and exhibit the same C_{3v} behavior in solution as the free **LTP** ligand, resulting in only one set of peaks for the complexes containing no peaks for the free ligand that would indicate an incomplete reaction. Due to the paramagnetic, Lewis acidic nature of the lanthanide metal centers used in these complexes, the ^{1}H NMR spectra display increased broadness of individual peaks and large chemical shifts (See **Appendix A** for spectra).
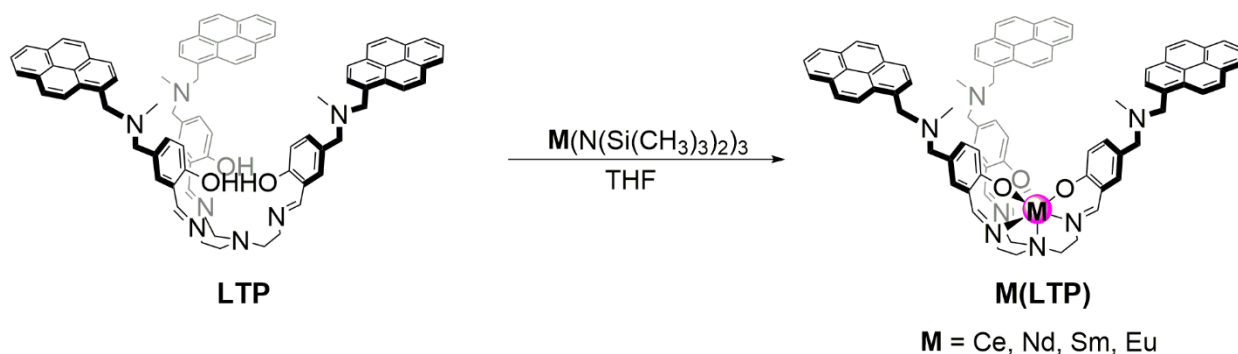
Scheme 2.6. Synthetic scheme for the synthesis of **M(LTP)** complexes.

2.3.3 *Surface Immobilization of* **M(LTP)** *Complexes*

Numerous types of carbon surfaces have been utilized for surface immobilization studies, some of the most prevalent being single- and multi-walled carbon nanotubes.[50] In order to accommodate large surface loadings, we chose to utilize drop-casted carbon black (Ketjen black) on basal-plane highly oriented pyrolytic graphite (HOPG) electrodes due to its high microscopic surface area.[51-52] Similar to previous work done on the **M(LTO)** complexes, the **M(LTP)** analogues were immobilized by soaking our Ketjen black electrodes in a 0.5 mM solution of the desired metal complex in dichloromethane for 12 hours and then rinsed with neat dichloromethane.[43]

2.4 *X-ray Photoelectron Spectroscopy (XPS)*

After soaking the Ketjen black electrodes in a concentrated solution of the **LTP** ligand and **M(LTP)** complexes, X-ray photoelectron spectroscopy (XPS) was used to interrogate the nature of the immobilized species. Surface analysis by XPS is accomplished by irradiating samples with soft, monoenergetic X-rays and analyzing the energy of the detected electrons emitted by the photoelectric effect.[53] These electrons have a measurable kinetic energy given by **Equation 2.1**, where hυ is the energy of the photon, BE is the binding energy of the atomic orbital from which the electron originates, KE is the kinetic energy of the detected electrons, and Φ_s is the spectrometer work function and serves as a correctional factor for comparing data across instruments.[53]

$$\text{Equation 2.1} \qquad KE = h\upsilon - BE - \Phi_s$$

Common X-ray sources for XPS experiments produce Mg Kα (1253.6 eV) or Al Kα (1486.6 eV) X-rays, both of which will be used in this study and discussed in more depth in later sections. Utilizing the values from the X-ray sources and the kinetic energy of the emitted electrons, the binding energies can be calculated for a sample. Core binding energies are determined by a variety of factors, such as the oxidation state, effective nuclear charge, and electrostatic shielding of an element. As a result, small variations in a surface or complex composition can cause noticeable changes in an XPS spectrum. This ability to observe minute differences in a spectrum can provide valuable insights to the composition, purity, empirical formula, oxidation state, chemical-state, and thickness of a surface or material.[53]

2.4.1 *Al Kα XPS Data*

The survey spectrum obtained for a blank Ketjen black electrode using Al Kα (1486.6 eV) displayed appropriate signals for the carbon (C) 1s orbital centered around 285 eV. Additionally, oxygen (O) and fluorine (F) 1s signals were observed at 530 eV and 680 eV, respectively (**Figure 2.1**).[53] These contributions can be attributed to the preparation of the Ketjen black coating and the use of reagents such as Triton X and polyvinylidene fluoride (see **Appendix A** for experimental details). No other peaks were observed that could be attributed to the presence of any metal or nitrogen-containing organic compounds that could interfere with the interpretation of other spectra.
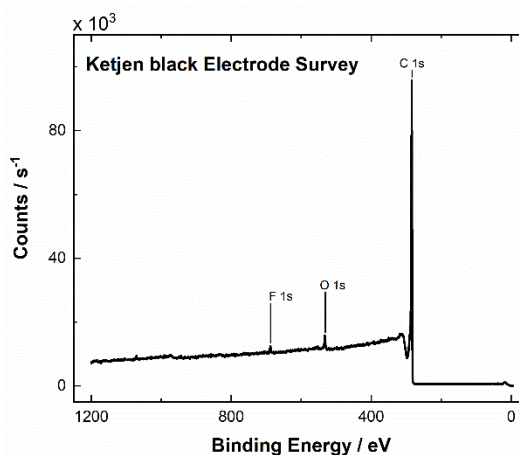

Figure 2.1. XP spectrum of a blank Ketjen black electrode from the Al Kα source data.

39

When examining an electrode functionalized with free **LTP** ligand, the survey revealed the same contributions from the C, O, and F $1s$ orbitals. An additional peak centered at a binding energy of 400 eV was also observed and is readily assigned to a N $1s$ orbital (**Figure 2.2**).[54] As expected, contributions from N $1s$ orbitals were also observed in the spectra for the **M(LTP)** complexes, centered at
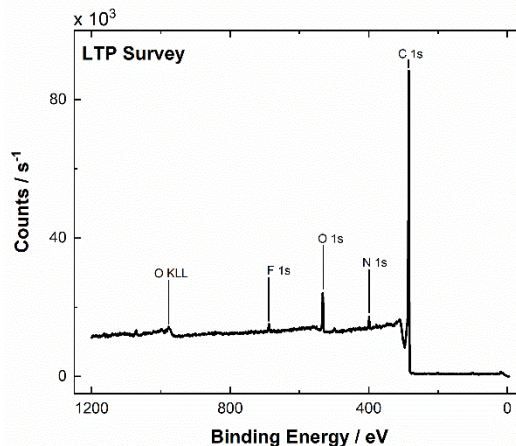
Figure 2.2. XP spectrum of the immobilized **LTP** ligand from the Al Kα source data.

binding energies of approximately 400 eV. Additionally, the spectra of the **M(LTP)** complexes also displayed the appropriate binding energies for each of the metal's $3d$ and $4d$ orbitals (**Figure 2.3**).[55-56] Other contributions from the given *f*-block metals, such as the $4s$, $5s$, $3p$, $4p$, $5p$, and $4f$,

Figure 2.3. XP survey spectra for the **M(LTP)** complexes from the Al Kα data.

40

were also located in the survey spectra for the **M(LTP)** complexes; however, these peaks were not analyzed in this work as the short lifetimes of the associated core-electron excitations results in broadened photoelectron signals that masks resolvable, fine structure.[57]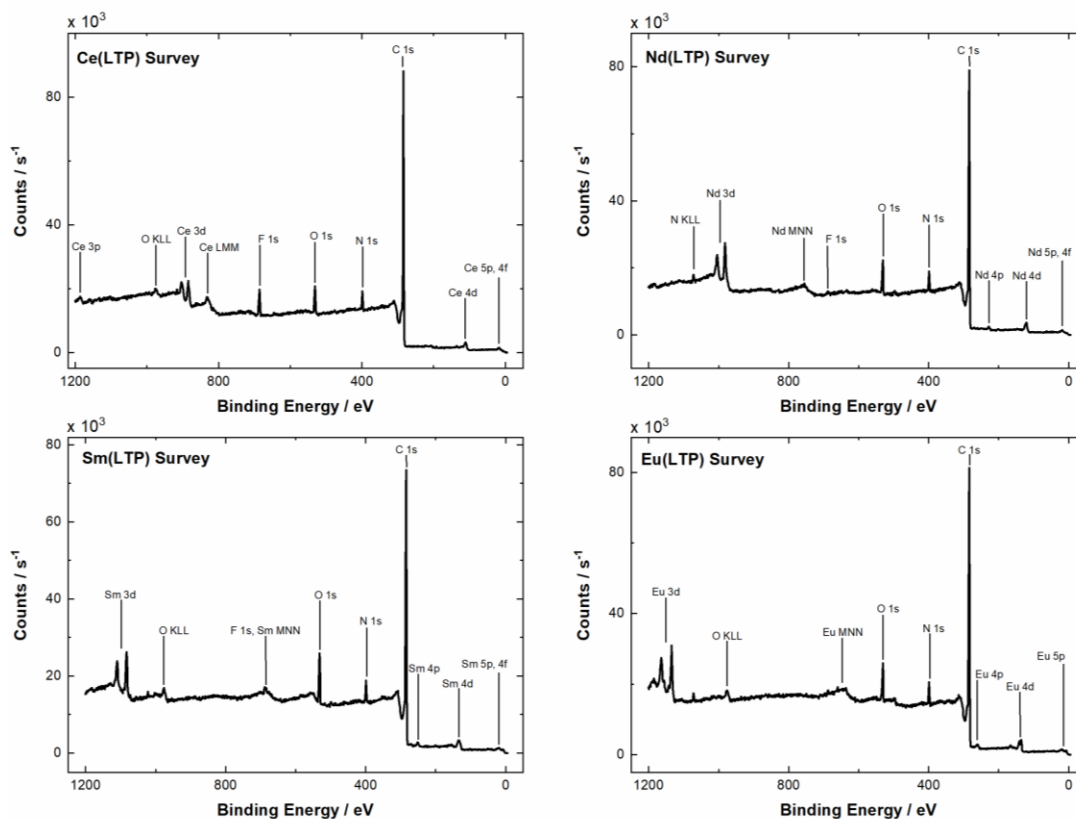 A complete set of stacked spectra for a blank Ketjen black electrode, the free **LTP** ligand, and each **M(LTP)** complex is depicted in **Figure 2.4**.

From the data plotted in **Figure 2.4**, there is a noticeable increase in the binding energies observed for the main M $3d$ and M $4d$ signals as one moves across the $4f$ row from cerium to europium. In XPS, higher binding energies indicate that an element is more oxidized while lower binding energies are indicative of an element that is more reduced. An illustration of this concept
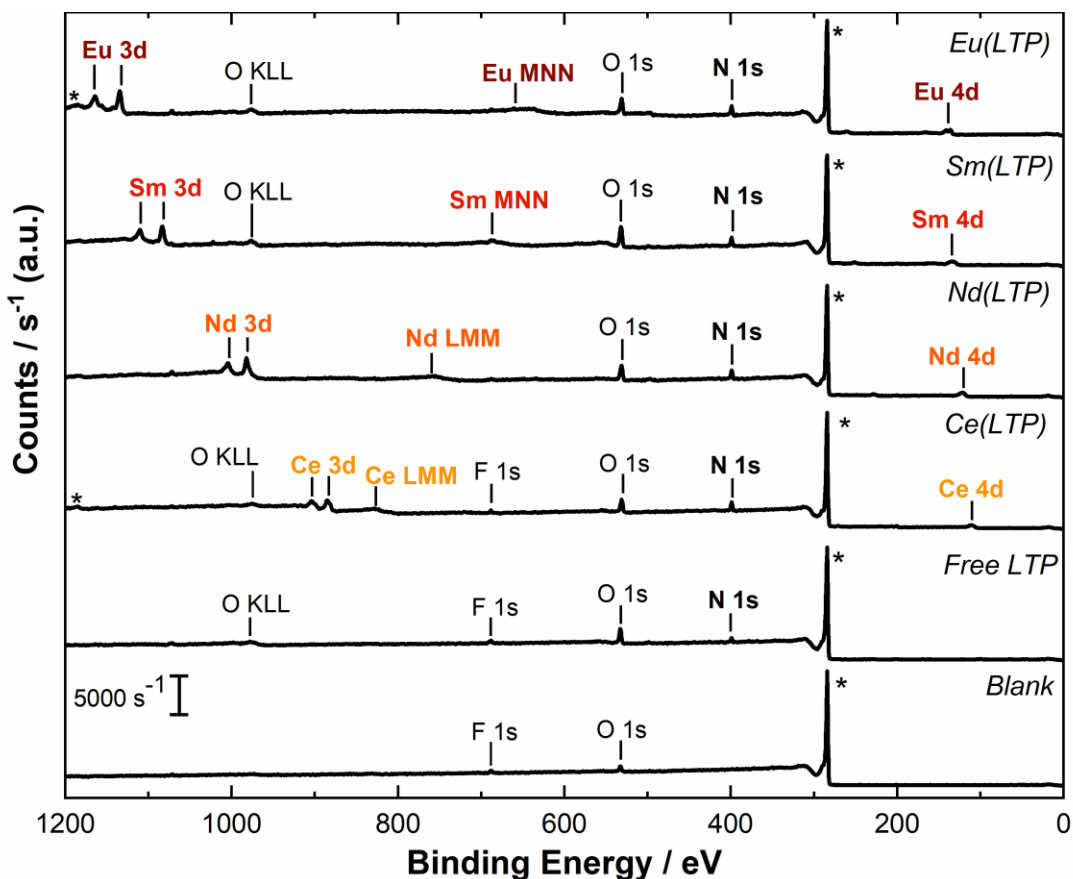

Figure 2.4. Stacked Al-source XP survey spectra for a blank electrode and electrodes functionalized with free **LTP** and **M(LTP)** (M = Ce, Nd, Sm, Eu) complexes. Signals corresponding to the surface bound complexes are highlighted in bold. Signals corresponding to carbon (C $1s$ and C KLL) are marked with (*).

41

would be to compare the observed binding energies of carbon-containing compounds, where the carbon $1s$ signal for a carboxylic acid group is typically observed at 289 eV while the carbon $1s$ signal for an alkane group is observed around 285 eV.[58] For the data obtained for the **M(LTP)** complexes, the increasing binding energies for the M $3d$ and M $4d$ signals are a result of the increasing effective nuclear charge (Z_{eff}) of the lanthanide metal centers. Due to the poor shielding provided by the electrons in the $4f$ subshell, there is an increase in Z_{eff} across the lanthanide series.[59] The increasing Z_{eff} causes the ionic radii of the lanthanide metal to decrease as the electrostatic force from the nucleus on the valence electrons increases, causing the coined 'lanthanide contraction'.[59-60] Both the increasing Z_{eff} and decreasing ionic radii have an impact on the binding energies observed in the XP data for the **M(LTP)** complexes. For example, the M $3d$ and M $4d$ signals **Ce(LTP)** complex are centered at 894.5 eV and 111.5 eV, respectively. Comparatively, the M $3d$ and M $4d$ signals for the **Eu(LTP)** complex are centered at much greater binding energies: 1149.5 eV and 139.4 eV, respectively. The europium metal center of the **Eu(LTP)** complex has a much greater Z_{eff} and smaller ionic radii compared to the cerium metal center of the **Ce(LTP)** complex, which causes the electrons in the **Eu(LTP)** complex to be held more tightly than those in the **Ce(LTP)** complex.

Data obtained from XPS can be used to determine the stoichiometry of an immobilized complex. First, the data obtained for the N $1s$ region of the **LTP** ligand and the **M(LTP)** complexes were fit according to the expected stoichiometry.[61] The N $1s$ peak was fit with three contributions that were constrained to a ratio of 3:3:1 for the 3 imine nitrogen species (red), the 3 tertiary amines (blue), and the 1 axial nitrogen species (green) as depicted in **Scheme 2.7**. The slight variations in the environment experienced by the nitrogen group can give rise to minute changes in the binding energies of the N $1s$ orbital.[53] Upon examination of the N $1s$ regions of the **M(LTP)** complexes,

there are small changes in the binding energies that appear to trend with the Lewis acidic nature of the lanthanide metals used (**Figure 2.5**). As a result, the lanthanide metal center is capable of withdrawing electron density from the interacting nitrogen atoms, resulting in a subtle increase in the binding energies for the imine (red) and axial (green)
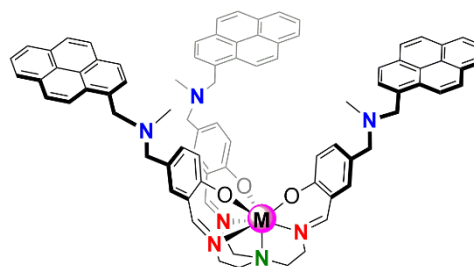
Scheme 2.7. A color-coded representation of the N 1*s* signals in the XPS spectrum. Blue: tertiary nitrogen, Red: imine nitrogen, Green: axial nitrogen.

nitrogen groups.[53, 56] After fitting the N 1*s* data, the positions of each of the contributions were tabulated and are shown in **Table 2.1**. The binding energies for the blue N 1*s* contributions across the complexes do not appreciably shift, suggesting that these contributions come from nitrogen atoms that are not directly ligated to the metal center. The values for the red and green N 1*s* fits,

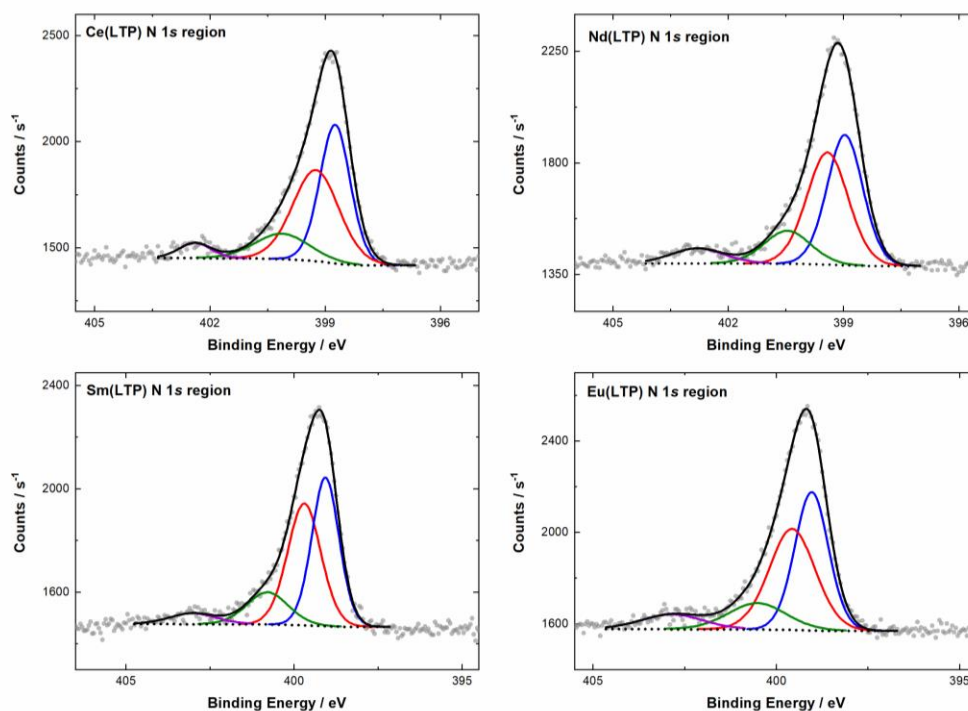**Figure 2.5**. Al Kα-source XP spectra for the N 1*s* region for electrodes functionalized with **M(LTP)** complexes. Legend: gray dots: data; dashed black lines: fitting background; blue, red and green lines: fitting curves for three distinct nitrogen environments (constrained to 3:3:1 area ratio); purple line: fitting curve that corresponds to the presence of a protonated nitrogen species; continuous black line: overall fit.

Compound	N, blue (eV)	N, red (eV)	N, green (eV)	N, violet (eV)
LTP	399.0	399.3	400.4	402.4
Ce(LTP)	398.8	399.2	400.1	402.4
Nd(LTP)	399.0	399.4	400.5	402.5
Sm(LTP)	399.1	399.6	400.6	402.6
Eu(LTP)	399.1	399.6	400.8	402.6

Table 2.1. Tabulated values for the fittings of the N 1s data.

however, do experience large shifts greater than $\pm$ 0.2 eV,[53, 55, 62] suggesting that these contributions come from nitrogen atoms that are capable of interacting with the metal center. Given these observations, the assignments of these contributions can be made, where the blue N 1s fits are the tertiary amines near the pyrene groups, the red N 1s fits are attributed to the imine nitrogen atoms, and the green N 1s contributions are from the axial nitrogen. These assignments agree qualitatively with those previously made for the N 1s region of the **M(LTO)** complexes.

Within the N 1s region, an additional contribution is observed at significantly higher binding energies and is indicated by a violet fit line. These contributions center around 402.5 eV for both the free **LTP** and each **M(LTP)** complex and are much higher in binding energy than what is expected for any nitrogen species within the **LTP** framework. However, reported values for protonated amines, such as ammonium salts, are often cited at binding energies around 402 to 403 eV.[54, 63] Given this information, the contribution at higher binding energies has been fit and is assigned to the presence of a protonated amine species. The presence of a protonated species may be in part because the **M(LTP)** complexes are water and oxygen sensitive. Before the functionalized electrodes are loaded into the XPS instrument, they are first attached to a base—this step must be done in ambient air. The process of loading the electrodes into the instrument can

take up to five minutes, enough time for the complex to partially decompose. The presence of a protonated amine species is not detected in the ^{1}H NMR of the **M(LTP)** complexes and no peaks corresponding to the free ligand were present that would support decomposition in solution (See **Appendix A** for spectra). This evidence supports that partial decomposition occurs only when the complex of interest is immobilized on the Ketjen black electrode and is most likely due to the partial exposure to ambient conditions (e.g. air, water) when loaded into the instrument for analysis by XPS.

Upon ionization in an XPS experiment, p, d, and f orbitals become split as a result of spin-orbital coupling.[58] When an electron is emitted from an initially fully occupied shell with a nonzero orbital momentum ($l = 1, 2, 3$), there remains an unpaired electron spin ($s = \pm \frac{1}{2}$) that couples parallel or anti-parallel to the angular momentum ($j = |l + s|$) of the orbital (**Table 2.2**).[53] As a result, peaks for p, d, and f orbitals are split into doublets with fixed area ratios (1:2 for p, 2:3 for d, and

Subshell	j Values	Degeneracy
s	$\frac{1}{2}$	-
p	$\frac{1}{2}, \frac{3}{2}$	2, 4 = 1, 2
d	$\frac{3}{2}, \frac{5}{2}$	4, 6 = 2, 3
f	$\frac{5}{2}, \frac{7}{2}$	6, 8 = 3, 4

Table 2.2. Tabulated mathematical representation for spin-orbital splitting adapted from reference 47.

3:4 for f levels), and the difference in energy between the peaks can assist in element identification.[55, 64] Looking at the fitting for the $3d$ and $4d$ regions of the **M(LTP)** complexes, there are two observable, distinct peaks for each complex that are related to the $3d_{3/2}$, $3d_{5/2}$, $4d_{3/2}$, and $4d_{5/2}$ (**Figure 2.6** and **Figure 2.7**). In addition to the expected peaks for the $nd_{3/2}$ (red) and $nd_{5/2}$ (blue), additional features (green) are also observed. These peaks can be attributed to shake-up and
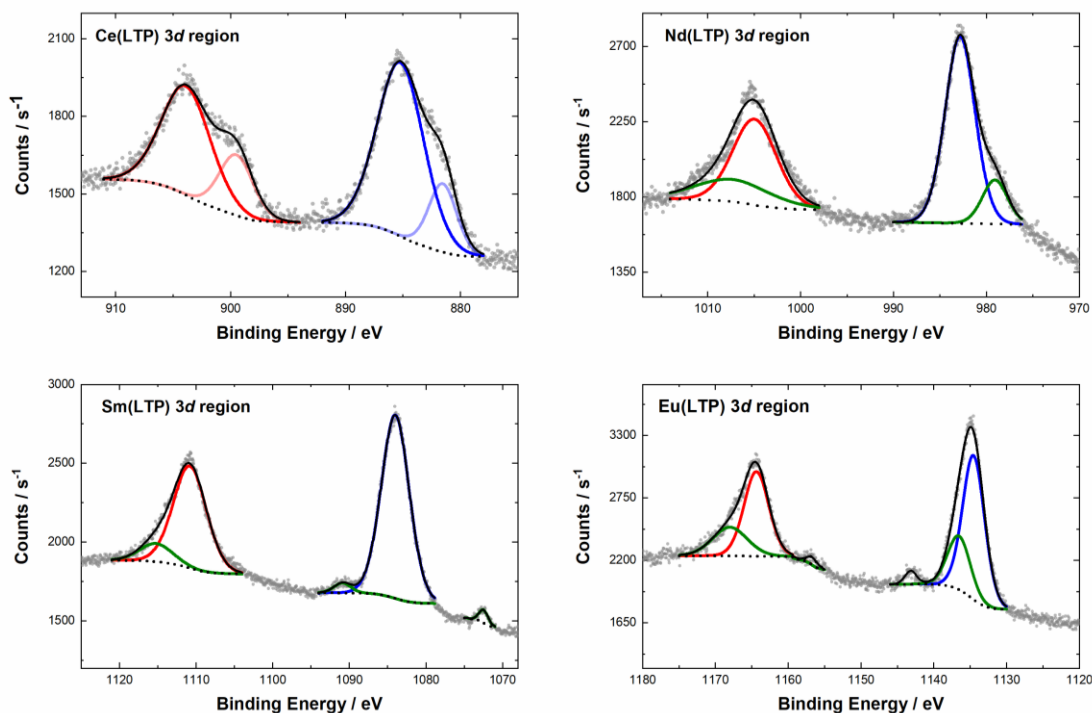
Figure 2.6. Al-source XP spectra for the respective M 3d regions for **M(LTP)** complexes. Legend: gray dots: data; dashed black lines: fitting background; blue lines: M 3$d_{5/2}$ peak fit; red lines: M 3$d_{3/2}$ peak fit (constrained to 2/3 area with respect to M 3$d_{5/2}$); green lines: shake-up and shake-down peaks fit; continuous black line: overall fit.

shake-down features that are often observed for lanthanide-containing species.[62, 64-67] The presence of shake-up and shake-down features in lanthanide-containing samples has been attributed to a variety of causes, such as paramagnetism, charge-transfer events, and the tendency for electrons in lanthanide complexes to relax into various degenerate final states.[68-71]

As mentioned previously, XPS data can be used to calculate the elemental composition of a sample and calculate stoichiometric ratios.[53] These tabulated ratios can be used to determine whether the structural integrity of the **M(LTP)** complexes is maintained upon immobilization. To determine these ratios, the areas for the N 1s region and M 3d regions were integrated and normalized utilizing Scofield relative sensitivity factors.[72] Relative sensitivity factors are well-established in the literature and must be used for these calculations since XPS has varying
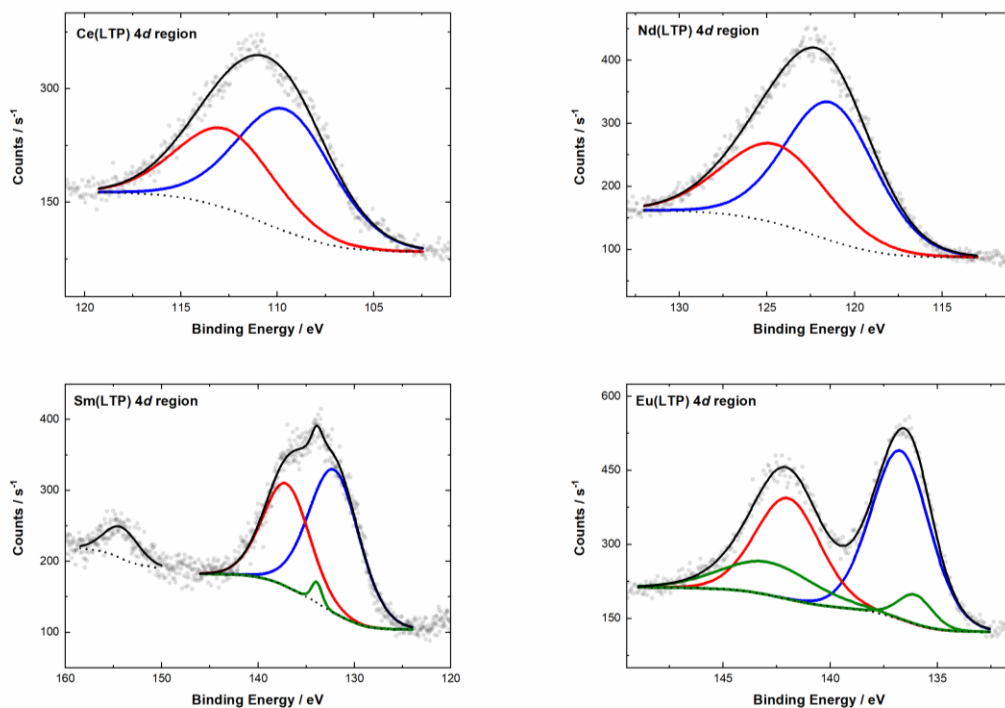
Figure 2.7. Al-source XP spectra for the respective M 4d regions for **M(LTP)** complexes. Legend: gray dots: data; dashed black lines: fitting background; blue lines: M $4d_{5/2}$ peak fit; red lines: M $4d_{3/2}$ peak fit (constrained to 2/3 area with respect to M $4d_{5/2}$); green lines: shake-up and shake-down peaks fit; continuous black line: overall fit.

sensitivities for different elements.[58] The calculated M:N ratio that would be expected from this analysis would be 1:7 since there is 1 metal center present per 7 nitrogen atoms in the **M(LTP)** framework. The calculated ratios for the M:N ratios are tabulated in **Table 2.3** and show an approximate relationship of 1:7. This analysis of the XPS data confirms that the structural integrity of the **M(LTP)** complexes is maintained upon immobilization.

Compound	M $3d_{5/2}$ (eV)	M $3d_{3/2}$ (eV)	M $4d_{5/2}$ (eV)	M $4d_{3/2}$ (eV)	M $3d$ splitting (eV)	M $4d$ splitting (eV)	M : N Ratio
Ce(LTP)	885.3	903.7	109.8	113.1	18.4	3.3	1 : 7.0
Nd(LTP)	982.8	1004.9	121.3	124.5	22.1	3.2	1 : 6.5
Sm(LTP)	1084.0	1110.8	132.1	137.1	26.8	5.0	1 : 7.3
Eu(LTP)	1134.5	1164.4	136.7	142.0	29.9	5.3	1 : 8.1

Table 2.3. Tabulated values for the shift in peaks for the M $3d$ and M $4d$ regions of the **M(LTP)** complexes from Al-source XP data. **M:N** ratio was calculated utilizing the integration of the total area of the M $3d$ regions, N $1s$ regions, and normalizing them with the Scoffield relative sensitivity factors. The expected ratio is a 1:7 relationship based on the stoichiometry of the complex.

2.4.2 *Mg Kα XPS Data*

Within the Al Kα data, noticeable contributions to the M $3d$ and $4d$ regions, depicted with green fit lines in **Figure 2.6** and **Figure 2.7**, can be assigned to Auger processes. For example, the M $3d_{5/2}$ of the **Nd(LTP)** region has a contribution centered at 979 eV that can be readily assigned to the O KLL Auger process. Since Auger lines have

Figure 2.8. Survey spectrum of a Kejen black electrode functionalized with free **LTP** ligand utilizing Mg Kα (1253.6 eV) source XPS.

kinetic energies that are independent of the ionizing radiation, their resulting binding energies can be shifted by switching X-ray sources. For this, a Mg Kα (1253.6 eV) source was used to obtained additional XPS data to attempt to shift the binding energies of Auger processes (see **Appendix A** for experimental details). A survey spectrum utilizing the Mg Kα source for a Ketjen black electrode functionalized with **LTP** is shown in **Figure 2.8**. Of important note is that the backgrounds for Mg Kα source spectra are noticeably higher than those of Al Kα source spectra. The features observed in the backgrounds are intrinsic to the source type and are not to be confused with an instrumental error or sample contamination. In addition to higher backgrounds, using the Mg Kα source often results in an increase in the number of X-ray satellite features present in the resulting spectra. These features are attributed to the non-monochromatic nature of the Mg Kα source, resulting in excitation of electrons in the sample with multiple photon energies coming from the Bremsstrahlung radiation (in other words, non-monochromatic X-ray).[53, 64]
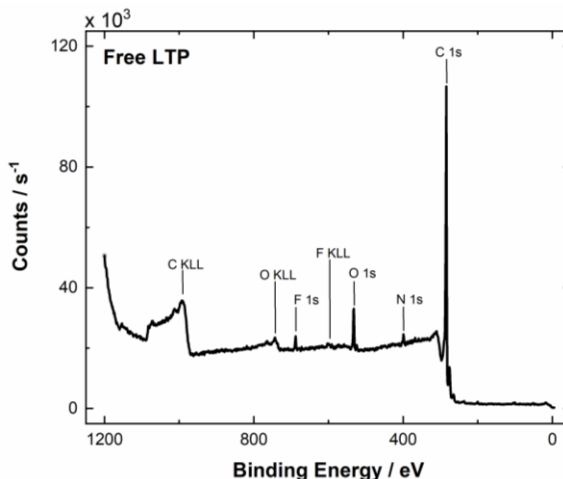
The primary photoelectron emission peaks of the Mg Kα source spectra are nearly identical to those observed in the Al Kα source spectra. The spectra of the M $3d$ region of the **Ce(LTP)** complex was essentially unchanged and peaks assignable to the presence both a Ce(III) and Ce(IV) complex were still observed in the Mg-source data (**Figure 2.9**). The features of the **Sm(LTP)** complex for the Mg Kα source M $3d$ region were again very similar to the features seen in the Al Kα source spectra; however, it was observed that the peak corresponding to the M $3d_{5/2}$ in the Mg Kα source spectra did not have an additional shake-up feature at 1115 eV like in the Al Kα source spectra (**Figure 2.10**). This suggests that the shake-up feature at 1115 eV is not intrinsic to a simple photoelectron emission process of Sm. Further differences in the **Sm(LTP)** Mg Kα source spectra can be seen in the M $4d$ region (**Figure 2.11**). In the Al Kα source data, there is a feature present in the M $4d$ region centered around 154 eV and 134 eV; however, those features are absent in the Mg Kα source data, suggesting shifted Auger signals. This behavior was also observed in the case of the **Eu(LTP)** complex M
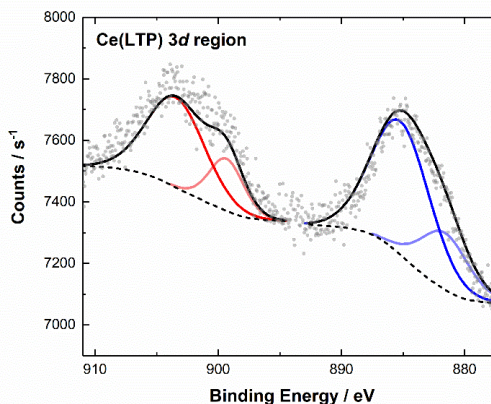

Figure 2.9. Spectrum of the M $3d$ region of the immobilized **Ce(LTP)** complex utilizing the Mg Kα source. Legend: gray dots: data; dashed black lines: fitting background; dark blue lines: Ce(IV) M $3d_{5/2}$ peak fit; dark red lines: Ce(IV) M $3d_{3/2}$ peak fit (constrained to 2/3 area with respect to M $3d_{5/2}$); light blue lines: Ce(III) M $3d_{5/2}$ peak fit; light red lines: Ce(III) M $3d_{3/2}$ peak fit; continuous black line: overall fit.
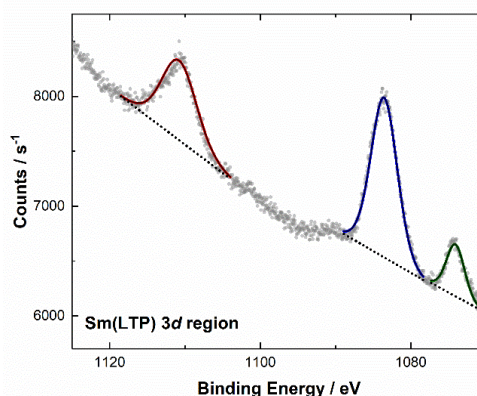

Figure 2.10. Spectrum of the M $3d$ region of the immobilized **Sm(LTP)** complex utilizing the Mg Kα source. Legend: gray dots: data; dashed black lines: fitting background; blue lines: M $3d_{5/2}$ peak fit; red lines: M $3d_{3/2}$ peak fit (constrained to 2/3 area with respect to M $3d_{5/2}$); green lines: shake-up and shake-down peaks fit; continuous black line: overall fit.

4*d* region (**Figure 2.12**). In the Al-source data, additional peaks in the M 4*d* regions were necessary to achieve proper fitting of the M 4d region. In a similar fashion, the features centered around 143 eV and 136 eV are absent in the M 4d region of the Mg-source data, indicating that these additional features were due to Auger processes that could be shifted by adjusting the source ionization energy. Unfortunately, the higher background energy of the achromatic Mg X-ray source obscures most of the interpretation related to the M 3*d* regions of the **Nd(LTP)** and the **Eu(LTP)** and so the data could not be reliably evaluated (**Appendix A**, **Figures A14** and **A15**).

Figure 2.11. Spectrum of the M 4*d* region of the immobilized **Sm(LTP)** complex utilizing the Mg Kα source. Legend: gray dots: data; dashed black lines: fitting background; blue lines: M $4d_{5/2}$ peak fit; red lines: M $3d_{3/2}$ peak fit (constrained to 2/3 area with respect to M $3d_{5/2}$); continuous black line: overall fit.
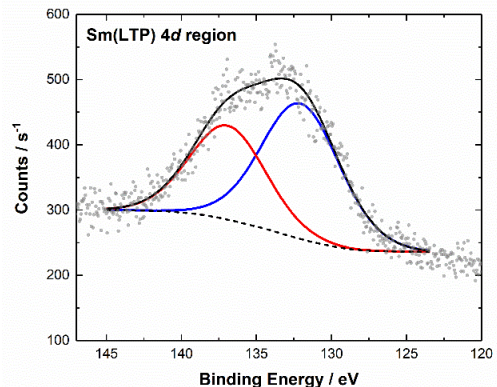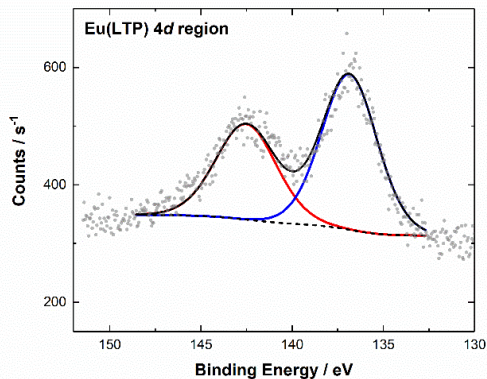

Figure 2.12. Spectrum of the M 4*d* region of the immobilized **Eu(LTP)** complex utilizing the Mg Kα source. Legend: gray dots: data; dashed black lines: fitting background; blue lines: M $4d_{5/2}$ peak fit; red lines: M $4d_{3/2}$ peak fit (constrained to 2/3 area with respect to M $3d_{5/2}$); continuous black line: overall fit.

2.5 *Cyclic Voltammetry*

Cyclic voltammetry (CV) studies were used to probe the electrochemical properties of the **Ce(LTP)** complex on the surface. The cerium complex was selected for this study due to the clean, reversible nature of Ce(IV/III) couples that is well-documented in the literature.[73-74] Previous work on the analogous **Ce(LTO)** complex showed the presence of a quasi-reversible Ce(IV/III) couple at –0.34 V versus Fc$^{+/0}$. Since the structure and coordination chemistry of the **Ce(LTP)** and **Ce(LTO)** complexes are nearly

Figure 2.13. Cyclic voltammogram of the **Ce(LTP)** complex on a functionalized Ketjen black electrode overlaid with a blank Ketjen black electrode. Electrochemical experiments were carried out at 100 mV/s in 0.1 M TBAPF$_6$ in CH$_3$CN. The working electrode was the functionalized Ketjen black electrode, platinum was used as the counter electrode, and a silver electrode was used as a reference electrode.

isomeric, the expectation was that the **Ce(LTP)** complex would exhibit a Ce(IV/III) couple at a similar potential. Voltammograms of the electrodes functionalized with **Ce(LTP)** displayed a single quasi-reversible redox event at –0.19 V versus Fc$^{+/0}$ which can be readily assigned to the Ce(IV/III) couple (**Figure 2.13**). The resulting 150 mV difference in the Ce(IV/III) redox potentials for the **Ce(LTP)** and **Ce(LTO)** can be attributed to the sensitivity of the Ce(IV/III) redox event to substitution effects on the aromatic rings.[73] The ligand framework of the **Ce(LTO)** complex is decorated with methyl-substituents on the aromatic rings while the supporting **Ce(LTP)** framework contains no substituents on the aromatic rings. Methyl substituents are well-known to possess electron donating properties in aromatic systems;[75-76] therefore, removing the methyl groups from the aromatic rings results in a cerium metal center that is less electron-rich, causing the Ce(IV/III) couple of **Ce(LTP)** to shift to a more oxidizing potential.
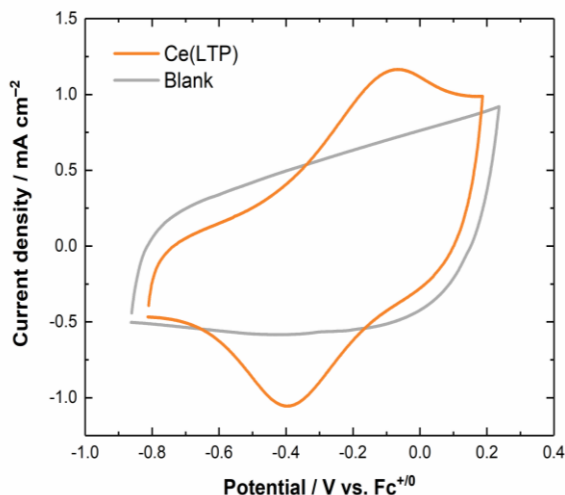
Further analysis of the electrochemical properties of the **Ce(LTP)** complex sought to confirm that the electrochemical profile matched with the characteristics for a molecule confined to a surface. One electrochemical feature that is indicative of an immobilized species is an anodic and cathodic peak separation (ΔE_p) of 0 V at all scan rates;[50, 76-78] however, the resulting cyclic voltammetry of the **Ce(LTP)** deviates from this ideal behavior (**Figure 2.14**). The values for ΔE_p for the **Ce(LTP)** complex see quite large peak-to-peak separations, even at slow scan rates (200 mV at 25 mV/s), and gradually increase with increasing scan rate. These deviations from ideality have been noted for several immobilized complexes[79-86] and have been attributed to a multitude of factors, such as electrostatic interactions between proximal electroactive species and slow interfacial electron transfer between the electrode surface and the immobilized species. For this work, slow electron transfer between the **Ce(LTP)** and electrode surface has been determined as the predominant cause for the large ΔE_p values and will be discussed later in this chapter when the electrochemical profile of the **Ce(LTP)** and **Ce(LTO)** complexes are analyzed using Laviron's method.
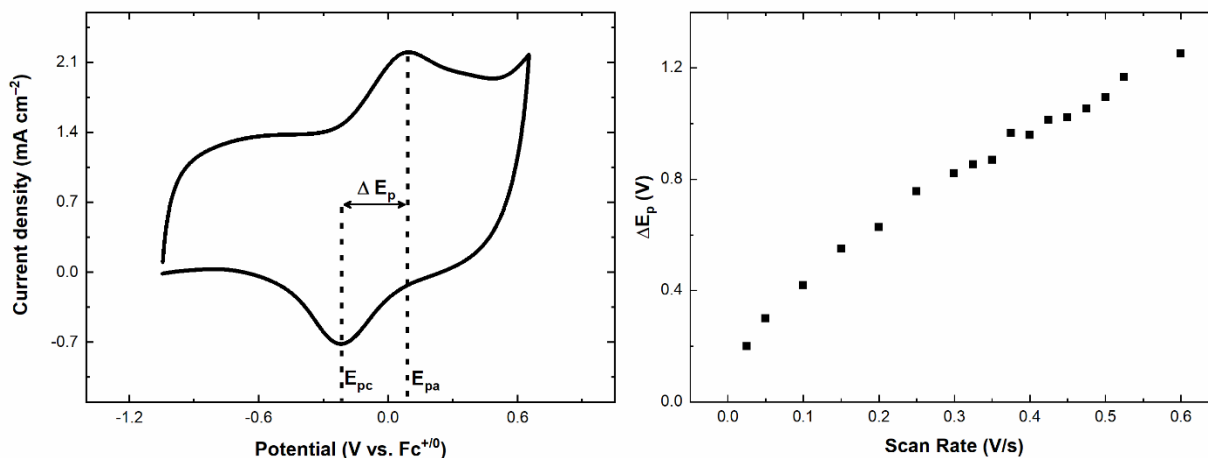

Figure 2.14. Cyclic voltammetry data of the **Ce(LTP)** complex displaying changes in the value for ΔE_p as a function of scan rate. The left panel utilizes the cyclic voltammogram for **Ce(LTP)** to depict how the value for ΔE_p is obtained. The right panel is the plotted data of the change in ΔE_p as a function of increasing scan rate. All electrochemical measurements were performed in 0.1 M TBAPF$_6$ in CH$_3$CN. The functionalized Ketjen black electrode was utilized as the working electrode with a Pt counter electrode and a Ag$^{+/0}$ reference electrode.

Cyclic voltammetry studies at variable scan rates can also be used to probe the reversibility and the surface confinement of the **Ce(LTP)** complex. For a homogeneous system, cyclic voltammetry shows a linear relationship between peak current and the square root of scan rate, as demonstrated by the Randles-Sevcik equation, **Equation 2.1** (where i_p is the peak current, n is the number of electrons, F is Faraday's constant, A is the area of the electrode surface, C is the concentration of the compound in solution, v is the scan rate, D is the diffusion coefficient, and R and T are the ideal gas constant and temperature at which the experiment was performed).[76] In a system where the complex has been attached to the electrode surface, diffusional considerations are negated and **Equation 2.2** can be derived from the original Randles-Sevcik equation given these parameters (where i_p is the peak current, n is the number of electrons, F is Faraday's constant, Γ is the surface concentration, A is the area of the electrode, v is the scan rate, and R and T are the ideal gas constant and temperature at which the experiment was run).[76, 87] These differences stem from the fact that in homogenous systems a complex must diffuse to the electrode surface, limiting the total current passed during an electrochemical sweep.

Equation 2.1 $\qquad i_p = 0.4463 nFAC \left(\frac{nFvD}{RT} \right)^{\frac{1}{2}}$

Equation 2.2 $\qquad i_p = \frac{n^2 F^2 \Gamma A v}{4RT}$

While there is significant current generated that can be assigned to the Ce(IV/III) couple, there is also a relatively large background current from the Ketjen black electrode coating. Due to the high surface area of the Ketjen black electrode material, the capacitance of each electrode is relatively large, corresponding to a current density of ≥ 1 mA/cm^2 at 100 mV/s. This excess capacitance is problematic for accurate electrochemical analysis
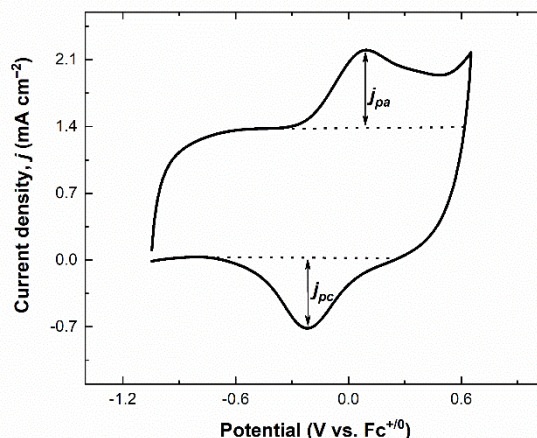

Figure 2.15. A depiction of how the values for the anodic and cathodic peak current densities, **j$_p$**, were determined for all scan rates.

since current related to capacitance also varies linearly with scan rate; therefore, proper background subtraction is necessary to obtain reliable values for peak current densities (**Figure 2.15**). Once background subtracted, the peak current for the anodic and cathodic scans of the Ce(IV/III) couple could be obtained from the voltammetry measurements and are plotted in **Figure 2.16**. In agreement with the theoretical model for a species immobilized on an electrode surface, the cyclic voltammetry studies at variable scan rates reveal a linear relationship between the peak
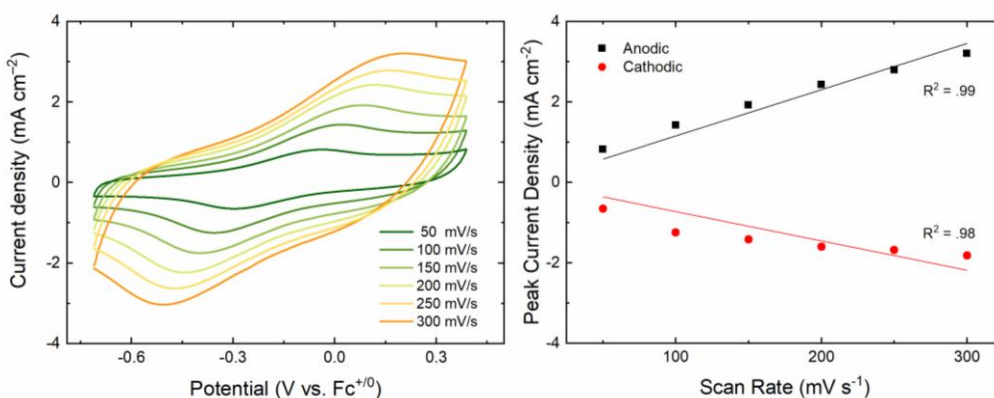

Figure 2.16. Voltammograms showing scan rate dependence of the **Ce(LTP)** complex on a functionalized Ketjen black electrode (left). The corresponding plot of peak current densities for the anodic and cathodic scans versus scan rate is plotted on the right. The line of best fit has been fit through zero for both the anodic and cathodic branches in agreement with theory. Electrochemical experiments were carried out in 0.1 M TBAPF$_6$ in CH$_3$CN. The working electrode was Ketjen black, a platinum wire was used as the counter electrode, and a silver electrode was used as the reference electrode.

current and scan rate for the **Ce(LTP)** complex.
Additional analysis of the cyclic voltammetry
can also provide information on the
reversibility of the Ce(IV/III) redox process.
Integration of the current for the anodic and
cathodic peaks was done using **Equation 2.3**,
where Q is the total charge, *n* is the number of
electrons, F is Faraday's constant, A is the area
of the electrode, and Γ is the surface
concentration, in order to validate the
stoichiometry of the redox event. Since the

Figure 2.17. Plot of the calculated ratios of the anodic
and cathodic peak areas as a function of scan rate. The
expected ratio for the 1 electron process that occurs in
the **Ce(LTP)** complex is 1:1, indicated by the
horizontal dotted line.

Ce(IV/III) couple is a 1 electron process, the expected ratio of the integrated anodic and cathodic

peaks is 1:1. **Figure 2.17** demonstrates the ratio of the integrated anodic and cathodic peaks as a

function of varying scan rate. The data obtained indicate a 1:1 ratio between the anodic and

cathodic peak areas at all scan rates, suggesting that the Ce(IV/III) redox process is not affected

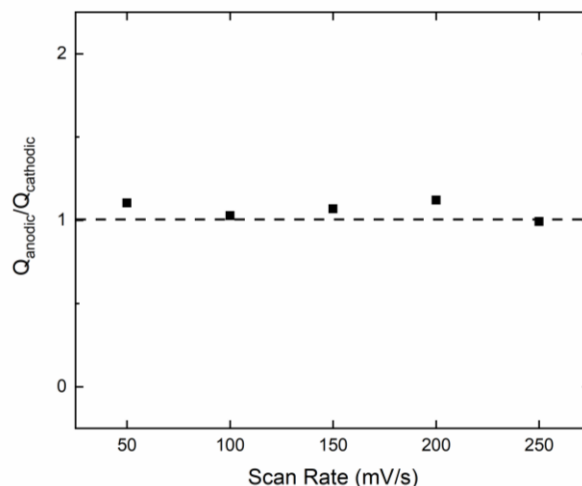by any follow-up chemical reactions after oxidation or reduction.

$$\text{Equation 2.3} \quad Q = nFA\Gamma$$

From the collective data obtained from electrochemical experiments, we concluded that

Ce(LTP) was successfully immobilized. The scan rate dependence studies indicated the successful

immobilization of the **Ce(LTP)** complex while the integration of the anodic and cathodic peak

currents revealed a 1:1 ratio free of follow-up chemical reactions. With the complete

electrochemical profile of the **Ce(LTP)** complex determined, the surface and electrochemical

properties of the **Ce(LTP)** and **Ce(LTO)** complexes could be examined and compared.

56

2.5.1 *Stability Studies Utilizing Cyclic Voltammetry*

Previous studies of the **Ce(LTO)** complex revealed that the current from the Ce(IV/III) redox process significantly diminished over the course of an electrochemical experiment; however, quantification of this process was never pursued. To explain this surface behavior, it was hypothesized that the pyrene groups of the **LTO** framework preferred to interact with one another rather than participating in non-covalent interactions with the surface. The **LTP** framework was designed as an attempt to avoid the suspected aggregation of pyrene groups, resulting in increased surface stability. To compare the surface stability of the **Ce(LTP)** and **Ce(LTO)** complexes, cyclic voltammetry was used. By taking voltammograms at given time intervals, one can easily integrate the current from the voltammetry to calculate surface concentration as a function of time. This method has been widely used in the literature due to the straightforward nature of the measurements and the data work-up. Coated electrodes were functionalized with either **Ce(LTP)** or **Ce(LTO)** and fixed into a special set-up for immobilized electrochemistry (**Scheme 2.9**). A solution of the electrolyte was then added to the electrochemical cell and measurements were taken at designated time intervals. By obtaining the total charge (Q) by integrating the voltammograms, the surface coverage could be calculated using the previously mentioned **Equation 2.3**. The fractional coverage plots for the **Ce(LTO)** and **Ce(LTP)** complexes are shown in **Figure 2.18**, where Γ_0 is the initial surface coverage and Γ_t is the coverage determined at time t. Within the first hour, the Ce(IV/III) signal of the **Ce(LTO)** complex significantly diminishes to 30% of its
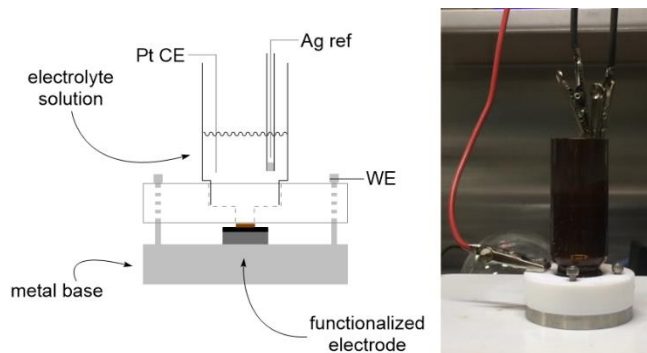
Scheme 2.9. Diagram of the immobilized set-up used for electrochemical experiments. The diagram in the left panel is credited to Dr. Davide Lionetti.

57

original surface coverage. Surprisingly, the **Ce(LTP)** complex retains 60% of its initial surface coverage after the first hour. Over the course of the experiment, the Ce(IV/III) signal for the **Ce(LTO)** complex was completely lost after three hours, indic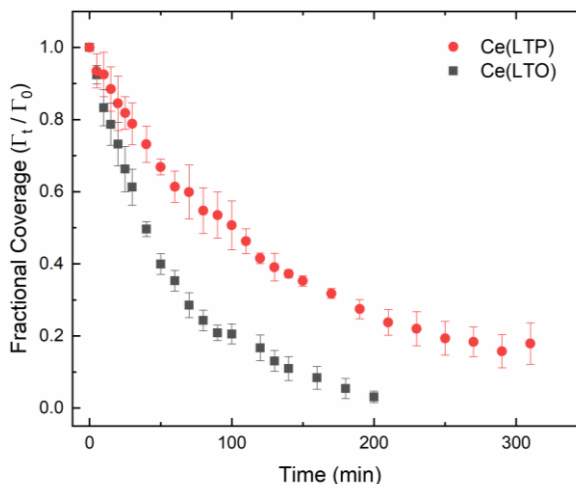ating all of the **Ce(LTO)** had been lost from the surface. However, the data obtained for the **Ce(LTP)** complex plateaus at 20% the original surface concentration after the four hour mark, suggesting that an equilibrium surface

Figure 2.18. Fractional coverage plots for the **Ce(LTP)** (red) and **Ce(LTO)** (grey) complexes. Electrochemical experiments were run in triplicate to determine error bars. Each electrode was submerged in 2 mL of 0.1 M TBAPF$_6$ in CH$_3$CN. The scan rate for all measurements was 100 mV/s.

concentration is being established. Many recent studies have examined the relationship between the number of pyrene groups and the resulting surface stability,[80, 88] but this is the first example of a study that examines the influence of pyrene placement on surface stability for analogous complexes.

2.5.2 *Laviron Analysis and Rates of Electron Transfer*

Given the observed differences in surface stability, follow up electrochemical work utilized the Laviron formulism to probe for potential differences in the intrinsic electronic properties of the **Ce(LTO)** and **Ce(LTP)** complexes.[89] The Laviron method is well established in the literature and has been used to examine the properties of redox-active metal complexes, catalytic systems, and different types of surfaces.[79-83, 88] To extract values for k_{ET}, this method utilizes the Butler-Volmer kinetics approach and only requires overpotentials (η) for analysis. By examining the separation

58

of the cathodic and anodic peak potentials (ΔE_p) at varying scan rates, the k_{ET} value for the redox

process can be determined using the following equations:

$$\textbf{Equation 2.3} \qquad E_{p,c} = E^{\circ\prime} - \frac{2.3RT}{\alpha nF} \log \frac{\alpha nF\upsilon}{RTk_{ET}}$$

$$\textbf{Equation 2.4} \qquad E_{p,a} = E^{\circ\prime} - \frac{2.3RT}{(1-\alpha)nF} \log \frac{(1-\alpha)nF\upsilon}{RTk_{ET}}$$

where $E_{p,a}$ is the anodic peak potential, $E_{p,c}$ is the cathodic peak potential, $E^{\circ\prime}$ is the formal

Ce(IV/III) potential of the complex of interest, α is the electron-transfer coefficient, υ is the critical

scan rate, R is the ideal gas constant, T is temperature, F is Faraday's constant, and n is the number

of electrons transferred. By plotting the E_p–$E^{\circ\prime}$ values of the anodic and cathodic branches against

the log of scan rate (**Figure 2.19**), the critical scan rates, υ_a, and υ_c can be determined by solving
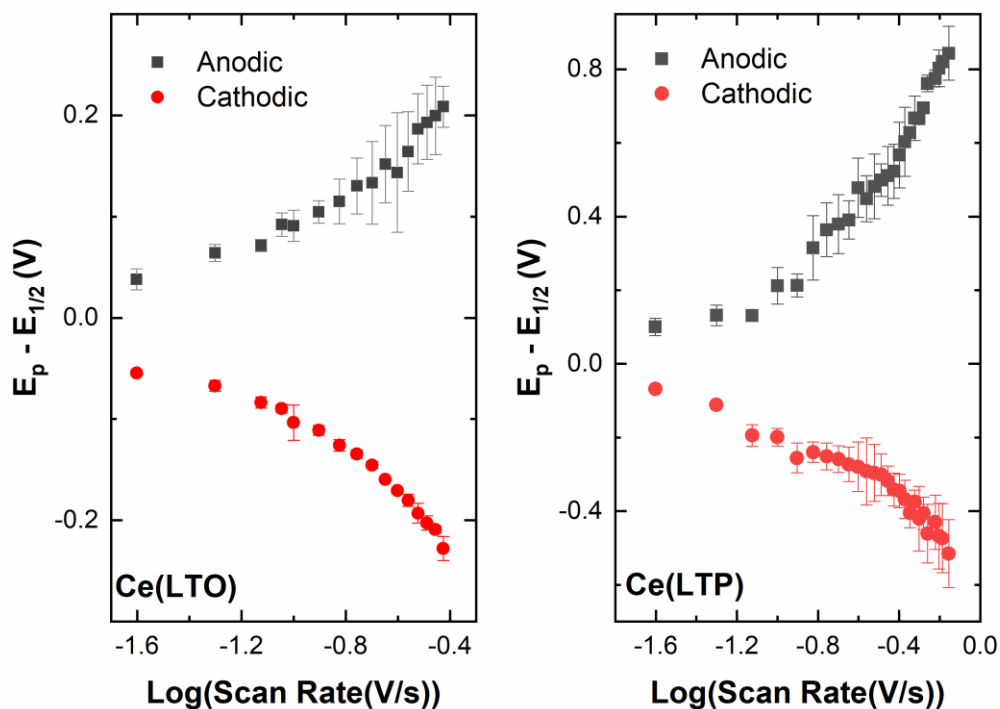

Figure 2.19. Laviron analysis plots for the **Ce(LTO)** (left) and **Ce(LTP)** (right) complexes. Electrochemical experiments were run in triplicate to determine error bars. All electrochemical experiments were run in 0.1 M TBAPF$_6$ in CH$_3$CN.

for the x-intercepts of the linear portion of the plots where $\eta > 100$ mV. The resulting symmetry of the anodic and cathodic branches in **Figure 2.19** and the similarities in their determined slopes is indicative of an electron-transfer coefficient value of approximately 0.5 ($\alpha \approx 0.5$), as expected from theory.[76]

On the basis of the data shown in **Figure 2.19**, the average k_{ET} values for the **Ce(LTO)** and **Ce(LTP)** complexes was determined to be 1.3 ± 0.4 s^{-1} and 2.2 ± 0.8 s^{-1} respectively. These k_{ET} values are lower than those previously reported for some transition metal tripodal complexes,[82] but are on the same order of magnitude as other reported immobilized metal complexes.[79] These results could be attributed to the high surface area and capacitance of the Ketjen black coating that makes interfacial electron transfer between the surface and complex slow.[81, 89] In spite of this, the k_{ET} values of the complexes are within error of one another and indicate that the interactions between the Ketjen black surface and the **Ce(LTO)** and **Ce(LTP)** complexes are similar. This result was anticipated since the **Ce(LTO)** and **Ce(LTP)** complexes are structurally similar and it was expected that they would interact in a similar fashion with the electrode surface.

2.6 *Conclusion*

This Chapter reports the complete synthesis and characterization of a new set of tripodal lanthanide complexes that are capable of noncovalent immobilization on carbon electrode surfaces. NMR studies reveal only one set of peaks for these tripodal **M(LTP)** complexes, indicative of C_{3v} symmetry in solution on the NMR timescale. This behavior is also observed in the NMR spectra for the previously reported **M(LTO)** complexes. After immobilization of the **M(LTP)** complexes, full characterization by XPS analysis supports the retention of molecular fidelity on the surface. In agreement with the stoichiometry of the **M(LTP)** complexes, integration

and normalization of the observed metal $3d$ and nitrogen $1s$ regions indicated a 1:7 ratio. The complete electrochemical characterization of the **Ce(LTP)** complex has also been provided in this Chapter, where the Ce(IV/III) couple is observed at -0.34 V versus the Fc$^{+/0}$ couple. Scan rate dependence studies show a direct linear relationship between the peak current densities and the scan rate, in agreement with the relationship expected for a surface-immobilized redox couple.

Electrochemical analysis of the **Ce(LTP)** and **Ce(LTO)** complexes shows significant differences in their surface stabilities. Within the first hour, only 30% of the **Ce(LTO)** complex remains on the electrode surface, while the **Ce(LTP)** complex retains 60% of its original surface loading. Further electrochemical work utilizing the Laviron formalism determined that the k_{ET} values for the **Ce(LTP)** and **Ce(LTO)** complexes were 2.2 ± 0.8 s^{-1} and 1.3 ± 0.4 s^{-1}, respectively. The similarity of the k_{ET} values indicates that both complexes interact with the carbon electrode surface in a similar fashion. The results discussed in this Chapter support that properties relevant to surface immobilization, such as stability and electron transfer, can be influenced by ligand design.

2.7 *References*

1.   Wang, Q.-X.; Xue, S.-F.; Chen, Z.-H.; Ma, S.-H.; Zhang, S.; Shi, G.; Zhang, M., *Biosens. Bioelectron.* **2017,** *94*, 388-393.

2.   Zhou, Z.; Wang, Q.; Wang, J.; Zhang, C. C., *Carbon* **2015,** *93*, 671-680.

3.   Rinehart, J. D.; Long, J. R., *Chem. Sci.* **2011,** *2*, 2078-2085.

4.   Woodruff, D. N.; Winpenny, R. E. P.; Layfield, R. A., *Chem. Rev.* **2013,** *113*, 5110-5148.

5.   Shibasaki, M.; Yoshikawa, N., *Chem. Rev.* **2002,** *102*, 2187-2210.

6.   Qiao, Y.; Schelter, E. J., *Acc. Chem. Res.* **2018,** *51*, 2926-2936.

7.   Halter, D. P.; Palumbo, C. T.; Ziller, J. W.; Gembicky, M.; Rheingold, A. L.; Evans, W. J.; Meyer, K., *J. Am. Chem. Soc.* **2018,** *140*, 2587-2594.

8.   Rosser, T. E.; Windle, C. D.; Reisner, E., *Angew. Chem.* **2016,** *55*, 7388-7392.

9.   Reuillard, B.; Le Goff, A.; Cosnier, S., *Chem. Commun.* **2014,** *50*, 11731-11734.

10.   Bullock, R. M.; Das, A. K.; Appel, A. M., *Chem. Eur. J.* **2017,** *23*, 7626-7641.

11.   Wilkinson, G.; Birmingham, J. M., *J. Am. Chem. Soc.* **1954,** *76*, 6210-6210.

12.   Birmingham, J. M.; Wilkinson, G., *J. Am. Chem. Soc.* **1956,** *78*, 42-44.

13.   Fischer, R. D.; Fischer, H., *J. Organomet. Chem.* **1965,** *4*, 412-414.

14.   Fischer, R. D.; Fischer, H., *J. Organomet. Chem.* **1967,** *8*, 155-175.

15.   Mares, F.; Hodgson, K.; Streitwieser, A., *J. Organomet. Chem.* **1970,** *24*, C68-C70.

16.   Mares, F.; Hodgson, K. O.; Streitwieser, A., *J. Organomet. Chem.* **1971,** *28*, C24-C26.

17.   DeKock, C. W.; Ely, S. R.; Hopkins, T. E.; Brault, M. A., *Inorg. Chem.* **1978,** *17*, 625-631.

18.   Bottrill, M.; Kwok, L.; Long, N. J., *Chem. Soc. Rev.* **2006,** *35*, 557-571.

19. Chakhmouradian, A. R.; Wall, F., *Elements* **2012,** *8*, 333-340.

20. Feng, J.; Zhang, H., *Chem. Soc. Rev.* **2013,** *42*, 387-410.

21. Ritter, S. K., A Whole New World for Rare Earths. *Chem. Eng. News* August 2017, pp 30-34.

22. Van Gosen, B. S. V., P. L.; Long, K. R.; Gambogi, J.; Seal II, R. R. *The Rare-Earth Elements- Vital to Modern Technologies and Lifestyles*, 2014.

23. Bünzli, J.-C. G., *Chem. Rev.* **2010,** *110*, 2729-2755.

24. Skovran, E.; Martinez-Gomez, N. C., *Science* **2015,** *348*, 862-863.

25. Nielsen, L. G.; Junker, A. K. R.; Sørensen, T. J., *Dalton Trans.* **2018,** *47*, 10360-10376.

26. Molloy, J. K.; Philouze, C.; Fedele, L.; Imbert, D.; Jarjayes, O.; Thomas, F., *Dalton Trans.* **2018**.

27. Shannon, R., *Acta Crystallogr. A* **1976,** *32*, 751-767.

28. Helm, L.; Merbach, A. E., *Chem. Rev.* **2005,** *105*, 1923-1960.

29. Sørensen, T. J.; Faulkner, S., *Acc. Chem. Res.* **2018,** *51*, 2493-2501.

30. Leoncini, A.; Huskens, J.; Verboom, W., *Chem. Soc. Rev.* **2017,** *46*, 7229-7273.

31. Comby, S.; Surender, E. M.; Kotova, O.; Truman, L. K.; Molloy, J. K.; Gunnlaugsson, T., *Inorg. Chem.* **2014,** *53*, 1867-1879.

32. Hu, L.; Xu, G., *Chem. Soc. Rev.* **2010,** *39*, 3275-3304.

33. Moore, E. G.; Samuel, A. P. S.; Raymond, K. N., *Acc. Chem. Res.* **2009,** *42*, 542-552.

34. Sessoli, R.; Powell, A. K., *Coord. Chem. Rev.* **2009,** *253*, 2328-2341.

35. Layfield, R. A., *Organometallics* **2014,** *33*, 1084-1099.

36. Kuda-Wedagedara, A. N. W.; Wang, C.; Martin, P. D.; Allen, M. J., *J. Am. Chem. Soc.* **2015,** *137*, 4960-4963.

37.   de Bettencourt-Dias, A.; Rossini, J. S. K., *Inorg. Chem.* **2016,** *55*, 9954-9963.

38.   Xu, J.; Shen, X.-K.; Jia, L.; Cao, J.-L.; Wang, Y.; Zhao, X.-L.; Bi, N.; Guo, S.-L.; Ma, T.-Y., *J. Mater. Chem. B* **2019**.

39.   Gago, S.; Pillinger, M.; Sá Ferreira, R. A.; Carlos, L. D.; Santos, T. M.; Gonçalves, I. S., *Chem. Mater.* **2005,** *17*, 5803-5809.

40.   Lenaerts, P.; Driesen, K.; Van Deun, R.; Binnemans, K., *Chem. Mater.* **2005,** *17*, 2148-2154.

41.   Gago, S.; Fernandes, J. A.; Rainho, J. P.; Sá Ferreira, R. A.; Pillinger, M.; Valente, A. A.; Santos, T. M.; Carlos, L. D.; Ribeiro-Claro, P. J. A.; Gonçalves, I. S., *Chem. Mater.* **2005,** *17*, 5077-5084.

42.   Mercier, D.; Leconte, N.; Méthivier, C.; Suzenet, F.; Guillaumet, G.; Wuillaume, A.; Pradier, C.-M., *Phys. Chem. Chem. Phys.* **2010,** *12*, 6099-6106.

43.   Lionetti, D.; Day, V. W.; Blakemore, J. D., *Dalton Trans.* **2017,** *46*, 11779-11789.

44.   Cozzi, P. G., *Chem. Soc. Rev.* **2004,** *33*, 410-421.

45.   Molloy, J. K.; Philouze, C.; Fedele, L.; Imbert, D.; Jarjayes, O.; Thomas, F., *Dalton Trans.* **2018,** *47*, 10742-10751.

46.   Chen, H.; Yang, H.; Xu, W.; Tan, Y., *RSC Adv.* **2013,** *3*, 13311-13317.

47.   Fennie, M. W.; DiMauro, E. F.; O'Brien, E. M.; Annamalai, V.; Kozlowski, M. C., *Tetrahedron* **2005,** *61*, 6249-6265.

48.   Chirakul, P.; Hampton, P. D.; Bencze, Z., *J. Org. Chem.* **2000,** *65*, 8297-8300.

49.   Bradley, D. C.; Ghotra, J. S.; Hart, F. A., *J. Chem. Soc., Dalton Trans.* **1973**, 1021-1023.

50.   McCreery, R. L., *Chem. Rev.* **2008,** *108*, 2646-2687.

51.	Blakemore, J. D.; Gupta, A.; Warren, J. J.; Brunschwig, B. S.; Gray, H. B., *J. Am. Chem. Soc.* **2013,** *135*, 18288-18291.

52.	Kamitaka, Y.; Tsujimura, S.; Kano, K., *Chem. Lett.* **2007,** *36*, 218-219.

53.	Briggs, D., *Handbook of X-ray and ultraviolet photoelectron spectroscopy*. Heyden: London, 1977.

54.	Hendrickson, D. N.; Hollander, J. M.; Jolly, W. L., *Inorg. Chem.* **1969,** *8*, 2642-2647.

55.	Uwamino, Y.; Ishizuka, T.; Yamatera, H., *J. Electron. Spectrosc. Relat. Phenom.* **1984,** *34*, 67-78.

56.	Bernhardt, P. V.; Flanagan, B. M.; Riley, M. J.; Wood, B. J., *J. Electron. Spectrosc. Relat. Phenom.* **2002,** *124*, 73-77.

57.	Hillebrecht, F. U.; Fuggle, J. C., *Phys. Rev. B* **1982,** *25*, 3550-3556.

58.	Orchard, A. F., *Handbook of X-ray and ultraviolet photoelectron spectroscopy*. Heyden: London, 1977.

59.	Kaltsoyannis, N.; Scott, P., *The f elements*. Oxford University Press: New York, 1999.

60.	Hughes, I. D.; Däne, M.; Ernst, A.; Hergert, W.; Lüders, M.; Poulter, J.; Staunton, J. B.; Svane, A.; Szotek, Z.; Temmerman, W. M., *Nature* **2007,** *446*, 650.

61.	Shirley, D. A., *Phys. Rev. B* **1972,** *5*, 4709-4714.

62.	Signorelli, A. J.; Hayes, R. G., *Phys. Rev. B* **1973,** *8*, 81-86.

63.	Krawicz, A.; Yang, J.; Anzenberg, E.; Yano, J.; Sharp, I. D.; Moore, G. F., *J. Am. Chem. Soc.* **2013,** *135*, 11861-11868.

64.	Wagner, C. D.; Taylor, J. A., *J. Electron. Spectrosc. Relat. Phenom.* **1980,** *20*, 83-93.

65.	Mercier, F.; Alliot, C.; Bion, L.; Thromat, N.; Toulhoat, P., *J. Electron. Spectrosc. Relat. Phenom.* **2006,** *150*, 21-26.

66. Bêche, E.; Charvin, P.; Perarnau, D.; Abanades, S.; Flamant, G., *Surf. Interface Anal.* **2008,** *40*, 264-267.

67. Romeo, M.; Bak, K.; El Fallah, J.; Le Normand, F.; Hilaire, L., *Surf. Interface Anal.* **1993,** *20*, 508-512.

68. Crecelius, G.; Wertheim, G. K.; Buchanan, D. N. E., *Phys. Rev. B* **1978,** *18*, 6519-6524.

69. Herbst, J. F.; Burkstrand, J. M.; Wilkins, J. W., *Phys. Rev. B* **1980,** *22*, 531-533.

70. Berthou, H.; Jørgensen, C. K.; Bonnelle, C., *Chem. Phys. Lett.* **1976,** *38*, 199-206.

71. Tatsumi, K.; Tsutsui, M.; Beall, G. W.; Mullica, D. F.; Milligan, W. O., *J. Electron. Spectrosc. Relat. Phenom.* **1979,** *16*, 113-118.

72. Scofield, J. H., *J. Electron. Spectrosc. Relat. Phenom.* **1976,** *8*, 129-137.

73. Piro, N. A.; Robinson, J. R.; Walsh, P. J.; Schelter, E. J., *Coord. Chem. Rev.* **2014,** *260*, 21-36.

74. Bogart, J. A.; Lewis, A. J.; Medling, S. A.; Piro, N. A.; Carroll, P. J.; Booth, C. H.; Schelter, E. J., *Inorg. Chem.* **2013,** *52*, 11600-11607.

75. Anslyn, E. V. D., D. A., *Modern Physical Organic Chemistry*. University Science Books: Mill Valley, 2006.

76. Bard, A. J.; Faulkner, L. R., *Electrochemical Methods: Fundamentals and Applications*. 2 ed.; John Wiley & Sons: New York, 2001.

77. Zhou, Y.; Zhi, J.; Zou, Y.; Zhang, W.; Lee, S.-T., *Anal. Chem.* **2008,** *80*, 4141-4146.

78. Ambrosi, A.; Chua, C. K.; Bonanni, A.; Pumera, M., *Chem. Rev.* **2014,** *114*, 7150-7188.

79. Lydon, B. R.; Germann, A.; Yang, J. Y., *Inorg. Chem. Frontiers* **2016,** *3*, 836-841.

80. Kohmoto, M.; Ozawa, H.; Yang, L.; Hagio, T.; Matsunaga, M.; Haga, M.-a., *Langmuir* **2016,** *32*, 4141-4152.

81. Hanna, C. M.; Sanborn, C. D.; Ardo, S.; Yang, J. Y., *ACS Appl. Mater. Interfaces* **2018,** *10*, 13211-13217.

82. Mann, J. A.; Rodríguez-López, J.; Abruña, H. D.; Dichtel, W. R., *J. Am. Chem. Soc.* **2011,** *133*, 17614-17617.

83. Mann, J. A.; Dichtel, W. R., *ACS Nano* **2013,** *7*, 7193-7199.

84. Hoarau, M.; Badieyan, S.; Marsh, E. N. G., *Org. Biomol. Chem.* **2017,** *15*, 9539-9551.

85. Reuillard, B.; Ly, K. H.; Rosser, T. E.; Kuehnel, M. F.; Zebger, I.; Reisner, E., *J. Am. Chem. Soc.* **2017,** *139*, 14425-14435.

86. Li, T.-T.; Qian, J.; Zhou, Q.; Lin, J.-L.; Zheng, Y.-Q., *Dalton Trans.* **2017,** *46*, 13020-13026.

87. Prodromidis, M. I.; Florou, A. B.; Tzouwara-Karayanni, S. M.; Karayannis, M. I., *Electroanal.* **2000,** *12*, 1498-1501.

88. Ozawa, H.; Katori, N.; Kita, T.; Oka, S.; Haga, M.-a., *Langmuir* **2017,** *33*, 11901-11910.

89. Laviron, E., *J. Electroanal. Chem.* **1979,** *101*, 19-28.

Chapter 3

Electrochemical Properties of Molecular Uranyl Complexes on Carbon Electrodes

3.1 *Abstract*

The extensive use of fossil fuels has contributed significantly to the onset of rapid anthropogenic climate change.[1] To reduce the rate of global climate change, scientists across disciplines are working to develop alternative energy strategies that do not require emission of greenhouse gasses like carbon dioxide (CO_2). While significant advancements have been made in the field of renewable energy, many technologies rely on intermittent sources such as solar and wind energy and are currently unable to meet energy demands.[2-3] One energy strategy that has existed since the mid-20th century and can meet ever-increasing energy needs without significant greenhouse gas emission is nuclear energy.

Despite nuclear energy's ability to generate large amounts of energy from small quantities of fuel, its implementation has been hobbled by pervasively negative public opinions. Specifically, the long-term storage of highly radioactive wastes from nuclear power plants has been of significant concern. To reduce the volume of radioactive waste generated during the nuclear fuel cycle, much of the work in *f*-element science is focused on developing methods to selectively and efficiently extract highly radioactive components from aqueous solutions. Additional work focuses on methods to capture and separate uranium from waste streams, as significant quantities of fissile [235]U remain in fuel components at the end of their useful lifetime. Thus, recycling or reprocessing of uranium from waste back into the nuclear fuel cycle is possible; however, improved chemistry for the handling of this difficult element is needed. This chapter focuses on the synthesis and electrochemical profiles of surface immobilized uranyl [$(UO_2)^{2+}$] complexes. The work presented in this chapter serves as the first example, to the best of our knowledge, of utilizing Schiff base ligand frameworks for immobilization of $(UO_2)^{2+}$ on electroactive substrates. Eventually, such

structures could serve in systems for selective extraction of uranyl ions from solutions also containing trivalent lanthanide ions and other actinides.

3.2 *Introduction*

As of 2017, roughly 80% of the energy produced in the United States came from non-renewable, carbon-based sources such as coal, oil, and gas (**Figure 3.1**).[3] Although the use of carbon-based materials (e.g., wood) as fuels predates recorded history, these fossil energy sources are finite and could become scarce resources in the foreseeable future.[4-5] Given that the population of the United States currently exceeds 325 million people and is expected to surpass 400 million by the year 2050,[6] the challenge to meet the increasing demands for energy will only become more economically pressing. Additionally, the use of fossil fuels also carries significant environmental implications. The combustion of coal and other hydrocarbon-based fuel sources produces various air-pollutants such as nitrogen oxides and sulfur dioxides.[7] However, one of the greatest concerns with burning fossil fuels is the emission of greenhouse gases like carbon dioxide (CO_2) due to the implications arising from the conclusion that these emissions are the leading cause of anthropogenic climate change.[1, 8-11] Increases in the emissions of these gases have been observed since the Industrial Revolution[12-13] and the rising levels of atmospheric CO_2 have been monitored by the Mauna Loa Observatory in Hawaii since 1958
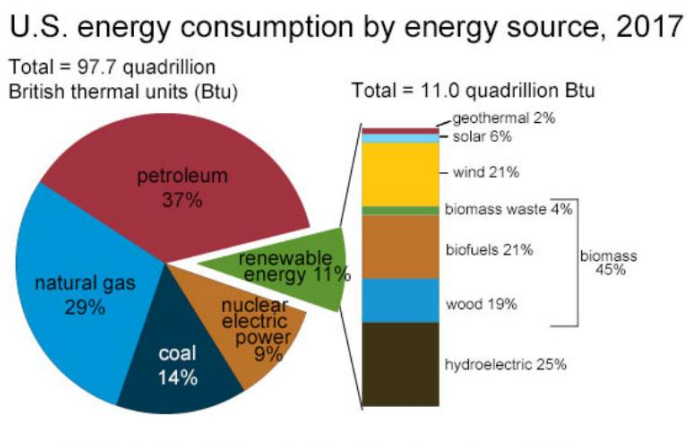
Figure 3.1. Tabulated contributions from various energy sources. Source: U.S. Energy Information Administration, *Monthly Energy Reviews*, Table 1.3 and 10.1, April 2018.

70

(**Figure 3.2**).[11-13] Given the impending depletion and rising environmental concerns surrounding fossil fuel usage, academic, government, and industrial fields have turned to exploring alternative energy strategies.

Nuclear energy represents one of the possible strategies that has the potential to support the world's growing energy needs while also remaining carbon neutral.[14-15] While coal and other hydrocarbon-based fuels generate energy via combustion, nuclear energy is generated by the fission of heavy actinide elements, predominantly uranium and plutonium.[16] The foundations of nuclear energy were first developed in the 1940s during the Second World War when fission processes were being studied for applications in nuclear weapons but were later commercialized in the 1950s for power generation. In a typical reactor, a U-235 or Pu-239 atom absorbs a neutron and then undergoes nuclear fission to split into two or more lighter nuclei, emitting gamma radiation, free neutrons, and kinetic energy.[16] From here, there are different ways in which a reactor can generate energy: 1) gamma rays produced during fission can be absorbed by the reactor and converted to heat energy or 2) the kinetic energy of the fission products can be converted into
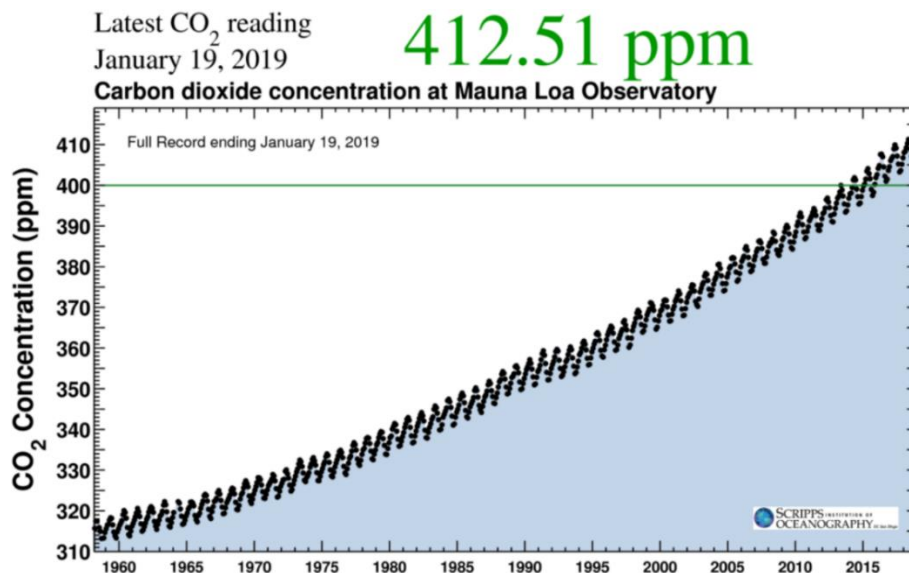
Figure 3.2. A plot of the average atmospheric CO_2 concentrations over time from 1958 to present from the Mauna Loa Observatory in Hawaii from reference 13. Credit: Scripps Institute of Oceanography.

thermal energy when the nuclei collide with surrounding atoms. The heat energy from nuclear fission can then be harnessed to convert water to steam and power mechanical turbines to produce electricity.[16-17] In comparison with other materials for energy generation, such as noble metals like ruthenium, rhodium, iridium, and rhenium, nuclear fuel sources such as uranium are much more earth-abundant, approximately 1.8 ppm in the Earth's crust.[18] Additionally, fissile uranium is also energy dense, where one kilogram can be converted to 7.2×10^{13} J of energy while, on average, one kilogram of coal produces 2.4×10^7 J of energy. Despite the significantly enhanced capability to produce energy without evolving large quantities of greenhouse gases like CO_2, nuclear power only accounts for 11% of the world's energy production due to serious political, economic, environmental, and public health-related concerns.[19-23]

Currently, there are 454 active nuclear power plants worldwide and there have been 99 documented nuclear power plant accidents of varying severity since 1952.[22] However, catastrophic incidents such as the Chernobyl, Three Mile Island, and Fukushima disasters are the forefront examples in most people's minds when the subject of nuclear power is discussed.[23] Despite the rarity of such events, public opinion of nuclear energy is often negative due to concerns related to the potentially devastating amounts of radioactive materials that can be released if a nuclear reactor were to catastrophically fail.[15] Another controversial topic related to nuclear energy is the long-term storage of radioactive waste.[24-26] Radioactive waste is generated at nearly every step of the nuclear fuel cycle and is classified into three categories: 1) low-level waste (LLW), 2) intermediate-level waste (ILW), and 3) high-level waste (HLW).[24-25, 27] LLW makes up roughly 90% of the total volume of radioactive waste produced during the nuclear fuel cycle, but accounts for only 1% of the radioactivity and requires no shielding during handling or transport. ILW requires some shielding due to higher levels of radioactivity while also producing nominal amounts

of heat (< 2 kW/m^3), but makes up only 7% of the total volume and 4% of the total radioactivity found in radioactive waste. Finally, HLW makes up just 3% of the total volume of radioactive waste but accounts for 95% of the total radioactivity. HLW is predominatly made up of the used fuel from the reactor core that contains both fission products and transuranic elements. HLW also experiences elevated temperatures (> 2 kW/m^3) due to high levels of radioactive decay and is often stored underwater in 'storage ponds' with significant shielding.[25]

Due to the long lifetimes of the radioactive components in HLW, long-term storage of these wastes is necessary (40-100 years) in order to provide ample time for the components to decay prior their final disposal. Currently, the only means to store HLW is through storage ponds or by burying the HLW in deep geological repositories such the Department of Energy's (DOE) Waste Isolation Pilot Plant (WIPP) in New Mexico.[27] The development and use of such repositories have spurred countless debates and criticisms from public and political officials due to both environmental and public health concerns. For instance, the Yucca Mountain nuclear waste repository in Nevada was intended to be a major storage facility for both spent nuclear fuel and other highly radioactive wastes in the United States.[25] However, construction of the Yucca Mountain repository was halted due to opposition from local communities around where the repository was being developed.[28] Representatives from the communities articulated concerns about the amount of potential radiation exposure to those living near the facility would incur as well as related issues regarding groundwater contamination as a result of potential leaks that could occur during the repository's tenure. These and similar arguments are pervasive in the discussions related to the large-scale commercialization of nuclear energy in the United States.[29]

In order to navigate the issues related to waste storage, government agencies like the DOE have turned to developing methods that would greatly reduce the amount of HLW generated from

nuclear plants. Reprocessing spent nuclear fuel has become an attractive option for reducing the amount of long-lived radioactive isotopes while reclaiming the unconsumed uranium and plutonium components of the original fuel. Currently, the PUREX (**P**lutonium **U**ranium **R**edox **Ex**traction) process is the predominant method for reprocessing spent nuclear fuel,[30-31] and is based on liquid-liquid extraction and ion exchange reactions that utilizes tributyl phosphate to extract leftover uranium and plutonium materials. While this method has proven effective in reclaiming unspent nuclear fuel, it is a complex and laborious process that does not alleviate many of the concerns related to reducing the generation of HLW. In the U.S., the use of the PUREX process has not been used since the end of the Cold War Era after the decommissioning of the Hanford Site in Washington; however, countries such as France and Russia both utilize procedures adapted from PUREX to reprocess their spent nuclear fuel.

To develop and improve separation strategies, agencies like the DOE and National Science Foundation (NSF) have turned to funding *f*-element research to further understand the similarities and differences between 4*f* and 5*f* elements. 'Heavy element chemistry' (HEC) has emerged as an active and diverse area of research due to the unique molecular and electronic properties that *f* elements possess, giving rise to bonding properties that are vastly different from related *d*-block transition metal complexes. From theoretical, experimental, and spectroscopic studies, it is understood that the valence 3*d*-, 4*d*-, and 5*d*-orbitals extend well into the periphery of the atom and can interact with valence ligand orbitals to form covalent chemical bonds.[32] In contrast, the 4*f* orbitals of lanthanide species behave core-like, resulting in a limited overlap with valence ligand orbitals.[33-36] Consequently, the metal-ligand bonding in lanthanide complexes is predominantly electrostatic, as discussed in the introduction section of Chapter 2. Curiously, the bonding behavior of the actinides lies in-between the behaviors seen in the transition metals and the lanthanides,

prompting much debate over the ability for these elements to utilize the near-degenerate $5f$-, $6d$-, or both sets of orbitals in chemical bond formation.[37-40] For these reasons, work in both academic and government laboratories has focused on resolving the 'f electron challenge' to better understand actinide-ligand bonding in hopes of developing new ligand frameworks to selectively and efficiently sequester actinides.[41-43]

Given the capability to immobilize lanthanide complexes on carbon surfaces demonstrated in Chapter 2, there was an interest in applying this approach for actinide complexes. Specifically, immobilizing U(VI) ions, commonly referred to as $[UO_2]^{2+}$ or the uranyl cation, was of considerable interest since this is among the most common uranium components in radioactive waste. In prior work, several methods have been explored for removal of U(VI) ions from aqueous solution, such as membrane filtration,[44] ion exchange,[45-48] adsorption,[49] and metal-organic frameworks (MOFs).[50-52] To the best of our knowledge, the surface immobilization of a well-defined molecular uranyl species has not yet been reported, opening a path towards new knowledge and opportunities. Given that uranyl complexes are redox active and possess a quasi-reversible U(IV/V) couple, an immobilized uranyl species can be probed by electrochemical methods to gain information about its properties following surface immobilization.

3.3 *Results and Discussion*

Due to their ability to stabilize a variety of oxidation states and their modular steric and electronic properties, Schiff base ligand frameworks have been used heavily in transition metal, lanthanide, and actinide coordination chemistry.[53-55] The ligand framework used to immobilize the uranyl ($[UO_2]^{2+}$) complex was inspired by the Schiff base framework used in Chapter 2 to

immobilize the lanthanide complexes. For work with $[UO_2]^{2+}$, κ^4-Schiff base ligands have been proven to be effective ligands for stabilizing the dication,[55-58] in addition to some exploratory work with low-valent U(IV) and Th(IV) species.[59-61] For this work, two homogeneous literature uranyl complexes were first synthesized and characterized by spectroscopic and electrochemical techniques to develop an understanding of the U(VI/V) redox process in organic solvents such as acetonitrile (MeCN) and dimethylformamide (DMF). Once work on the homogenous model was complete, analogous pyrene-appended uranyl complexes were synthesized and characterized by spectroscopic techniques, followed by immobilization and further analysis utilizing electrochemical methods.

3.4 *Synthesis and Electrochemistry of $[UO_2]^{2+}$ Salen Complexes*

While literature pertaining to the synthesis and characterization (^{1}H NMR, ^{13}C NMR, IR, and X-ray diffraction (XRD)) of Schiff base uranyl complexes is vast,[53, 62-68] electrochemical exploration of these complexes is often scarce. To begin developing an understanding of the electrochemical behavior of Schiff base uranyl complexes, the synthesis of the complex **1-U** (**Scheme 3.1**) was pursued in order to examine its electrochemistry. The ligand precursor **1-L** is a common transition metal ligand due to its ease of synthesis.[53-55, 69-70] **Scheme 3.1** illustrates the synthetic procedure used to obtain the **1-L** ligand as well as the **1-U** complex.[62] The ^{1}H NMR
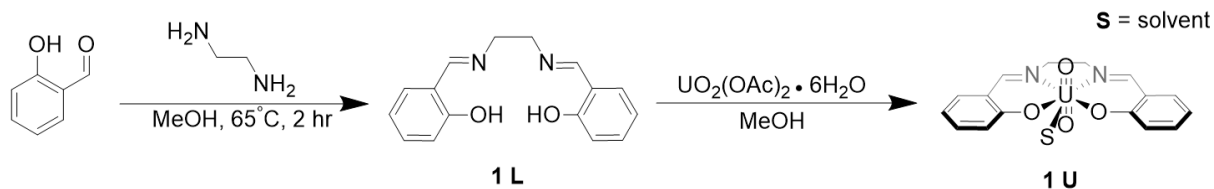
Scheme 3.1. Synthetic scheme to obtain the homogeneous $[UO_2]^{2+}$ salen complex **1-U**. Synthesis adapted from previous literature procedures in reference 62.

spectrum of the free ligand in a solution of $CDCl_3$ matches with that reported in the literature (**Appendix B**, **Figure B1**).[62, 66] The isolated **1-L** was then metallated with a stoichiometric amount of uranyl acetate hexahydrate ($UO_2(OAc)_2 \bullet 6H_2O$), which resulted in the formation of the red precipitate, **1-U**.[62, 66-67] The ^{1}H NMR spectrum of the **1-U** (**Appendix B**, **Figure B2**) shows the absence of the –OH proton resonance at 13.1 ppm from the free ligand, indicating that deprotonation has occurred. Additionally, there is a large shift downfield for the proton corresponding to the imine functionality from 8.4 ppm in the free ligand to 9.5 ppm in the **1-U** complex. Finally, the peaks at 8.0, 2.8, and 2.4 ppm correspond to a DMF-coordinated uranyl species. This behavior is common in Schiff base uranyl complexes, where the uranium center prefers to coordinate five ligands in its equatorial plane, often taking up a solvent molecule given the κ^4 nature of most Schiff base frameworks.[54, 58, 61-62, 71]

The predominant methods to characterized uranyl complexes have been by NMR, IR, and crystallography;[62] however, very little work has been done in terms of electrochemical characterization. Electrochemical work on the **1-U** complex has been done previously by the Shorkaei group, where they synthesized various solvent adducts of the **1-U** complex and compared their spectroscopic and electrochemical profiles.[67] However, reporting key components of the electrochemical experiment, such as choice of electrolyte and electrode materials, was overlooked.[67] Later work by the Mazzanti group also looked at the electrochemistry of the **1-U** complex briefly before subsequent reduction by cobaltocene to investigate the behavior of the resulting U(V) species, but did all of their electrochemical work in a pyridine-based electrolyte (E(U(VI/V)) = −1.51 V versus Fc$^{+/0}$).[65]

Cyclic voltammetry studies of the **1-U** complex were performed in a solution of 0.1 M tetrabutylammonium hexafluorophosphate in dimethylformamide. Guided by previous work from

Mazzanti and co-workers,[61, 72] the $E_{1/2}$ for the quasi-reversible U(IV/V) redox event was expected around –1.50 V versus the Fc$^{+/0}$ couple. In this work, the $E_{1/2}$ of the U(VI/V) couple for the **1-U** complex was determined to be –1.68 V versus the Fc$^{+/0}$ couple (**Figure 3.3**). Additionally, after reduction of the U(IV) complex to generate a U(V) species, a smaller current was observed in the anodic wave corresponding to the re-oxidation of the U(V) species to U(VI). This behavior is indicative of a chemical reaction
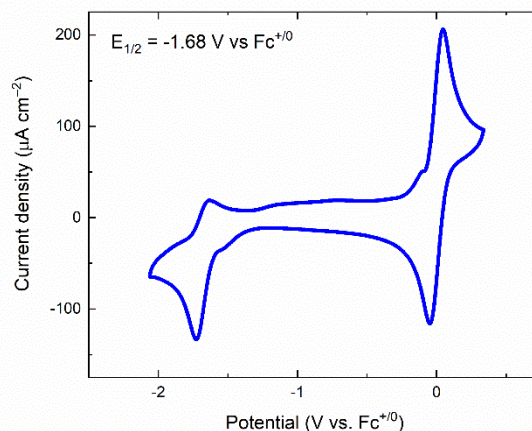
Figure 3.3. Cyclic voltammetry of the **1-U** complex in 0.1 M TBAPF$_6$ in DMF. Working: HOPG, Counter: Pt, Pseudo-reference: Pt, Scan rate: 100 mV/s. All values referenced to the standard Fc$^{+/0}$ couple shown centered at 0 V.

occurring after the reduction of the U(IV) complex to the U(V) species; however, scan rate dependence studies utilizing the Randles-Sevcik equation displayed a linear relationship between the peak current densities and the square root of scan rate (**Figure 3.4**). This relationship supports that the homogeneous system is diffusional, but exemplifies EC behavior upon reduction (EC =
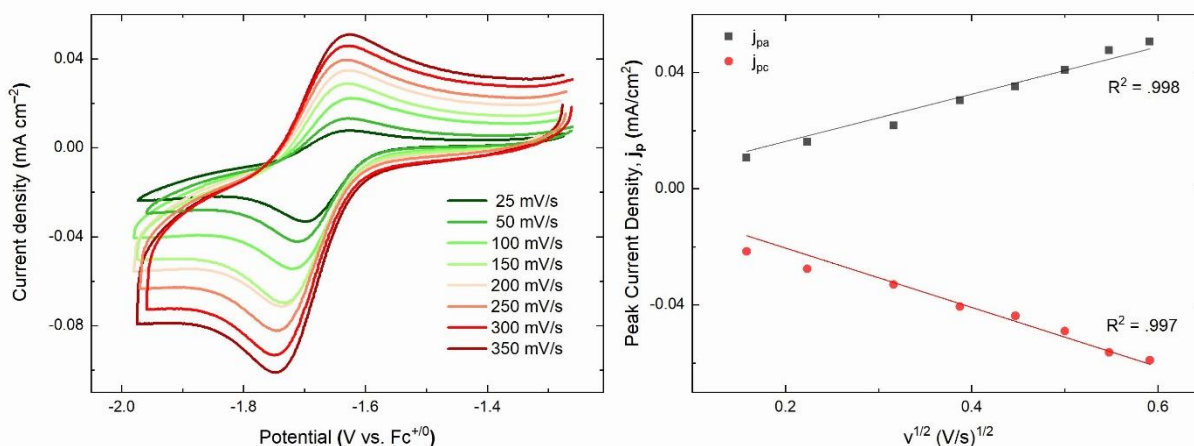
Figure 3.4. Scan rate dependence studies of the **1-U** complex in 0.1 M TBAPF$_6$ in DMF. Working electrode: HOPG, Counter: Pt, Pseudo-reference: Pt. Values for the peak current densities were background subtracted and plotted with the intercept fixed to 0 V in accordance with theory.

the oxidation/reduction of a complex by a single electron followed by a chemical reaction). **Figure 3.5** depicts the results from a single electrochemical experiment on the **1-U** complex with a total of 4 cyclic voltammetry sweeps at variable potential ranges. This experiment was used to inspect the U(VI/V) redox behavior more closely. Scan 1 of **Figure 3.5** (red) begins at –1.3 V versus Fc$^{+/0}$, scans cathodically until the switching potential of –2.2 V versus Fc$^{+/0}$ is
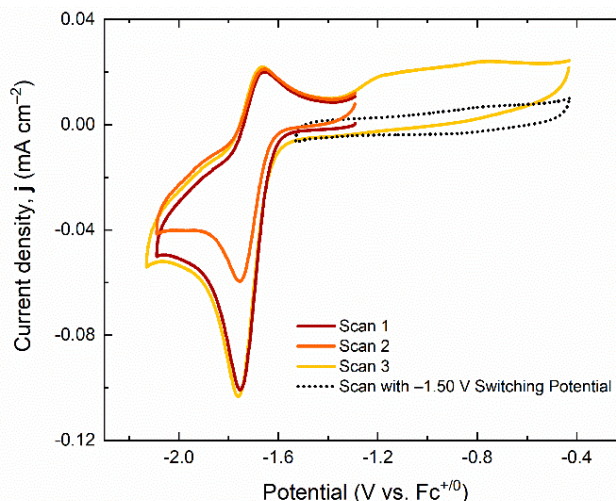
Figure 3.5. Cyclic voltammetry sweeps of the **1-U** complex at various potential windows. Electrochemical work was done in 0.1 M TBAPF$_6$ in DMF at 100 mV/s for all scans with an HOPG working electrode and platinum wires used as the counter and pseudo-reference electrodes.

reached, and then scans anodically to –1.3 V versus Fc$^{+/0}$ to begin Scan 2 (orange). Scan 2 covers the same potential range as Scan 1, scanning cathodically with a switching potential of –2.2 V versus Fc$^{+/0}$ and ending at –1.3 V versus Fc$^{+/0}$ before beginning the third scan (yellow). In Scan 3, the applied potential becomes more positive until the first switching potential of –0.4 V versus Fc$^{+/0}$ is reached. Scan 3 then sweeps cathodically until reaching the second switching potential of –2.2 V versus Fc$^{+/0}$, followed by a final anodic scan to –1.3 V versus Fc$^{+/0}$.

The data presented in **Figure 3.5** demonstrate an interesting observation that was made during the electrochemical experiment regarding the anodic (j$_{pa}$) and cathodic (j$_{pc}$) peak current densities of the **1-U** complex. Following reduction of U(VI) to U(V) in Scan 1, there is significantly less anodic current generated upon re-oxidation of U(V) to U(VI) at the end of Scan 1. By integrating the current generated for the anodic (Q$_a$) and cathodic (Q$_c$) processes in Scan 1, there was a 61% reduction in the amount of current generated during the anodic sweep following

reduction. In Scan 2, the j_{pc} was observably attenuated compared to the j_{pc} of Scan 1; however, the j_{pa} values for Scan 1 and Scan 2 were similar. These data suggest that there is a follow-up chemical reaction after the reduction of the U(VI) to U(V) that limits the amount of U(V) available for re-oxidation during the anodic sweep. This hypothesis is supported by the behavior observed in Scan 3 of **Figure 3.5**, where scanning to more oxidizing potentials results in the presence of new anodic features that contribute to a greater amount of current density that is not observed unless the potential goes through the U(VI/V) redox couple (as seen in the dotted line in **Figure 3.5**). The electrochemistry presented in **Figure 3.5** for the **1-U** complex thus suggests the presence of follow-up chemical reactions that occur following the electrochemical reduction of the U(VI) complex. The undefined follow-up reactions generate redox-active uranium species that require more oxidizing potentials to presumably regenerate the starting U(VI) species.

Behavior similar to that of the **1-U** complex has been observed previously by Ikeda and co-workers, where they examined the electrochemical behavior of a uranyl salophen complex (**Scheme 3.2**) using spectroelectrochemistry.[73] The complex studied by Ikeda and co-workers utilized phenylenediamine as the backbone of the ligand, but maintained a similar electrochemical profile to the **1-U** complex (**Figure 3.6**). Utilizing both electrochemical and spectroscopic techniques, Ikeda and co-workers proposed **Scheme 3.3** as a plausible mechanism for the observed behavior of their uranyl salophen complex. Reduction of the U(VI) species generates of U(V) species, as expected; however, the solvent ligand **L** can subsequently be lost after the reduction event. As a result of the solvent's ability to reversibly coordinate with the reduced U(V) species, the uranium metal centers
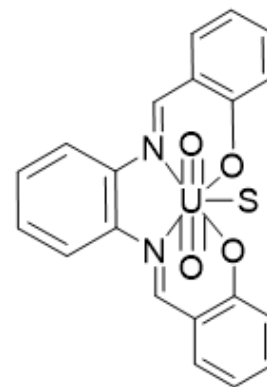
Scheme 3.2. A depiction of the uranyl salophen complex studied by spectroelectrochemistry by Ikeda and co-workers in reference 73. The solvent, S, was DMF or DMSO.

of the **U(V)** and **U(V)-L** have slightly different oxidation potentials (**Scheme 3.3**). These differences in oxidation potentials are what gives rise to the additional current observed positive of the formal U(VI/V) redox potential. Given the similar electrochemical profile, we currently assign that the **1-U** complex also follows the model proposed by Ikeda and co-workers. Further spectroscopic and electrochemical work could be used to confirm this hypothesis.

Intrigued by the electrochemical behavior of the **1-U** complex and its relative ease of synthesis, the design of a similar ligand framework that would allow for surface immobilization was pursued. Inspired by the work and ligand framework used in Chapter 2, a similar procedure was used to generate a κ^4 Schiff base ligand framework that could bind the uranyl dication while also being capable of immobilization on a carbonaceous surface. **Scheme 3.4** depicts the synthetic approach used to generate a pyrene-appended uranyl salen complex. Synthesis of compound **A** was previously discussed in Chapter 2 and served as the 'arm' component of the tripodal ligand scaffold used to immobilize the lanthanide ions.
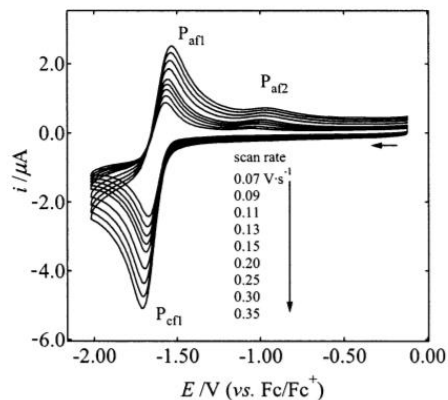
Figure 3.6. Scan rate dependent studies done by Ikeda and co-workers on the uranyl salophen complex from reference 73. Electrochemical experiments were run in 0.1 M TBAPF$_6$ in DMF utilizing Pt wires for the working and counter electrodes and a Ag$^{+/0}$ pseudo-reference electrode. All potential values were references to the Fc$^{+/0}$ couple. Reprinted with permission from Mizuoka, K.; Kim, S.-Y.; Hasegawa, M.; Hoshi, T.; Uchiyama, G.; Ikeda, Y., *Inorg. Chem.* **2003,** *42*, 1031-1038. Copyright 2003 American Chemical Society
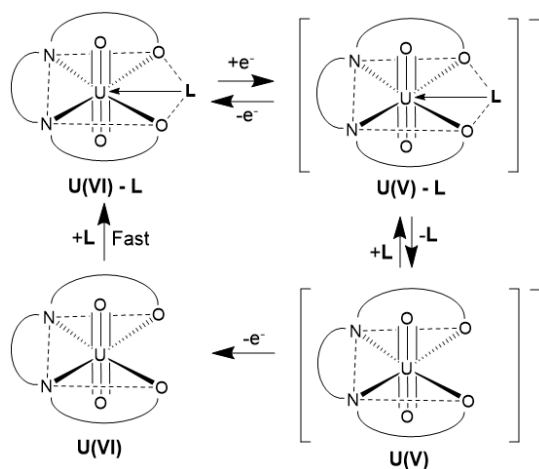
Scheme 3.3. A representation of the proposed electrochemical behavior of Ikeda and co-worker's uranyl salophen complex from reference 73.
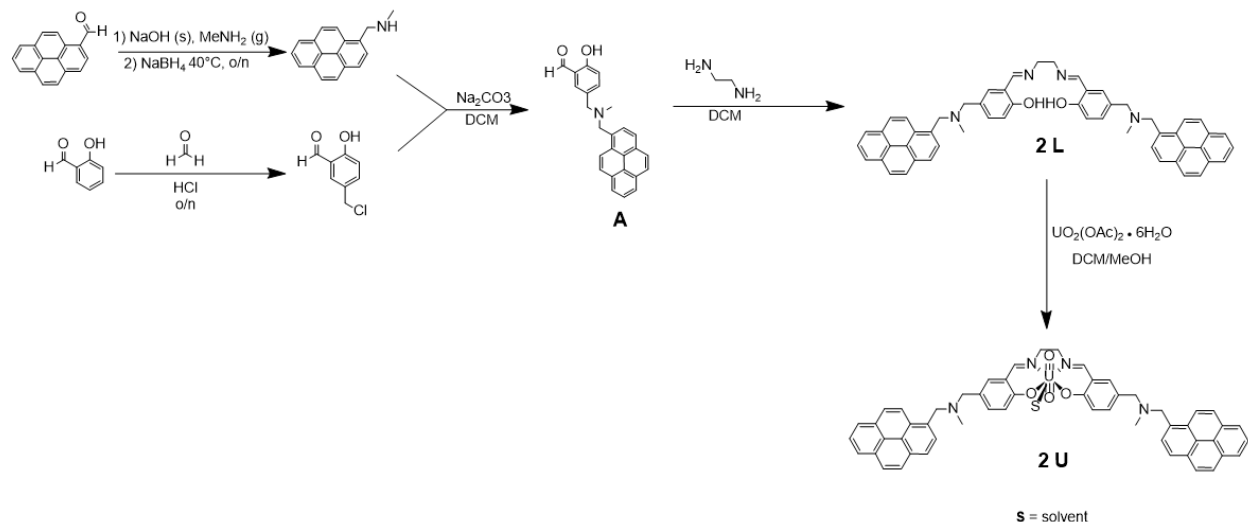
Scheme 3.4. Synthetic scheme for the synthesis of the pyrene-appended free ligand **2-L** and the pyrene-appended uranyl salen complex, **2-U**.

In order to generate the desired κ^4 Schiff base cavity, 2 equivalents of compound **A** were reacted with 1 equivalent of ethylenediamine to generate the pyrene-appended **2-L** ligand. Like the tripodal **LTP** ligand discussed in Chapter 2, the **2-L** ligand is isolated as a yellow foam in relatively good yields (ca. 87%). NMR spectroscopy was utilized in order to characterize the **2-L** free ligand prior to metalation with uranyl acetate. In **Appendix B**, **Figure B5** shows the ^{1}H NMR spectrum of the **2-L** ligand and matches with what would be expected based on the work from the tripodal complexes and has been integrated to confirm the expected stoichiometry of the ligand. Additionally, like the C_{3v} symmetry displayed by the **LTP** and **LTO** ligands from Chapter 2, the **2-L** free ligand displays only one set of peaks, indicating that the molecule is C_{2v} symmetric in solution on the NMR timescale.

Once the **2-L** free ligand was obtained, metalation with uranyl acetate hexahydrate was carried out. The **2-L** ligand was much less soluble in methanol than the **1-L** ligand, which can be attributed to the presence of the pyrene moieties. To ensure the complete solubility of the **2-L** ligand and the uranyl acetate hexahydrate, the metalation reaction was run in a mixture of methanol

and dichloromethane. After stirring overnight, a deep orange precipitate was isolated via filtration and rinsed with chilled methanol to give **2-U** in good yields (ca. 80%). The ^{1}H NMR spectrum of the **2-U** complex is shown in **Appendix B**, **Figure B7** and was recorded for the solution in d_6-DMSO. Like the ^{1}H NMR spectrum of the **1-U** complex, the ^{1}H NMR spectrum of the **2-U** complex confirms the complete and clean metalation of the **2-L** ligand. In the **2-U** spectrum, the broad peak corresponding to the phenolic proton (13.17 ppm in the **2-L** spectrum) is absent and the peak for the imine proton is shifted significantly downfield: 8.25 ppm in **2-L** to 9.5 ppm in **2-U**. As is evident by the peak intensities in the ^{1}H NMR, obtaining a reasonable concentration of the **2-U** complex in solution for characterization by NMR spectroscopy is incredibly difficult as the complex is only sparingly soluble in both organic and aqueous solvents. This behavior is quite different from the literature **1-U** complex as well as the **M(LTP)** complexes, where both could be solubilized in solvents such as dimethylformamide, dichloromethane, and dimethylsulfoxide quite readily (see Chapter 2). The solubility of the **2-U** complex is surprisingly similar to the reported behavior of the **M(LTO)** complexes,[74] where the complexes were also sparingly soluble in organic solvents. Given this, the solubility profile of the **2-U** complex might be explained as a result of the increased ability for the pyrene moieties to interact with one another due to increased proximity; however, future work and further studies related to pyrene aggregation effects are necessary to confirm this notion.

Following the synthesis and characterization of the **2-U** complex, surface immobilization onto a carbon electrode was pursued. Similar to previous work,[74-76] the drop-casted Ketjen black HOPG electrodes were utilized for the surface immobilization of the **2-U** complex. Due to solubility issues, smaller concentrations of **2-U** were used (0.25 mM solutions) in order to ensure that the compound was totally dissolved to give a homogeneous solution. Additionally, a 50:50

mixture of DMF:DCM was used as the solvent to encourage the **2-U** complex to retain a coordinated DMF molecule. Thus, the electrodes prepared with Ketjen black were submerged in the **2-U** solution overnight and subsequently rinsed with neat DCM to remove any loosely bound complex. Afterward, the electrode was placed in the

Scheme 3.5. Immobilized set-up for electrochemical work for all immobilized uranyl complexes. The diagram on the left is adapted from **Scheme 2.8** in Chapter 2 that is credited to Dr. Davide Lionetti.

custom-designed immobilized set-up from Chapter 2 (**Scheme 3.5**) for electrochemical studies.

In contrast with the single quasi-reversible U(VI/V) redox couple that had been observed in the homogeneous **1-U** complex, cyclic voltammetry of the **2-U** complex displayed two redox processes (**Figure 3.7**). The redox processes for the immobilized **2-U** complex are separated by more than 250 mV at –1.74 V and –2.00 V versus the Fc$^{+/0}$ couple. These values are significantly shifted toward greater reducing potentials, by comparison with the homogeneous **1-U** parent complex's U(VI/V) potential of –1.68 V versus Fc$^{+/0}$. These results differ from what has been previously observed for the **Ce(LTP)** and **Ce(LTO)** complexes, where immobilization lead to a shift in the E(Ce(IV/III)) to more oxidizing potentials than their homogeneous analogs. A plausible explanation for this behavior was that the tripodal ligand framework, when immobilized,

Figure 3.7. Cyclic voltammetry of the immobilized **2-U** complex in 0.1 M TBAPF$_6$ in DMF. The functionalized Ketjen black electrode served as the working electrode while 2 Pt wires were used as the counter and reference electrodes. The scan rate was 100 mV/s and all values were referenced externally to the Fc$^{+/0}$ couple.

disrupted the coordination sphere around the metal Ln^{3+} ion and pulled the hard, anionic donating ligands further from the metal center. As a result, the metal center became *less* electron-rich in that case and therefore easier to reduce. However, the electrochemical behavior of the **2-U** complex suggests that, upon immobilization, the U(VI) metal center becomes more difficult to reduce, and therefore *more* electron rich. This is likely a consequence of surface immobilization.

Although there are many questions surrounding the electrochemical properties of the **2-U** complex, further investigation of the surface immobilized complex was not carried out. There were significant issues with solubilizing the **2-U** complex in order to functionalize the Ketjen black electrodes, and there were additional issues with the surface stability and surface concentration of the **2-U** complex. Across multiple electrochemical experiments, the surface concentrations of the **2-U** were incredibly varied and most of the complex was lost from the surface within minutes,

85

making any attempts at quantitative analysis nearly impossible. Despite these drawbacks, the ability to immobilize a molecular uranyl species by noncovalent methods was achieved for the first time.

3.5 *Synthesis and Electrochemistry of Pentadentate $[UO_2]^{2+}$ Schiff base Complexes*

Although extensive quantification of the properties of the immobilized **2-U** complex was unsuccessful, the ability to achieve immobilization of a large $[UO_2]^{2+}$-containing compound was nonetheless encouraging. Given that the **1-U** and analogous complexes studied by Ikeda and co-workers displayed a dependence on the coordination of a solvent molecule,[73, 77-78] a plausible cause of the problematic electrochemistry related to the coordination chemistry of the **2-U** complex and the tendency of the compound to eject the loosely bound solvent ligand upon reduction of U(VI) to U(V). While further electrochemical analysis of the immobilized **2-U** complex was not pursued, there was an interest in pursuing the synthesis of pentadentate ligands that would satiate the coordination needs of the uranyl metal center and alleviate the involvement of solvent coordination to the uranium center. From the literature, N^1-(2-aminoethyl)ethane-1,2-diamine (diethylenetriamine for short) was determined to be the most readily accessible and inexpensive amine for generating a κ^5 Schiff base ligand framework. **Scheme 3.6** depicts the synthetic approach used by Ikeda and co-workers to generate the pentadentate ligand **3-L** and the metallated complex **3-U**.[79-80] Synthesis of the free ligand **3-L** and the metallated **3-U** complex was performed according to previously published procedures.[79] Characterization by ^{1}H NMR spectroscopy matched with
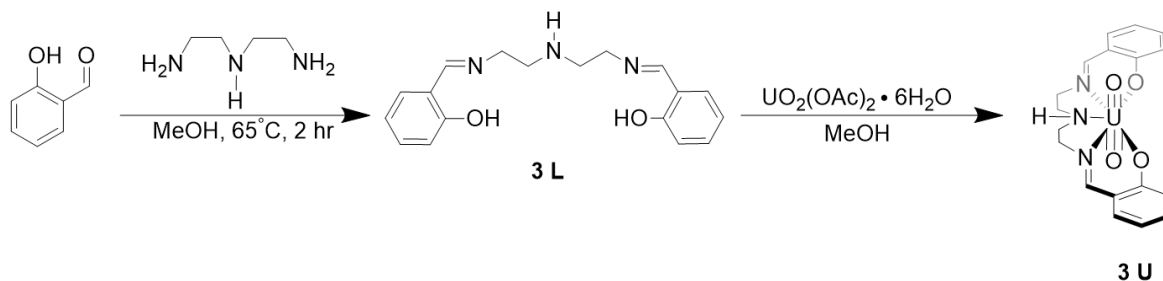
Scheme 3.6. A depiction of the route to synthesize the pentadentate Schiff base ligand **3-L** and complex **3-U**. Scheme adapted from the approach from reference 79.

previously reported values (**Appendix B**, **Figure B3** for **3-L**, and **Figure B4** for **3-U**). Original electrochemical work on the **3-U** complex was performed using 0.1 M tetrabutylammonium perchlorate (TBAP) in DMSO and showed a reversible U(VI/V) couple at -1.59 V versus $Fc^{+/0}$.[79]

Given the need to compare data for the **3-U** complex with that of the **1-U** and **2-U** complexes, electrochemical analysis of the **3-U** complex was carried out in 0.1 M $TBAPF_6$ in DMF (**Figure 3.8**). In agreement with the value expected from the literature, the U(VI/V) redox process is observed at -1.68 V versus the $Fc^{+/0}$ couple. Interestingly, the midpoint potential determined for the **3-U** complex is the same as the potential value for the **1-U** complex that was discussed previously (refer to **Figure 3.3**). However, it is not unreasonable that the **1-U** and **3-U** complexes have the same U(VI/V) redox potential given their similar coordination chemistry and their
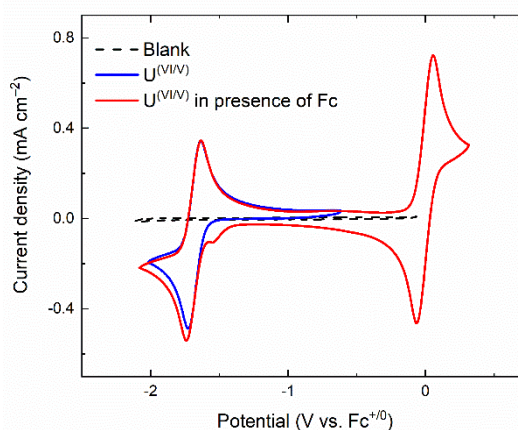
Figure 3.8. Cyclic voltammetry of the **3-U** complex in 0.1 M $TBAPF_6$ in DMF at a scan rate of 100 mV s^{-1}. The working electrode for all experiments was HOPG and Pt wires served as the reference and counter electrodes. All values were referenced to the external $Fc^{+/0}$ couple which is depicted in the red-labeled scan centered at 0 mV. The dotted line represents the current generated in the absence of the **3-U** complex and the scan in the blue was after adding the **3-U** complex to the solution.
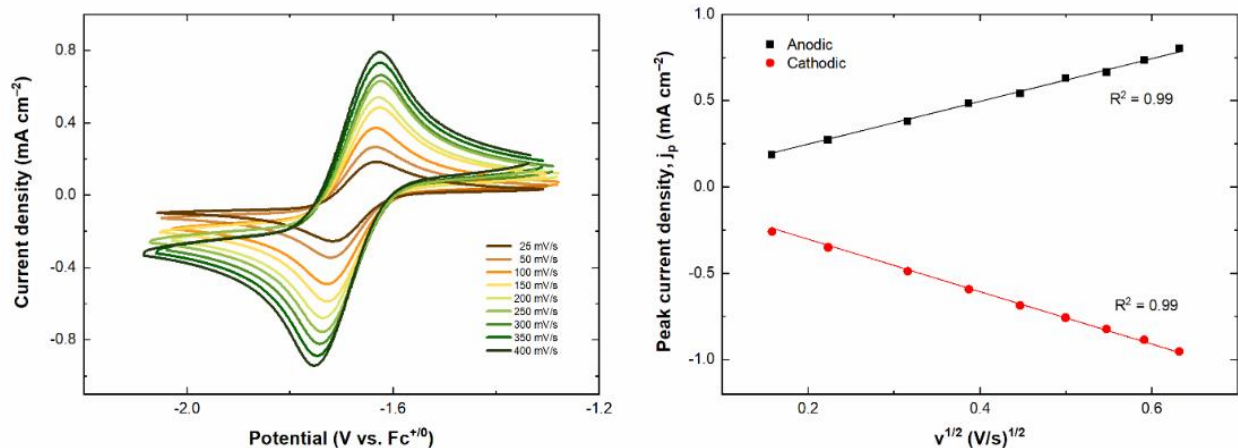
Figure 3.9. Cyclic voltammetry studies at varying scan rates for the **3-U** complex in 0.1 M TBAPF$_6$ in DMF. The working electrode used was HOPG and Pt wires were used as the counter and reference electrodes. All values were referenced to the Fc$^{+/0}$ couple. Peak current densities were background subtracted for both the cathodic and anodic processes and the line of best fit was constrained to a 0 intercept in accordance with theory.

near-identical molecular geometries.[81] One feature of the electrochemical profile of the **3-U** complex that is quite different from that of the **1-U** is the enhanced electrochemical reversibility of the U(VI/V) redox process. The peak current densities of the **1-U** complex showed a linear relationship with the square root of scan rate, in agreement with the Randles-Sevcik equation and indicated quasi-reversible, diffusional processes (**Figure 3.9**). However, there was also an observable current positive of the U(VI/V) couple for the **1-U** complex that was attributed to the presence of multiple species of reduced **1-U** complex by Ikeda and co-workers. For the **3-U** complex, additional oxidative features are not present and the anodic and cathodic currents appear to be proportional to one another (**Figure 3.10**). Scan rate dependence
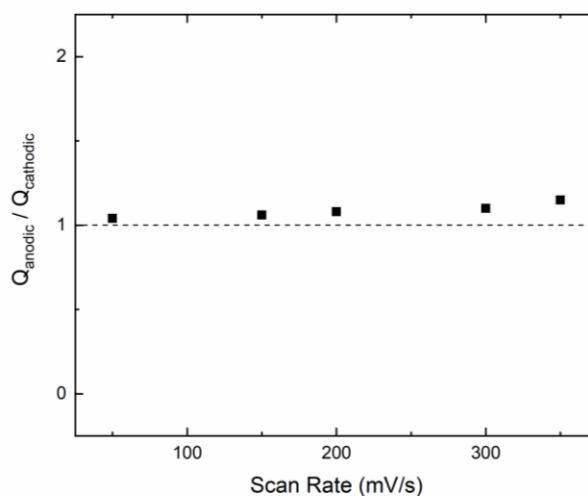
Figure 3.10. Plot of the calculated ratios of the anodic and cathodic peak areas as a function of scan rate. The expected ratio for the 1 electron U(VI/V) process that occurs in the **3-U** complex is 1:1, indicated by the horizontal dotted line.
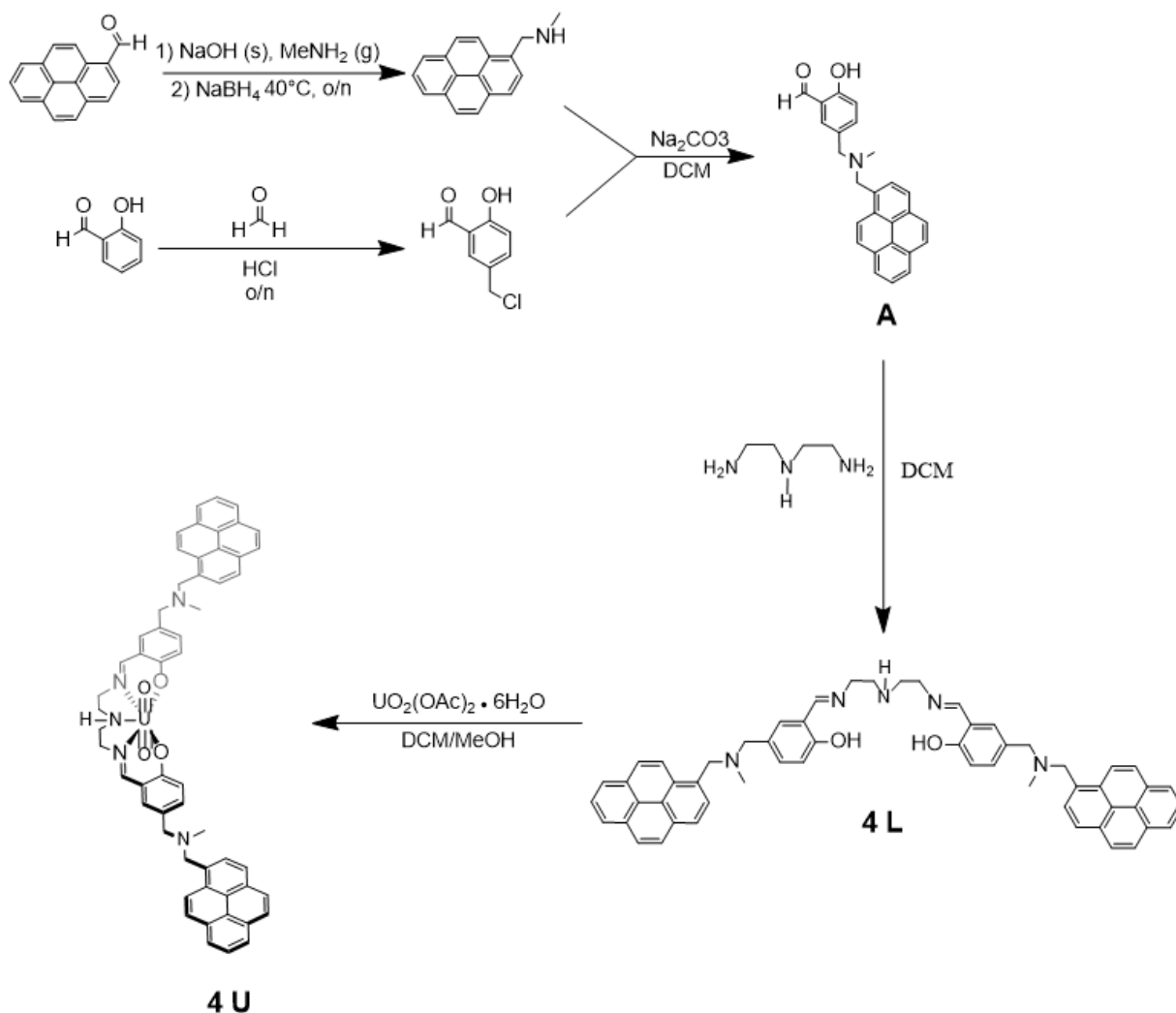
Scheme 3.7. Synthetic procedure to obtain compound **4-L** and complex **4-U**.

studies of the **3-U** complex also displayed a linear relationship between the peak current densities

of the anodic and cathodic scans and the square root of scan rate, supporting diffusional and quasi-

reversible nature of the U(VI/V) redox couple.

To further understand the surface properties of an immobilized U(VI/V) redox couple, the

synthesis of a pyrene-appended, pentadentate ligand was pursued (**Scheme 3.7**). Fortunately, as

with previous work, compound **A** could be used as a precursor to generate the pyrene-appended **4-**

L ligand framework. Compound **4-L** can be isolated in good yields (ca. 70%) as a yellow foam,

much like the other frameworks discussed in this thesis. By ^{1}H- and ^{13}C NMR spectroscopy,

compound **4-L** was fully characterized and shows only a single set of peaks, indicating that compound **4-L** displays C_{2v} symmetry in solution on the NMR timescale (**Appendix B**, **Figure B8**, and **Figure B9**). Subsequent metalation of **4-L** with uranyl acetate hexahydrate results in the formation of a yellow-orange precipitate that corresponds to complex **4-U**. Similar to the **2-U** complex, the solubility of the **4-U** complex in organic solvents was relatively poor, making isolation simple but characterization more difficult. The ^{1}H NMR spectrum of the **4-U** complex was collected in CD_2Cl_2 and is shown in **Appendix B**, **Figure B10**. Within the aliphatic region of the ^{1}H NMR spectrum, there are five peaks corresponding to the **4-U** complex. The singlet centered around 2.26 ppm and integrating to 6.44 can be readily assigned to the protons present on the tertiary amine within the 'arm' component of the ligand framework in agreement with the previous chemical shifts documented for the **M(LTP)** and **2-U** complexes (**Figure 3.11**, purple). Between 3 and 5 ppm, there are four peaks present with integrations of 2, 3, 6, and 6 corresponding to the protons on the diethylenetriamine backbone and the protons on the connecting carbons of the arm component (labeled in blue, green, and red in **Figure 3.11**). These assignments are based on the
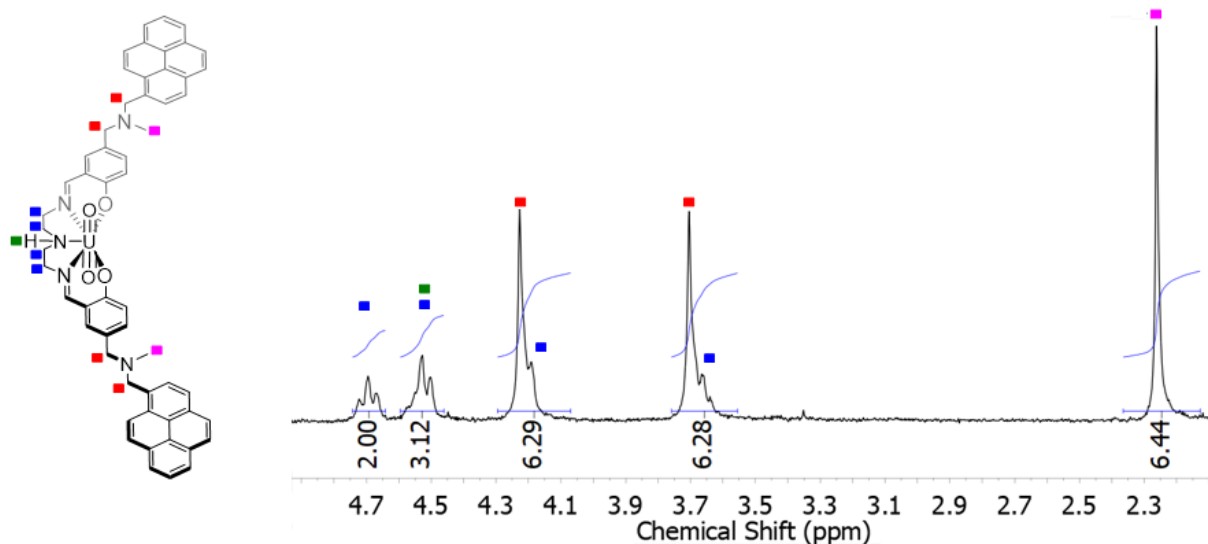
Figure 3.11. Enhanced ^{1}H NMR spectrum of the **4-U** complex's aliphatic region with color-coded preliminary assignments.

previous assignments made for the **M(LTP)**, **M(LTO)**, and **2-U** complexes in addition to the detailed crystallographic and NMR work done by Ikeda and co-workers on the homogeneous **3-U** complex.[74, 79] Currently, the assignments made in **Figure 3.11** are preliminary and would require further analysis, such as ^1H-^1H correlated spectroscopy (COSY) or ^1H-^{13}C heteronuclear single quantum coherence spectroscopy (HSQC), to confirm.

Once the **4-U** complex had been isolated and characterized by NMR, surface immobilization of the complex was pursued. Similar to the issues incurred with the **2-U** complex, the **4-U** complex was challenging to solubilize in organic solvents so lower concentrations were used to soak electrodes (0.20 mM of complex in DCM). After the electrodes were allowed to soak in the solution overnight, they were immediately placed in the immobilized electrochemical setup. A cyclic voltammogram of the **4-U** complex is shown in **Figure 3.12**. Cyclic voltammetry studies showed a quasi-reversible redox event centered at –1.59 V versus the $Fc^{+/0}$ couple that could be readily assigned to the U(VI/V) couple. Unlike the immobilized **2-U** complex, only one quasi-reversible redox event was observed, and the midpoint potential was shifted to approximately 100 mV positive (at more oxidizing potentials) of the homogeneous **3-U** complex. Additionally, the voltammetry of the **4-U** complex displays a qualitatively larger surface coverage than the **2-U** complex, as well as greater surface stability that can be readily quantized.
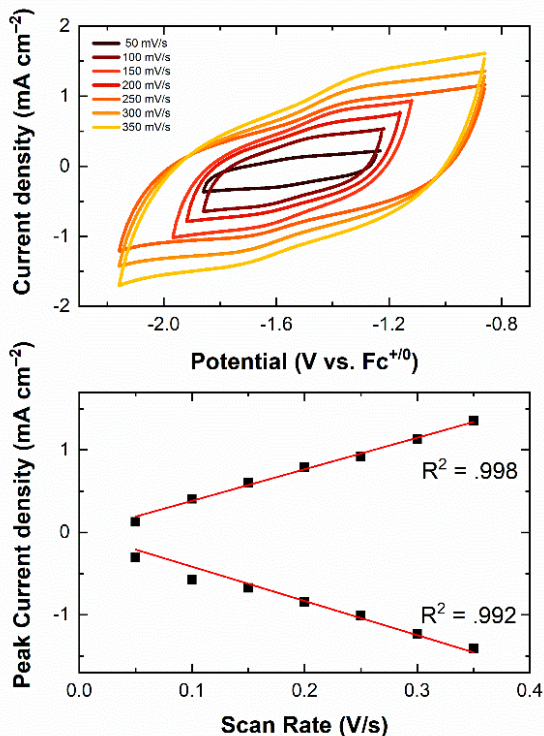

Figure 3.12. Cyclic voltammogram of the **4-U** complex in 0.1 M $TBAPF_6$ in MeCN. A functionalized Ketjen black electrode served as the working electrode with 2 Pt wires for the counter and reference electrodes. All values were referenced to the $Fc^{+/0}$ couple. The scan rate was 100 mV/s.

Scan rate dependence studies were run on the immobilized **4-U** complex in order to probe the relationship between the peak current density and the

91

scan rate. As one might recall from Chapter 2, the current generated from an immobilized redox couple should display a linear relationship with the scan rate in accordance with the equation, $i_p = \frac{n^2F^2\Gamma Av}{4RT}$.[81] **Figure 3.13** shows the voltammetry from the scan rate dependence studies for the **4-U** complex, where the peak current density of the U(VI/V) redox event is linear with the scan rate. This result demonstrates that the U(VI/V) couple has been successfully immobilized on a surface. Despite this relationship, the difference between the anodic (E_{pa}) and cathodic (E_{pc}) peak potentials (ΔE_p) for the **4-U** complex is much greater than 0 mV (ca. 400 mV). Large values for the ΔE_p were also observed for the **Ce(LTP)** and **Ce(LTO)**

Figure 3.13. Scan rate dependence of the **4-U** complex in 0.1 M TBAPF$_6$ in MeCN. A functionalized Ketjen black electrode served as the working electrode with 2 Pt wires for the counter and reference electrodes. All values were referenced to the Fc$^{+/0}$ couple and lines of the intercept for the line of best fit was constrained to 0 in accordance with theory.

complexes and are most likely due to slow interfacial electron transfer between the electrode surface and the redox-active metal center. Additionally, the integrated charge of the anodic and cathodic peak currents at various scan rates demonstrates the expected 1:1 ratio for a one-electron redox process (**Figure 3.14**). Thus the **4-U** complex displays an electrochemically quasi-reversible reduction that appears to be chemically reversible.

Given the complete electrochemical profile of the **4-U** complex, further analysis of the surface stability and electron transfer properties was pursued. Unlike the immobilized **2-U** complex, the **4-U** complex displayed greater surface stability that could be monitored with cyclic voltammetry over time. Given the data obtained for the **Ce(LTP)** and **Ce(LTO)** complexes, there was significant interest in comparing the surface and electron transfer properties across all of the complexes. In order to achieve this, the **4-U** complex was examined with time-dependent cyclic voltammetry to monitor the desorption of the **4-U** complex from the surface. Additionally, the electron transfer properties of the U(VI/V) couple were interrogated utilizing the Laviron analysis method.[82]

Figure 3.15 shows the results of the time-dependent cyclic voltammetry studies for the **4-U** complex. For these experiments, cyclic voltammograms were taken at designated time
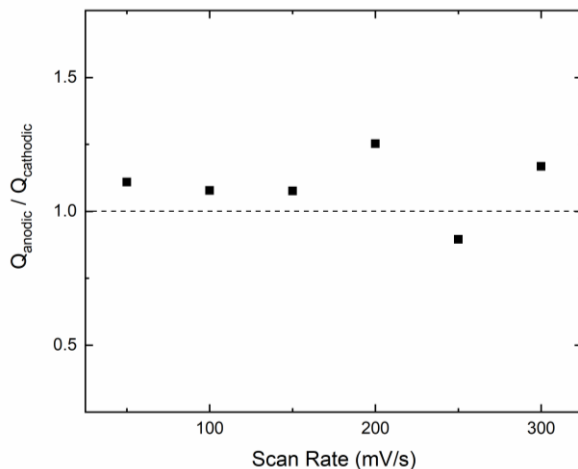
Figure 3.14. Plot of the calculated ratios of the anodic and cathodic peak areas as a function of scan rate. The expected ratio for a one-electron process that occurs in the **4-U** complex is 1:1, indicated by the horizontal dotted line.
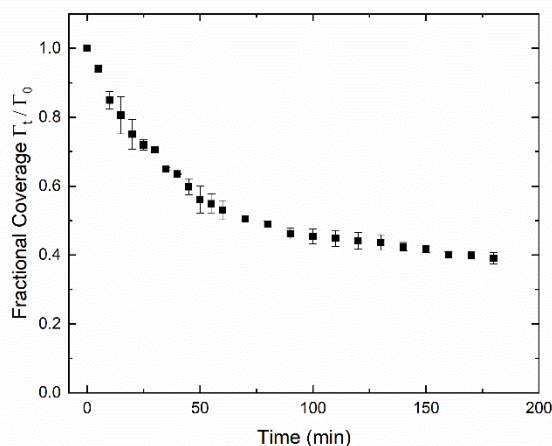
Figure 3.15. Time-dependent cyclic voltammetry study of the **4-U** complex showing gradual desorption of the complex from the surface over time. Experiments were run in triplicate and the average fractional coverage with corresponding error bars were plotted. A functionalized Ketjen black electrode served as the working electrode while 2 Pt wires were used as the counter and reference electrodes. Experiments were run in 2 mL of 0.1 M TBAPF$_6$ in MeCN at a scan rate of 100 mV/s for each scan.

intervals and the charge, Q, of the current generated from the U(VI/V) couple was integrated to calculate the surface coverage, Γ, using the equation $Q = nFA\Gamma$, where n represents the number of electrons, F is Faraday's constant, and A is the area of the electrode.[81, 83-86] Compared with the fractional coverage plots of the **Ce(LTP)** and **Ce(LTO)** complexes (**Figure 3.16**), the **4-U** complex maintains significantly greater surface coverage over long time periods. Approximately 40% of the **4-U** complex's original coverage is maintained after three hours while the **Ce(LTP)**
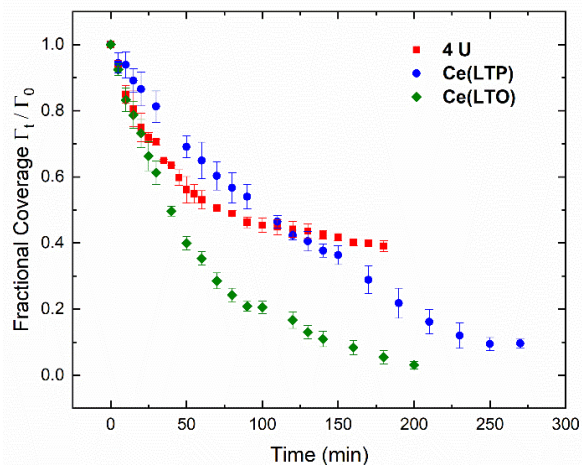
Figure 3.16. Comparison of the fractional coverage of the **4-U**, **Ce(LTP)**, and **Ce(LTO)** complexes determined from time-dependent cyclic voltammetry experiments. All experiments were performed in triplicate to determine error bars and the average fractional coverage values of the three measurements are plotted. Experiments were performed in 2 mL of 0.1 M TBAPF$_6$ in MeCN.

and **Ce(LTO)** complexes maintain only 20% and 5% of their original surface coverages, respectively. Additionally, the **4-U** complex appears to reach an equilibrium fractional coverage of approximately 40% after the first hour. This result is anomalous with what would be expected based on what has originally been reported in the literature,[85-86] where increasing the number of pyrene groups increased the surface stability of an immobilized complex. A possible explanation for this behavior could be due to the ability for the pyrene groups to interact with one another. In previous work examining the **Ce(LTO)** and **Ce(LTP)** complexes, there was evidence to suggest that the placement of the pyrene groups was influencing the overall surface stability of the complexes upon immobilization. Despite providing three pyrene groups, the tripodal ligand framework developed for the **Ce(LTO)** and **Ce(LTP)** complexes places these pyrene groups in such a way where they have the opportunity to interact with one another instead of a graphitic

surface, causing an overall loss of complex from the surface to the solution. In contrast, the bipodal framework of the **4-U** complex might allow for adequate separation of the pyrene groups from one another, resulting in a stronger interaction with a given surface. This is our working hypothesis for the observed differences in the surface stability between the tripodal and bipodal frameworks.

In future work, one technique that could serve as a useful tool to study pyrene aggregation behavior is fluorescence spectroscopy. The pyrene moiety has been employed as a molecular spectroscopic reporter to study a variety of biological and organic molecules.[87-92] When monomeric, the pyrene group displays an ensemble of fluorescence emission peaks from 375 to 405 nm. However, when two pyrene groups become spatially proximal with one another, they form an excited dimer (excimer) species that displays a red-shifted emission at 460 nm in the fluorescence emission spectrum.[93-95] Utilizing fluorescence spectroscopy, the degree of pyrene aggregation in the **M(LTP)**, **M(LTO)**, and **4-U** complexes could potentially be determined by quantifying the degree of excimer formation in the emission spectra. Future work utilizing this technique would be used to examine the potential relationship between excimer formation and the observed surface stability.

Given the enhanced surface stability exhibited by the **4-U** complex in comparison with the previously discussed **Ce(LTP)** and **Ce(LTO)** complexes, there was interest in probing the electron transfer properties of the **4-U** complex. To achieve this, Laviron analysis was utilized where the anodic and cathodic peak potentials (E_{pa} and E_{pc}) were examined as a function of scan rate.[82] As discussed in Chapter 2, Laviron analysis is a Butler-Volmer approach that utilizes overpotential (η) values to extract information related to the rate of electron transfer (k_{ET}) between the electrode surface and a redox-active complex.[82-83, 85-86] **Figure 3.17** was obtained for the **4-U** complex and displays the relationship between the peak anodic and cathodic potentials with increasing scan

rate. Similar to the profile observed for the **Ce(LTP)** and **Ce(LTO)** complexes, there is a large increase in the peak-to-peak potential separation ($\Delta E_p \gg 100$ mV) with increasing scan rate. Utilizing **Equation 3.1** and **Equation 3.2** to analyze each experimental data set (three trials in total), the average k_{ET} value for the **4-U** complex was determined to be 7.2 ± 0.5 s^{-1} (assuming $\alpha = 0.5$).

$$\textbf{Equation 3.1} \qquad E_{pc} = E^{o\prime} - \frac{2.3RT}{\alpha nF} \log \frac{\alpha nF\upsilon}{RTk_{ET}}$$

$$\textbf{Equation 3.2} \qquad E_{pa} = E^{o\prime} - \frac{2.3RT}{(1-\alpha)nF} \log \frac{(1-\alpha)nF\upsilon}{RTk_{ET}}$$

Compared to the k_{ET} values obtained for the **Ce(LTP)** and **Ce(LTO)** complexes, 2.2 ± 0.8 s^{-1} and 1.3 ± 0.4 s^{-1}, respectively, the **4-U** complex has a substantially larger k_{ET} value. These results suggest there are significant differences in the degree of interaction between the metal complexes and the electrode surface. Previous work from Dichtel and co-workers[83] observed a similar phenomenon when they compared the k_{ET} values of a tripodal and monopodal cobalt complex (**Scheme 3.8**). Utilizing Laviron analysis, they reported a k_{ET} of 13.5 s^{-1} for the tripodal cobalt complex and a k_{ET} of 18 s^{-1} for the monopodal cobalt complex. Dichtel and co-workers originally suspected that the larger k_{ET} value for the monopodal complex might be a result of lateral interaction between the complex and the surface of the electrode. Langmuir analysis[96] confirmed the adsorption of a monolayer of monopodal complex on the surface and
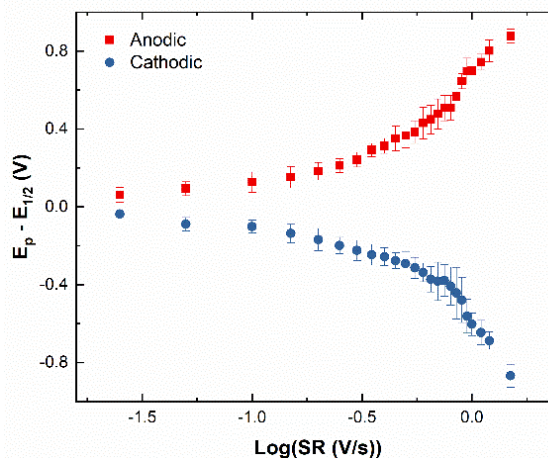
Figure 3.17. Plot of the anodic and cathodic peak currents as a function of scan rate for the **4-U** complex. Experiments were performed in triplicate to determine error bars and the average values from the three trials are plotted accordingly. All experiments were performed in 0.1 M TBAPF$_6$ in MeCN with a Ketjen black working electrode and 2 Pt wires as the counter and reference electrodes.

96

suggested no lateral interaction between the cobalt metal center and the electrode surface. Given this result, the Dichtel group suggested that this response could be attributed to the proximity of the metal center to the electrode surface, where the monopodal complex was suspected to be closer than the tripodal complex to the surface.
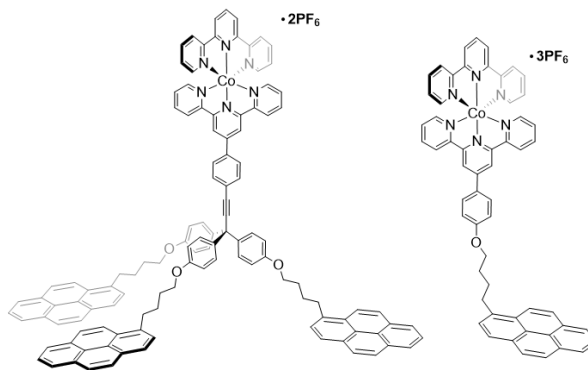
Scheme 3.8. Depiction of the Co *bis*-terpyridyl complexes studied by the Dichtel group. Scheme adapted from reference 83.

Given the large difference between the calculated k_{ET} values for the **4-U** complex and the **Ce(LTP)** and **Ce(LTO)** complexes, there could be differences in the proximity between the redox-active metal centers and the electrode surface. The differences in the ligand scaffold of the complexes could be a potential source of this behavior, where the tripodal ligand encapsulates and holds the cerium metal center further from the surface in contrast to the **4-U** bipodal ligand. Thus, the uranium metal center of the **4-U** complex can approach the surface more readily to undergo electron transfer, resulting in a larger k_{ET}. Potential techniques that could provide additional support for this hypothesis are Langmuir binding isotherm studies[83, 85-86, 96-97] that utilize electrochemistry or spectroscopy such as scanning electron microscopy (SEM),[98-101] atomic force microscopy (AFM),[70, 102-103] or spectroscopic ellipsometry (SE).[104-106] However, given the high capacitance of the Ketjen black electrode material, attempts at Langmuir studies have been ineffective due to the challenge of reliably detecting low concentrations of adsorbed electroactive species.

3.6 *Conclusion and Outlook*

In this Chapter, the successful noncovalent immobilization of uranyl Schiff base complexes utilizing pyrene has been achieved. Due to the abundance of uranyl salen complexes similar to **1-U** in the literature, the salen Schiff base framework was thought to be the most promising framework for surface immobilization.[58, 62-63, 66-67, 71-72, 107] While synthesis of the **2-U** complex was relatively simple and high-yielding, the electrochemical profile of the **2 U** complex upon immobilization was much more complicated than originally anticipated. The low current densities obtained for the U(VI/V) couple of the **2-U** complex combined with its poor surface stability made further electrochemical quantization incredibly difficult. As suggested by the work done by Ikeda and co-workers on a uranyl salophen complex, the complicated electrochemical behavior of the immobilized **2-U** complex likely stems from chemical reactions following the reduction of the U(VI) species to U(V). Future work could focus on understanding and assigning the electrochemical and chemical reaction events associated with the immobilized **2 U** complex using techniques like spectroelectrochemistry.

In order to avoid any potential issues stemming from solvent coordination to the uranium metal center, pentadentate Schiff base ligand frameworks were pursued in hopes of simplifying the electrochemistry. The homogeneous complex **3-U** initially studied by Ikeda and co-workers served as a valuable inspiration for the synthesis of the **4-U** complex. Once fully characterized by NMR, the **4-U** complex was immobilized and probed via electrochemical methods. Unlike the **2-U** complex, the **4-U** complex displayed a single, quasi-reversible U(VI/V) redox event that could be monitored and quantized utilizing electrochemistry. The stability of the **4-U** complex was substantially better than the stability of the **Ce(LTP)** and **Ce(LTO)** complexes discussed in Chapter 2. Additionally, Laviron analysis revealed a k_{ET} value of 7.2 ± 0.5 s^{-1}, which is

substantially larger than the values obtained for the cerium complexes. This suggests that surface immobilized uranyl complexes, which we have now shown to undergo relatively facile electron transfer, could be useful in future studies of uranyl capture and activation in the context of waste remediation or fuel recycling.

3.7 *References*

1.   Karl, T. R.; Trenberth, K. E., *Science* **2003,** *302*, 1719-1723.

2.   Poizot, P.; Dolhem, F., *Energy Environ. Sci.* **2011,** *4*, 2003-2019.

3.   U.S. Energy Information Administration Office of Energy Statistics. *Monthly Energy Review January 2019*; U.S. Energy Information Administration: Washington, DC. https://www.eia.gov/totalenergy/data/monthly/pdf/mer.pdf (Accessed January 29, 2019).

4.   Kerr, R. A., *Science* **1998,** *281*, 1128-1131.

5.   Cavallo, A. J., *Nat. Resour. Res.* **2004,** *13*, 211-221.

6.   Colby, S. L.; Ortman, J. M. *Projections of the Size and Composition of the U.S. Population: 2014-2060*; U.S. Census Bureau: Washington, DC. https://www.census.gov/content/dam/Census/library/publications/2015/demo/p25-1143.pdf (Accessed January 25, 2019).

7.   Khan, I., *Atmos. Environ.* **2019,** *200*, 131-141.

8.   Patz, J. A.; Campbell-Lendrum, D.; Holloway, T.; Foley, J. A., *Nature* **2005,** *438*, 310.

9.   Bonan, G. B., *Science* **2008,** *320*, 1444-1449.

10.   Hoegh-Guldberg, O.; Mumby, P. J.; Hooten, A. J.; Steneck, R. S.; Greenfield, P.; Gomez, E.; Harvell, C. D.; Sale, P. F.; Edwards, A. J.; Caldeira, K.; Knowlton, N.; Eakin, C. M.; Iglesias-Prieto, R.; Muthiga, N.; Bradbury, R. H.; Dubi, A.; Hatziolos, M. E., *Science* **2007,** *318*, 1737-1742.

11.   Cox, P. M.; Betts, R. A.; Jones, C. D.; Spall, S. A.; Totterdell, I. J., *Nature* **2000,** *408*, 184.

12.   Keeling, C. D.; Whorf, T. P.; Wahlen, M.; van der Plichtt, J., *Nature* **1995,** *375*, 666-670.

13.   Keeling, C. D.; Piper, S. C.; Bacastow, R. B.; Wahlen, M.; Whorf, T. P.; Heimann, M.; Meijer, H. A., *Exchanges of atmospheric CO_2 and $^{13}CO_2$ with the terrestrial biosphere and*

oceans from 1978 to 2000. I. Global aspects, SIO Reference Series, No. 01-06, Scripps Institution of Oceanography, San Diego, 88 pages, 2001.

14.   van Renssen, S., *Nat. Clim. Change* **2013,** *3*, 779.

15.   Kleiner, K., *Nat. Clim. Change* **2008**, 130.

16.   Nuclear Energy Institute. How a Nuclear Reactor Works. https://www.nei.org/fundamentals/how-a-nuclear-reactor-works (Accessed January 21, 2019).

17.   World Nuclear Association. How a Nuclear Reactor Makes Electricity. http://www.world-nuclear.org/nuclear-basics/how-does-a-nuclear-reactor-make-electricity.aspx (Accessed January 21, 2019).

18.   World Nuclear Association. Energy for the World - Why Uranium? http://www.world-nuclear.org/information-library/nuclear-fuel-cycle/introduction/energy-for-the-world-why-uranium.aspx (Accessed January 18, 2019).

19.   Dickson, D., *Nature* **1981,** *290*, 727.

20.   Sovacool, B. K., *Energy Policy* **2008,** *36*, 2950-2963.

21.   *Nat. Energy* **2016,** *1*, 16049.

22.   *Nature* **2006,** *440*, 969.

23.   Giles, J., *Nature* **2006,** *440*, 984.

24.   Commission, United States Nuclear Regulatory Commission. High-Level Waste. https://www.nrc.gov/waste/high-level-waste.html (Accessed January 23, 2019).

25.   World Nuclear Association. Radioactive Waste Management. http://www.world-nuclear.org/information-library/nuclear-fuel-cycle/nuclear-wastes/radioactive-waste-management.aspx (Accessed January 22, 2019).

26.   Tollefson, J., *Nature* **2014,** *507*, 15-16.

27.   United States Department of Energy. Waste Panels & Capacity. https://wipp.energy.gov/waste-panels-and-capacity.asp (Accessed January 23, 2019).

28.   Roush, W., *Science* **1995,** *270*, 1761-1762.

29.   Kerr, R. A., *Science* **2000,** *288*, 602-602.

30.   Seaborg, G. T.; Blaedel, W. J.; Walling, M. T. J. Method for Separation of Plutonium from Uranium and Fission Products by Solvent Extraction. US 2950166 United States DTIE English, 1960.

31.   Paiva, A. P.; Malik, P., *J. Radioanal. Nucl. Chem.* **2004,** *261*, 485-496.

32.   Kozimor, S. A.; Yang, P.; Batista, E. R.; Boland, K. S.; Burns, C. J.; Clark, D. L.; Conradson, S. D.; Martin, R. L.; Wilkerson, M. P.; Wolfsberg, L. E., *J. Am. Chem. Soc.* **2009,** *131*, 12125-12136.

33.   Löble, M. W.; Keith, J. M.; Altman, A. B.; Stieber, S. C. E.; Batista, E. R.; Boland, K. S.; Conradson, S. D.; Clark, D. L.; Lezama Pacheco, J.; Kozimor, S. A.; Martin, R. L.; Minasian, S. G.; Olson, A. C.; Scott, B. L.; Shuh, D. K.; Tyliszczak, T.; Wilkerson, M. P.; Zehnder, R. A., *J. Am. Chem. Soc.* **2015,** *137*, 2506-2523.

34.   Neidig, M. L.; Clark, D. L.; Martin, R. L., *Coord. Chem. Rev.* **2013,** *257*, 394-406.

35.   Nielsen, L. G.; Junker, A. K. R.; Sørensen, T. J., *Dalton Trans.* **2018,** *47*, 10360-10376.

36.   Kefalidis, C. E.; Castro, L.; Perrin, L.; Rosal, I. D.; Maron, L., *Chem. Soc. Rev.* **2016,** *45*, 2516-2543.

37.   Kaltsoyannis, N., *Inorg. Chem.* **2013,** *52*, 3407-3413.

38.   Su, J.; Batista, E. R.; Boland, K. S.; Bone, S. E.; Bradley, J. A.; Cary, S. K.; Clark, D. L.; Conradson, S. D.; Ditter, A. S.; Kaltsoyannis, N.; Keith, J. M.; Kerridge, A.; Kozimor, S.

A.; Löble, M. W.; Martin, R. L.; Minasian, S. G.; Mocko, V.; La Pierre, H. S.; Seidler, G. T.; Shuh, D. K.; Wilkerson, M. P.; Wolfsberg, L. E.; Yang, P., *J. Amer. Chem. Soc.* **2018,** *140*, 17977-17984.

39.   Glueckauf, E.; McKay, H. A. C., *Nature* **1950,** *166*, 605.

40.   Matsika, S.; Zhang, Z.; Brozell, S. R.; Blaudeau, J. P.; Wang, Q.; Pitzer, R. M., *J. Phys. Chem. A* **2001,** *105*, 3825-3828.

41.   Panak, P. J.; Geist, A., *Chem. Rev.* **2013,** *113*, 1199-1236.

42.   Leoncini, A.; Huskens, J.; Verboom, W., *Chem. Soc. Rev.* **2017,** *46*, 7229-7273.

43.   Patterson, M. G.; Mulville, A. K.; Connor, E. K.; Henry, A. T.; Hudson, M. L.; Tissue, K.; Biros, S. M.; Werner, E. J., *Dalton Trans.* **2018,** *47*, 14318-14326.

44.   Beyenal, H.; Sani, R. K.; Peyton, B. M.; Dohnalkova, A. C.; Amonette, J. E.; Lewandowski, Z., *Environ. Sci. Technol.* **2004,** *38*, 2067-2074.

45.   Feng, M.-L.; Sarma, D.; Gao, Y.-J.; Qi, X.-H.; Li, W.-A.; Huang, X.-Y.; Kanatzidis, M. G., *J. Amer. Chem. Soc.* **2018,** *140*, 11133-11140.

46.   Manos, M. J.; Kanatzidis, M. G., *Chem. Sci.* **2016,** *7*, 4804-4824.

47.   Wang, W.; Chen, Z.; Zhou, H.; Zhang, Y.; Wang, X., *Environ. Sci. Nano* **2018,** *5*, 2406-2414.

48.   Behrens, E. A.; Sylvester, P.; Clearfield, A., *Environ. Sci. Technol.* **1998,** *32*, 101-107.

49.   Wang, Z.; Lee, S.-W.; Catalano, J. G.; Lezama-Pacheco, J. S.; Bargar, J. R.; Tebo, B. M.; Giammar, D. E., *Environ. Sci. Technol.* **2013,** *47*, 850-858.

50.   Yin, C.; Liu, Q.; Chen, R.; Liu, J.; Yu, J.; Song, D.; Wang, J., *Ind. Eng. Chem. Res.* **2019,** *58*, 1159-1166.

51. Li, L.; Ma, W.; Shen, S.; Huang, H.; Bai, Y.; Liu, H., *ACS Appl. Mater. Interfaces* **2016,** *8*, 31032-31041.

52. Xiong, Y.; Gao, Y.; Guo, X.; Wang, Y.; Su, X.; Sun, X., *ACS Sustainable Chem. Eng.* **2018**.

53. Cozzi, P. G., *Chem. Soc. Rev.* **2004,** *33*, 410-421.

54. Klamm, B. E.; Windorff, C. J.; Celis-Barros, C.; Marsh, M. L.; Meeker, D. S.; Albrecht-Schmitt, T. E., *Inorg. Chem.* **2018,** *57*, 15389-15398.

55. Fenton, D. E.; Vigato, P. A., *Chem. Soc. Rev.* **1988,** *17*, 69-90.

56. Borisova, N. E.; Reshetova, M. D.; Ustynyuk, Y. A., *Chem. Rev.* **2007,** *107*, 46-79.

57. Hazra, S.; Majumder, S.; Fleck, M.; Mohanta, S., *Polyhedron* **2008,** *27*, 1408-1414.

58. Bharara, M. S.; Strawbridge, K.; Vilsek, J. Z.; Bray, T. H.; Gorden, A. E. V., *Inorg. Chem.* **2007,** *46*, 8309-8315.

59. Stobbe, B. C.; Powell, D. R.; Thomson, R. K., *Dalton Trans.* **2017,** *46*, 4888-4892.

60. Salmon, L.; Thuéry, P.; Ephritikhine, M., *Dalton Trans.* **2004**, 1635-1643.

61. Camp, C.; Andrez, J.; Pécaut, J.; Mazzanti, M., *Inorg. Chem.* **2013,** *52*, 7078-7086.

62. Evans, D. J.; Junk, P. C.; Smith, M. K., *Polyhedron* **2002,** *21*, 2421-2431.

63. Bharara, M. S.; Heflin, K.; Tonks, S.; Strawbridge, K. L.; Gorden, A. E. V., *Dalton Trans.* **2008**, 2966-2973.

64. Lombardo, G. M.; Thompson, A. L.; Ballistreri, F. P.; Pappalardo, A.; Sfrazzetto, G. T.; Tomaselli, G. A.; Toscano, R. M.; Punzo, F., *Dalton Trans.* **2012,** *41*, 1951-1960.

65. Mougel, V.; Horeglad, P.; Nocton, G.; Pécaut, J.; Mazzanti, M., *Angew. Chem.* **2009,** *48*, 8477-8480.

66. Zhao, X.; Zhang, D.; Yu, R.; Chen, S.; Zhao, D., *Eur. J. Inorg. Chem.* **2018,** *2018*, 1185-1191.

67. Asadi, Z.; Shorkaei, M. R., *Spectrochimi. Acta A* **2013,** *105*, 344-351.

68. Herasymchuk, K.; Chiang, L.; Hayes, C. E.; Brown, M. L.; Ovens, J. S.; Patrick, B. O.; Leznoff, D. B.; Storr, T., *Dalton Trans.* **2016,** *45*, 12576-12586.

69. Fennie, M. W.; DiMauro, E. F.; O'Brien, E. M.; Annamalai, V.; Kozlowski, M. C., *Tetrahedron* **2005,** *61*, 6249-6265.

70. Sonkar, P. K.; Ganesan, V.; Yadav, D. K.; Gupta, R., *ChemistrySelect* **2016,** *1*, 6726-6734.

71. Bharara, M. S.; Tonks, S. A.; Gorden, A. E. V., *Chem. Commun.* **2007**, 4006-4008.

72. Faizova, R.; Scopelliti, R.; Chauvin, A.-S.; Mazzanti, M., *J. Am. Chem. Soc.* **2018,** *140*, 13554-13557.

73. Mizuoka, K.; Kim, S.-Y.; Hasegawa, M.; Hoshi, T.; Uchiyama, G.; Ikeda, Y., *Inorg. Chem.* **2003,** *42*, 1031-1038.

74. Lionetti, D.; Day, V. W.; Blakemore, J. D., *Dalton Trans.* **2017,** *46*, 11779-11789.

75. Blakemore, J. D.; Gupta, A.; Warren, J. J.; Brunschwig, B. S.; Gray, H. B., *J. Am. Chem. Soc.* **2013,** *135*, 18288-18291.

76. Yuji, K.; Seiya, T.; Kenji, K., *Chem. Lett.* **2007,** *36*, 218-219.

77. Mizuoka, K.; Tsushima, S.; Hasegawa, M.; Hoshi, T.; Ikeda, Y., *Inorg. Chem.* **2005,** *44*, 6211-6218.

78. Mizuoka, K.; Ikeda, Y., *Inorg. Chem.* **2003,** *42*, 3396-3398.

79. Takao, K.; Kato, M.; Takao, S.; Nagasawa, A.; Bernhard, G.; Hennig, C.; Ikeda, Y., *Inorg. Chem.* **2010,** *49*, 2349-2359.

80. Takao, K.; Kato, M.; Takao, S.; Nagasawa, A.; Scheinost, A. C.; Bernhard, G.; Hennig, C.; Ikeda, Y., *IOP Conference Series: Mater. Sci. Eng.* **2010,** *9*, 012030.

81. Bard, A. J.; Faulkner, L. R., *Electrochemical Methods: Fundamentals and Applications*. 2 ed.; John Wiley & Sons: New York, 2001.

82. Laviron, E., *J. Electroanal. Chem.* **1979,** *101*, 19-28.

83. Mann, J. A.; Rodríguez-López, J.; Abruña, H. D.; Dichtel, W. R., *J. Amer. Chem. Soc.* **2011,** *133*, 17614-17617.

84. Mann, J. A.; Dichtel, W. R., *J. Phys. Chem. Lett.* **2013,** *4*, 2649-2657.

85. Kohmoto, M.; Ozawa, H.; Yang, L.; Hagio, T.; Matsunaga, M.; Haga, M.-a., *Langmuir* **2016,** *32*, 4141-4152.

86. Ozawa, H.; Katori, N.; Kita, T.; Oka, S.; Haga, M.-a., *Langmuir* **2017,** *33*, 11901-11910.

87. Shiraishi, Y.; Tokitoh, Y.; Hirai, T., *Org. Lett.* **2006,** *8*, 3841-3844.

88. Yang, J.-S.; Lin, C.-S.; Hwang, C.-Y., *Org. Lett.* **2001,** *3*, 889-892.

89. Bains, G. K.; Kim, S. H.; Sorin, E. J.; Narayanaswami, V., *Biochemistry* **2012,** *51*, 6207-6219.

90. Kim, S. K.; Bok, J. H.; Bartsch, R. A.; Lee, J. Y.; Kim, J. S., *Org. Lett.* **2005,** *7*, 4839-4842.

91. Zhou, Y.; Zhu, C.-Y.; Gao, X.-S.; You, X.-Y.; Yao, C., *Org. Lett.* **2010,** *12*, 2566-2569.

92. Fernández-Lodeiro, J.; Núñez, C.; de Castro, C. S.; Bértolo, E.; Seixas de Melo, J. S.; Capelo, J. L.; Lodeiro, C., *Inorg. Chem.* **2013,** *52*, 121-129.

93. Winnik, F. M., *Chem. Rev.* **1993,** *93*, 587-614.

94. Lemmetyinen, H.; Yliperttula, M.; Mikkola, J.; Virtanen, J. A.; Kinnunen, P. K. J., *J. Phys. Chem.* **1989,** *93*, 7170-7175.

95. Sahoo, D.; Narayanaswami, V.; Kay, C. M.; Ryan, R. O., *Biochemistry* **2000,** *39*, 6594-6601.

96. Langmuir, I., *J. Am. Chem. Soc.* **1918,** *40*, 1361-1403.

97. Mann, J. A.; Dichtel, W. R., *ACS Nano* **2013,** *7*, 7193-7199.

98. Gao, C.; He, H.; Zhou, L.; Zheng, X.; Zhang, Y., *Chem. Mater.* **2009,** *21*, 360-370.

99. Fang, B.; Zhang, C.; Zhang, W.; Wang, G., *Electrochim. Acta* **2009,** *55*, 178-182.

100. Liu, J.-W.; Zhang, Q.; Chen, X.-W.; Wang, J.-H., *Chem. Eur. J.* **2011,** *17*, 4864-4870.

101. Lu, J.; Liu, S.; Ge, S.; Yan, M.; Yu, J.; Hu, X., *Biosens. Bioelectron.* **2012,** *33*, 29-35.

102. Kidoaki, S.; Matsuda, T., *Langmuir* **1999,** *15*, 7639-7646.

103. Araki, Y.; Satoh, H.; Okumura, M.; Onishi, H., *Surf. Sci.* **2017,** *665*, 32-36.

104. Oppelt, K. T.; Gasiorowski, J.; Egbe, D. A. M.; Kollender, J. P.; Himmelsbach, M.; Hassel, A. W.; Sariciftci, N. S.; Knör, G., *J. Am. Chem. Soc.* **2014,** *136*, 12721-12729.

105. Neal, B. M.; Vorushilov, A. S.; DeLaRosa, A. M.; Robinson, R. E.; Berrie, C. L.; Barybin, M. V., *Chem. Commun.* **2011,** *47*, 10803-10805.

106. Maher, T. R.; Spaeth, A. D.; Neal, B. M.; Berrie, C. L.; Thompson, W. H.; Day, V. W.; Barybin, M. V., *J. Am. Chem. Soc.* **2010,** *132*, 15924-15926.

107. Brancatelli, G.; Pappalardo, A.; Trusso Sfrazzetto, G.; Notti, A.; Geremia, S., *Inorg. Chim. Acta* **2013,** *396*, 25-29.

Chapter 4

Summary and Future Directions

4.1 *Summary*

Advancing our ability to immobilize molecular species on conducting surfaces carries significance for a multitude of fields, such as catalysis, sensor technologies, and separations science.[1-3] Chapter 1 of this thesis gave a brief overview of surface immobilization by highlighting recent advancements utilizing both covalent and noncovalent methods on carbon-based materials.[2] By combining spectroscopic and electrochemical methods to interrogate a surface immobilized species, valuable insights regarding the properties of the immobilized species and the surface can be obtained.[1, 4-6] Many of the studies discussed in Chapter 1, such as the work from the Dichtel,[7-8] Haga,[9-10] and Ozawa[9-10] groups, have served as important foundations for examining immobilized species on carbon nanomaterials using electrochemical methods. These studies, along with many others,[6, 11-16] have been crucial to the development and interpretation of the work discussed in Chapters 2 and 3.

Chapter 2 of this thesis discusses the synthesis and characterization of a new family of tripodal lanthanide complexes, **M(LTP)** (where M = Ce, Nd, Sm, Eu), capable of noncovalent surface immobilization on carbon electrodes. Prior work published by the Blakemore group reported the synthesis and characterization of a similar family of tripodal lanthanide complexes, **M(LTO)** (where M = Ce, Nd, Sm, Eu).[17] However, electrochemical work suggested the pyrene groups of the **LTO** ligand scaffold were unable to sufficiently interact with the carbon surface. This inability of the pyrene groups to establish sufficient π-π stacking interactions with the electrode surface contributed to a limited surface stability for the **M(LTO)** complexes. Based on this observation, there was an interest in probing the effects of ligand design on surface stability. While there are many studies that have measured the effects of using different numbers and types of polycyclic aromatic hydrocarbons (PCAHs),[8-10, 18-19] there are relatively few reports that have

studied the effects of ligand design and pyrene placement on the properties of an immobilized species.

The **LTP** ligand framework was designed to limit the amount of π-interactions between the three pyrene appendages in order to enhance π-π stacking with a given electrode surface. In Chapter 2, the complete synthesis and characterization by NMR is reported for the **M(LTP)** complexes. The ^{1}H NMR spectra for the free **LTP** and **M(LTP)** complexes show only one set of peaks, indicating that the free ligand and resulting metal complex have C_{3v} symmetry in solution on the NMR timescale. This behavior was also observed in the ^{1}H NMR spectra for the **M(LTO)** complexes. Further characterization of the **M(LTP)** complexes utilizing XPS probed the integrity of the molecular structure after immobilization on a Ketjen black electrode surface. The Al Kα source XPS spectra for the M 3d and M 4d regions of each **M(LTP)** complex show only one set of peaks that can be fit with the corresponding n$d_{3/2}$ and n$d_{5/2}$, as expected from theory.[20] Additionally, the N 1s region for the **LTP** and **M(LTP)** complexes can be fit with three individual peaks in a 3:3:1 ratio, in agreement with stoichiometry. The single set of signals observed in the Al Kα XPS spectra for all **M(LTP)** complexes suggests that there is no significant decomposition after immobilization. Additionally, by integrating and normalizing the areas of the M 3d and N 1s regions, an approximate 1:7 ratio was observed for all **M(LTP)** complexes, in agreement with the stoichiometry of the complexes. Given the single set of peaks in the XPS data and the 1:7 ratio obtained by integration of the M 3d and N 1s regions of the **M(LTP)** complexes, there is substantial evidence confirming that the molecular fidelity of the **M(LTP)** complexes is maintained after immobilization.

Electrochemical analysis of the **Ce(LTO)** and **Ce(LTP)** complexes is also reported in Chapter 2. Cyclic voltammetry studies of the **Ce(LTP)** complex determined the E^0 of the

Ce(IV/III) redox couple to be –0.34 V versus the Fc$^{+/0}$ couple. Scan rate dependence studies of the **Ce(LTP)** complex displayed a linear relationship between the peak current density and the scan rate, indicating that the Ce(IV/III) couple is confined to the surface. Using the Ce(IV/III) couple as a probe, time dependent cyclic voltammetry studies of the **Ce(LTO)** and **Ce(LTP)** complexes were used to examine the relative surface stabilities of the complexes. Within the first hour, 60% of the **Ce(LTO)** complex and 40% of the **Ce(LTP)** complex was lost from the surface. After three hours, all of the **Ce(LTO)** complex had been lost from the surface while the **Ce(LTP)** complex appeared to reach an equilibrium surface concentration. Given the observed differences in surface stability, Laviron analysis was used to probe for potential differences in the interaction between the redox-active cerium metal center of the **Ce(LTO)** and **Ce(LTP)** complexes and the electrode surface. By tracking the values for E_{pc} and E_{pa} at increasing scan rates, the k_{ET} values for the **Ce(LTP)** and **Ce(LTO)** complexes were found to be 2.2 ± 0.8 s^{-1} and 1.3 ± 0.4 s^{-1} respectively. Given that these k_{ET} values are within error of one another, it can be said that the metal centers of the **Ce(LTP)** and **Ce(LTO)** complexes interact similarly with the electrode surface. Given the results from the time dependent cyclic voltammetry studies and Laviron analysis, there is a significant increase in the overall surface stability for the **Ce(LTP)** complex compared to the **Ce(LTO)** complex. These differences in surface stability are assigned to the overall design of the ligand scaffold and the placement of the pyrene groups. For the **Ce(LTO)** complex, the pyrene groups are in greater proximity to one another, contributing to increased pyrene aggregation and limiting the available area available for π-π stacking with the surface. Comparatively, the pyrene groups in the **Ce(LTP)** complex are placed further apart, limiting their interactions with each other and therefore increasing the propensity for the pyrene group to interact with the carbon surface.

Given the success of the tripodal lanthanide complexes in Chapter 2, Chapter 3 of this thesis discusses the synthesis and characterization of two new $[UO_2]^{2+}$ complexes capable of noncovalent immobilization. The complexes in Chapter 3 represent, to our knowledge, the first molecular uranium-containing complexes capable of noncovalent surface immobilization. Chapter 3 reports the synthesis and NMR characterization of two bipodal κ^4 Schiff base ligand frameworks that can be metallated with uranyl acetate to generate complexes **2-U** and **4-U**. Similar to the C_{3v} behavior observed in the tripodal work, the ^{1}H NMR spectra for free ligands and resulting complexes showed one set of peaks, indicative of C_{2v} symmetry in solution. Crystallographic data obtained for the **2-U** complex also displayed C_{2v} symmetry in the solid state. Also included in Chapter 3 were the synthesis and characterization for several uranyl complexes from the literature, **1-U** and **3-U**, that served as model complexes for the relevant electrochemical work on the **2-U** and **4-U** complexes.

Electrochemical analysis of the immobilized **2-U** complex revealed two quasi-reversible redox events with E^0 values of –1.74 V and –2.0 V versus the Fc$^{+/0}$ couple. The presence of two quasi-reversible redox events for a U(VI) uranyl species was unexpected as most uranyl complexes only display one redox event for the well-known U(VI/V) couple. The presence of the two redox events and their identification will require future work utilizing more sophisticated electrochemical techniques such as spectroelectrochemistry. Despite the issues with the electrochemistry of the **2-U** complex, the electrochemistry of the immobilized **4-U** complex displayed only one quasi-reversible redox couple centered at an E^0 of –1.59 V versus the Fc$^{+/0}$ couple. This redox event can be readily assigned to the U(VI/V) couple. Scan rate dependence studies of the **4-U** complex showed a linear relationship between the peak current density and the scan rate, indicative of a surface immobilized redox couple. Time dependent cyclic voltammetry studies of the **4-U** complex

were used to determine the relative surface stability of the bipodal complex. Compared to the results obtained for the **Ce(LTP)** and **Ce(LTO)** complexes, the **4-U** complex showed a remarkable increase in the surface stability over time. The **4-U** complex retains nearly 40% of its total surface coverage and appears to maintain that surface coverage over the course of several hours. Compared to the tripodal lanthanide complexes, the bipodal **4-U** complex appears to have a greater surface stability. Laviron analysis of the **4-U** complex revealed a k_{ET} of 7.2 ± 0.5 s^{-1} which is also substantially larger than those observed for the **Ce(LTP)** and **Ce(LTO)** complexes. In the literature, a higher k_{ET} value indicates a more direct interaction between the redox active metal center and the electrode surface.[7] For this reason, the current hypothesis for the high value of k_{ET} is that the bipodal framework 'lays down' on the electrode surface, contributing to a greater interaction between the uranium metal center and the electrode surface due to closer proximity.

4.2 *Future Directions*

  Throughout this thesis, there have been several recommended techniques that could enhance the work presented in Chapters 2 and 3. One recommendation has been to use fluorescence spectroscopy in order to observe and quantify the formation of pyrene excimers in the **M(LTO)**, **M(LTP)**, **2-U**, and **4-U** complexes. The pyrene moiety has been the focus of many spectroscopic studies[21-23] and has been used as a ratiometric probe for both cation[24-26] and anion sensing.[27-28] When two pyrene groups become close enough to engage in π-π stacking with one another, there is an observed emission at 460 nm in the fluorescence emission spectrum that has been assigned to a pyrene excimer species.[22, 29-30] Fluorescence spectroscopy could be useful to supplement the work done in Chapter 2 on the **M(LTO)** and **M(LTP)** complexes. By quantifying the emission signal for the pyrene excimer species in the fluorescence emission spectrum, one could measure the degree of pyrene aggregation in the **M(LTO)** and **M(LTP)** complexes. Specifically, observing higher quantities of the pyrene excimer species would indicate that the pyrene moieties in the ligand scaffold have a greater propensity to aggregate with one another. This aggregation behavior could be a contributing factor to the overall surface stability of a noncovalently immobilized complex. An observable increase in the formation of a pyrene excimer species would be expected for the **M(LTO)** complex as opposed to the **M(LTP)** complex. This theory is based on the results obtained from the time dependent cyclic voltammetry studies in **Figure 2.17**, where the overall surface stability of the **M(LTO)** complex was much less than the observed stability of the **M(LTP)** complex. Additionally, fluorescence spectroscopy could be used to probe for differences in pyrene aggregation behavior between the tripodal **M(LTO)**/**M(LTP)** complexes and the bipodal **2-U/4-U** complexes. To our knowledge, there are currently no reports that combine fluorescence

spectroscopy and the quantification of the pyrene excimer species to understanding of surface stability for noncovalently immobilized complexes.

Other areas of interest for future work are studies in organoactinide chemistry. The early actinides (U, Th) have many features that distinguish them from both lanthanide and *d*-block elements. Due to the relatively large ionic radii and the participation of the 5*f* orbitals in bonding interactions, complexes of the early actinides generally have higher formal coordination numbers and unusual coordination geometries. Additionally, metals such as uranium can access a range of stable oxidation states, including high-valent U(V) and U(VI) and low-valent U(III) and U(IV). While Chapter 3 of this thesis has focused on U(VI) species, there is significant interest in the synthesis, characterization, and possible catalytic activity of new U(IV) species. The chemistry and reactivity of alkyl U(IV) complexes have been extensively studied since the use of cyclopentadienyl as a supporting ligand for low-valent U(IV) complexes in the 1970s.[31] Since then, low-valent uranium metal complexes have been attracting increasing interest due to their demonstrated reactivity with small molecules such as CO,[32-34] CO_2,[35-36] N_2,[37] and H_2O[38-39] under mild conditions.[40-42]

Multidentate Schiff base ligand frameworks have been used extensively as ligands for *d*-block metals due to their ability to stabilize a range of oxidation states.[43-44] However, the use of Schiff base ligands in actinide chemistry has often been limited to the complexation of U(VI) species.[45-48] Notable contributions from the Arnold,[49] Love,[49] Ephritikhine,[50-51] and Mazzanti[37, 52-55] groups have advanced the use of Schiff base ligands in U(V) and U(IV) chemistry. Despite these advancements, there are still relatively few Schiff base U(IV) complexes[56] and even fewer that have been characterized electrochemically.[37]

2 L → **5 U**

1) 2 KO^{t}bu
2) UCl$_4$

THF

- 2 HO^{t}bu
- 2 KCl
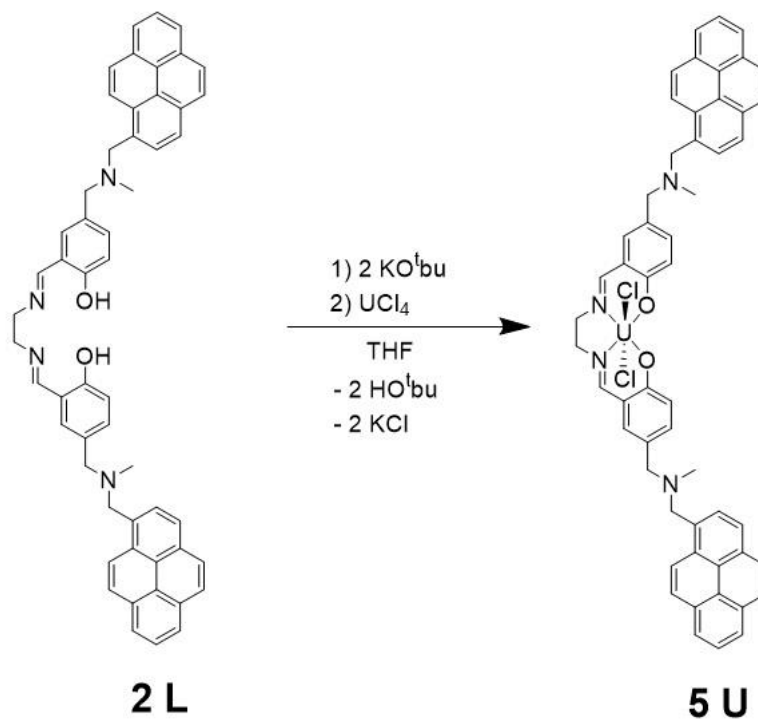
Scheme 4.1. Synthetic scheme for the **5-U** complex.

Inspired by the work from the Mazzanti[37] and the Thomson groups,[56] there was interest in using the pyrene-appended Schiff base **2-L** ligand to stabilize a U(IV) metal center. **Scheme 4.1** depicts the synthetic procedure that was used to metallate the **2-L** ligand. Unlike the procedure presented in Chapter 3 for the **2-U** and **4-U** complexes, this procedure utilized potassium tert-butoxide (KO^{t}bu) to deprotonate the **2-L** ligand before metalation. After deprotonation, a THF solution of the U(IV) precursor UCl$_4$ was added dropwise to the ligand solution. The solution was allowed to stir at room temperature overnight, followed by concentration and filtration of the solution according to previously published procedure.[56] A crude ^{1}H NMR spectrum of the suspected **5-U** complex is shown in **Figure 4.1**. While minor impurity peaks are observed in the spectrum, the major peaks in the spectrum match with expected signals for the **5-U** complex based on the previously reported spectra for U(IV) Schiff base complexes and
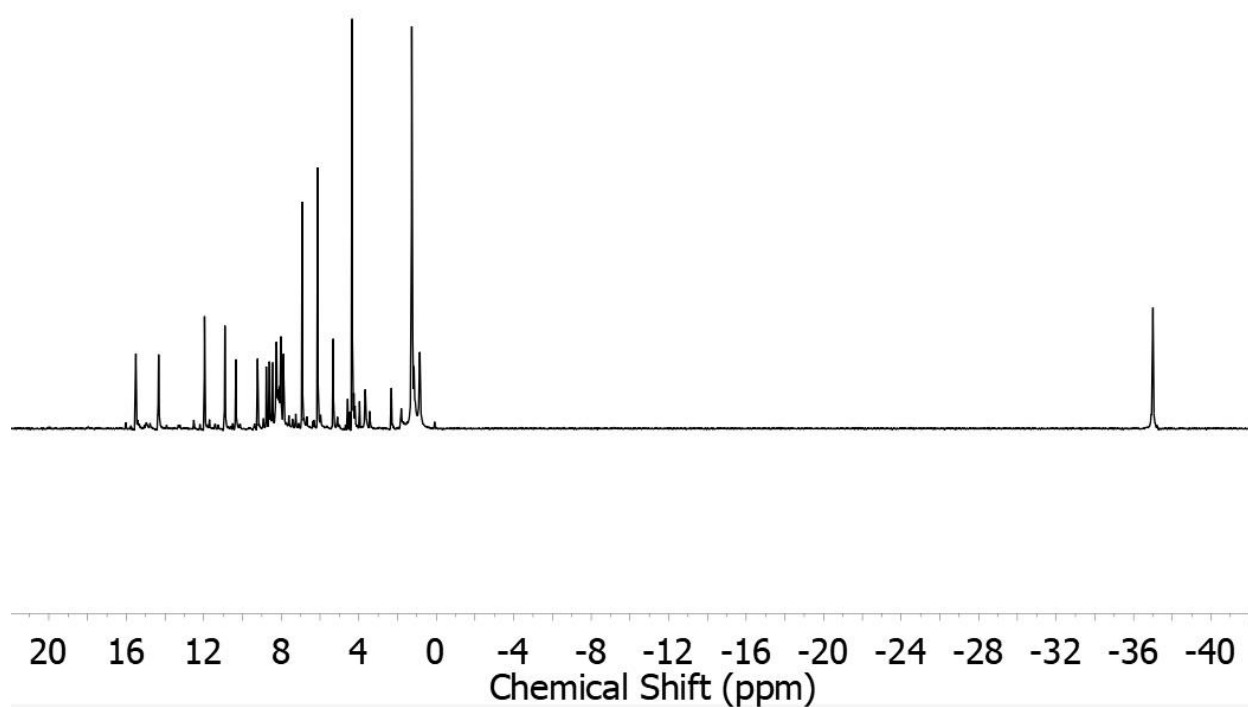
Figure 4.1. 500 MHz ^{1}H NMR spectrum of the **5-U** complex in CD$_2$Cl$_2$ at 298 K.

the findings from Chapter 3. While further purification and characterization are required to confirm the presence and integrity of the **5-U** complex, this work demonstrates that the synthesis of a pyrene appended U(IV) species for surface immobilization could be possible. This work could potentially have relevance to the immobilization of molecular U(IV) catalysts.

4.3 *References*

1. McCreery, R. L., *Chem. Rev.* **2008,** *108*, 2646-2687.

2. Bottari, G.; Herranz, M. Á.; Wibmer, L.; Volland, M.; Rodríguez-Pérez, L.; Guldi, D. M.; Hirsch, A.; Martín, N.; D'Souza, F.; Torres, T., *Chem. Soc. Rev.* **2017,** *46*, 4464-4500.

3. Axet, M. R.; Dechy-Cabaret, O.; Durand, J.; Gouygou, M.; Serp, P., *Coord. Chem. Rev.* **2016,** *308*, 236-345.

4. Bullock, R. M.; Das, A. K.; Appel, A. M., *Chem. Eur. J.* **2017,** *23*, 7626-7641.

5. Tran, D. N.; Balkus, K. J., *ACS Catal.* **2011,** *1*, 956-968.

6. Léger, C.; Bertrand, P., *Chem. Rev.* **2008,** *108*, 2379-2438.

7. Mann, J. A.; Rodríguez-López, J.; Abruña, H. D.; Dichtel, W. R., *J. Am. Chem. Soc.* **2011,** *133*, 17614-17617.

8. Mann, J. A.; Dichtel, W. R., *ACS Nano* **2013,** *7*, 7193-7199.

9. Kohmoto, M.; Ozawa, H.; Yang, L.; Hagio, T.; Matsunaga, M.; Haga, M.-a., *Langmuir* **2016,** *32*, 4141-4152.

10. Ozawa, H.; Katori, N.; Kita, T.; Oka, S.; Haga, M.-a., *Langmuir* **2017,** *33*, 11901-11910.

11. Lydon, B. R.; Germann, A.; Yang, J. Y., *Inorg. Chem. Frontiers* **2016,** *3*, 836-841.

12. McQueen, E. W.; Goldsmith, J. I., *J. Am. Chem. Soc.* **2009,** *131*, 17554-17556.

13. Reuillard, B.; Le Goff, A.; Cosnier, S., *Chem. Commun.* **2014,** *50*, 11731-11734.

14. Shou-Nian, D.; Dan, S.; Serge, C.; Alan, L. G., *Chem. Eur. J.* **2012,** *18*, 11564-11568.

15. Lei, H.; Liu, C.; Wang, Z.; Zhang, Z.; Zhang, M.; Chang, X.; Zhang, W.; Cao, R., *ACS Catal.* **2016,** *6*, 6429-6437.

16. Blakemore, J. D.; Gupta, A.; Warren, J. J.; Brunschwig, B. S.; Gray, H. B., *J. Am. Chem. Soc.* **2013,** *135*, 18288-18291.

17.   Lionetti, D.; Day, V. W.; Blakemore, J. D., *Dalton Trans.* **2017,** *46*, 11779-11789.

18.   Georgakilas, V.; Tiwari, J. N.; Kemp, K. C.; Perman, J. A.; Bourlinos, A. B.; Kim, K. S.; Zboril, R., *Chem. Rev.* **2016,** *116*, 5464-5519.

19.   Zhao, Y.-L.; Stoddart, J. F., *Acc. Chem. Res.* **2009,** *42*, 1161-1171.

20.   Orchard, A. F., *Handbook of X-ray and ultraviolet photoelectron spectroscopy*. Heyden: London, 1977.

21.   Sahoo, D.; Narayanaswami, V.; Kay, C. M.; Ryan, R. O., *Biochemistry* **2000,** *39*, 6594-6601.

22.   Lemmetyinen, H.; Yliperttula, M.; Mikkola, J.; Virtanen, J. A.; Kinnunen, P. K. J., *The J. Phys. Chem.* **1989,** *93*, 7170-7175.

23.   Duhamel, J., *Langmuir* **2012,** *28*, 6527-6538.

24.   Yang, J.-S.; Lin, C.-S.; Hwang, C.-Y., *Org. Lett.* **2001,** *3*, 889-892.

25.   Zhou, Y.; Zhu, C.-Y.; Gao, X.-S.; You, X.-Y.; Yao, C., *Org. Lett.* **2010,** *12*, 2566-2569.

26.   Kim, J. S.; Choi, M. G.; Song, K. C.; No, K. T.; Ahn, S.; Chang, S.-K., *Org. Lett.* **2007,** *9*, 1129-1132.

27.   Kim, S. K.; Bok, J. H.; Bartsch, R. A.; Lee, J. Y.; Kim, J. S., *Org. Lett.* **2005,** *7*, 4839-4842.

28.   Schazmann, B.; Alhashimy, N.; Diamond, D., *J. Am. Chem. Soc.* **2006,** *128*, 8607-8614.

29.   Bains, G. K.; Kim, S. H.; Sorin, E. J.; Narayanaswami, V., *Biochemistry* **2012,** *51*, 6207-6219.

30.   Zhang, R.; Tang, D.; Lu, P.; Yang, X.; Liao, D.; Zhang, Y.; Zhang, M.; Yu, C.; Yam, V. W. W., *Org. Lett.* **2009,** *11*, 4302-4305.

31.   Reynolds, L. T.; Wilkinson, G., *J. Inorg. Nucl. Chem.* **1956,** *2*, 246-253.

32. Summerscales, O. T.; Cloke, F. G. N.; Hitchcock, P. B.; Green, J. C.; Hazari, N., *J. Am. Chem. Soc.* **2006,** *128*, 9602-9603.

33. Summerscales, O. T.; Cloke, F. G. N.; Hitchcock, P. B.; Green, J. C.; Hazari, N., *Science* **2006,** *311*, 829-831.

34. Frey, A. S. P.; Cloke, F. G. N.; Coles, M. P.; Maron, L.; Davin, T., *Angew. Chem.* **2011,** *50*, 6881-6883.

35. Mansell, S. M.; Kaltsoyannis, N.; Arnold, P. L., *J. Am. Chem. Soc.* **2011,** *133*, 9036-9051.

36. Castro-Rodriguez, I.; Nakai, H.; Zakharov, L. N.; Rheingold, A. L.; Meyer, K., *Science* **2004,** *305*, 1757-1759.

37. Camp, C.; Andrez, J.; Pécaut, J.; Mazzanti, M., *Inorg. Chem.* **2013,** *52*, 7078-7086.

38. Halter, D. P.; Heinemann, F. W.; Maron, L.; Meyer, K., *Nat. Chem.* **2017,** *10*, 259.

39. Halter, D. P.; Heinemann, F. W.; Bachmann, J.; Meyer, K., *Nature* **2016,** *530*, 317.

40. Fox, A. R.; Bart, S. C.; Meyer, K.; Cummins, C. C., *Nature* **2008,** *455*, 341.

41. Andrea, T.; Eisen, M. S., *Chem. Soc. Rev.* **2008,** *37*, 550-567.

42. Kefalidis, C. E.; Castro, L.; Perrin, L.; Rosal, I. D.; Maron, L., *Chem. Soc. Rev.* **2016,** *45*, 2516-2543.

43. Cozzi, P. G., *Chem. Soc. Rev.* **2004,** *33*, 410-421.

44. Fennie, M. W.; DiMauro, E. F.; O'Brien, E. M.; Annamalai, V.; Kozlowski, M. C., *Tetrahedron* **2005,** *61*, 6249-6265.

45. Zhao, X.; Zhang, D.; Yu, R.; Chen, S.; Zhao, D., *Eur. J. Inorg. Chem.* **2018,** *2018*, 1185-1191.

46. Asadi, Z.; Shorkaei, M. R., *Spectrochim. Acta A* **2013,** *105*, 344-351.

47.   Brancatelli, G.; Pappalardo, A.; Trusso Sfrazzetto, G.; Notti, A.; Geremia, S., *Inorg. Chim. Acta* **2013,** *396*, 25-29.

48.   Evans, D. J.; Junk, P. C.; Smith, M. K., *Polyhedron* **2002,** *21*, 2421-2431.

49.   Bell, N. L.; Shaw, B.; Arnold, P. L.; Love, J. B., *J. Am. Chem. Soc.* **2018,** *140*, 3378-3384.

50.   Salmon, L.; Thuéry, P.; Ephritikhine, M., *Dalton Trans.* **2004**, 4139-4145.

51.   Salmon, L.; Thuéry, P.; Ephritikhine, M., *Dalton Trans.* **2004**, 1635-1643.

52.   Camp, C.; Mougel, V.; Horeglad, P.; Pécaut, J.; Mazzanti, M., *J. Am. Chem. Soc.* **2010,** *132*, 17374-17377.

53.   Horeglad, P.; Nocton, G.; Filinchuk, Y.; Pécaut, J.; Mazzanti, M., *Chem. Commun.* **2009**, 1843-1845.

54.   Mougel, V.; Horeglad, P.; Nocton, G.; Pécaut, J.; Mazzanti, M., *Angew. Chem.* **2009,** *48*, 8477-8480.

55.   Faizova, R.; Scopelliti, R.; Chauvin, A.-S.; Mazzanti, M., *J. Am. Chem. Soc.* **2018,** *140*, 13554-13557.

56.   Stobbe, B. C.; Powell, D. R.; Thomson, R. K., *Dalton Trans.* **2017,** *46*, 4888-4892.

Appendix A

Supplemental Information for Chapter 2:

Noncovalent Immobilization of Molecular Lanthanide Complexes

Appendix A

Supplemental Information for Chapter 2:
Noncovalent Immobilization of Molecular Lanthanide Complexes

Contents

A.1. *Experimental Details*

A.1.1. *General considerations*

All manipulations were carried out in dry N_2-filled gloveboxes (Vacuum Atmospheres Co., Hawthorne, CA) or under N_2 atmosphere using standard Schlenk techniques unless otherwise noted. All solvents were of commercial grade and dried over activated alumina using a PPT Glass Contour (Nashua, NH) solvent purification system prior to use, and were stored over molecular sieves. All chemicals were purchased from major commercial suppliers and used as received after drying. Deuterated NMR solvents were purchased from Cambridge Isotope Laboratories: CD_2Cl_2 was dried over CaH_2. 5-(chloromethyl)-2-hydroxybenzaldehyde, 3-(chloromethyl)-2-hydroxy-5-methylbenzaldehyde, *N*-methyl-1-(pyren-1-yl)methanamine, **1**, and **LTP** were synthesized accordingly to adapted published procedures.[1-2] Complexes $M(N(SiMe_3)_2)_3$ (M = Ce, Nd, Sm, Eu) were prepared according to the literature.[3] ^{1}H NMR spectra were collected on 400 MHz Bruker spectrometers and referenced to the residual protio-solvent signal in the case of ^{1}H. Chemical shifts (δ) are reported in units of ppm and coupling constants (J) are reported in Hz. Elemental analyses were performed by Midwest Microlab, Inc. (Indianapolis, IN).

A.1.2. *X-ray photoelectron spectroscopy (XPS)*

X-ray photoelectron spectra were collected using a Kratos AXIS Ultra system. For Al Kα source XPS, the sample chamber was kept at $< 5 \times 10^{-9}$ torr and ejected electrons were collected at an angle of 45° from the surface normal. For Mg Kα source XPS, spectra were collected using a Kratos AXIS Ultra system equipped with a nonmonochromatic Mg Kα source. The sample

chamber was kept at $< 5 \times 10^{-9}$ torr and ejected electrons were collected at an angle of 90° from the surface normal.

Survey scans were performed to identify the elements on the surface of carbon electrodes, while additional high-resolution spectra were obtained for details on specific elements. The XPS data was analysed using the program Computer Aided Surface Analysis for X-ray Photoelectron Spectroscopy (CasaXPS; from Casa Software Ltd., Teignmouth, UK). All XPS signals reported are binding energies and reported in eV. Backgrounds were fit with standard Shirley or linear backgrounds. Element peaks were fit with a standard Gaussian-Lorentzian line shape. For M $3d$ and $4d$ high-resolution spectra, major features were best fit as the respective M n$d_{5/2}$ and n$d_{3/2}$ signals with constrained peak areas of 3:2 as predicted from theory.[4] Any additional features (shake-up and shake-down peaks) were modelled as distinct individual contributions. For high-resolution spectra of the N 1s regions, the data were best fit as three distinct contributions with peak areas constrained to a 3:3:1 ratio with respect to the stoichiometry of the ligand framework. Any additional features in the N 1s region were modelled as distinct individual contributions.

A.1.3. *Electrochemistry*

Electrochemical experiments were carried out in a dry N_2-filled glovebox. Measurements were made with a Gamry Reference 600 Plus Potentiostat/Galvanostat utilizing a standard three electrode set-up using 0.10 M tetra(n-butylammonium) hexafluorophosphate (Sigma-Aldrich; electrochemical grade) as the supporting electrolyte in acetonitrile.

For homogeneous experiments, basal plane of highly oriented pyrolytic graphite (HOPG) (GraphiteStore.com, Buffalo Grove, Ill.; surface area: 0.09 cm^2) was used as the working electrode, a platinum wire (Kurt J. Lesker, Jefferson Hills, PA; 99.99%, 0.5 mm diameter) was used as the counter electrode, and a silver wire served as the pseudo-reference electrode (CH Instruments). The silver pseudo-reference was separated from the electrolyte solution by a Vycor frit (Bioanalytical Systems, Inc.). At the end of each experiment, ferrocene (Sigma Aldrich; twice-sublimed) was added to the electrolyte solution as the external reference. The experimental data was referenced to the midpoint potential for the ferrocenium/ferrocene couple (denoted as $Fc^{+/0}$).

For immobilized electrochemical measurements, all experiments were carried out in an inert atmosphere N_2-filled glovebox utilizing a custom-made Teflon cell with an O-ring seal used as the geometric area of the exposed electrode (0.28 cm^2). The platinum counter and the silver quasi-reference electrodes were immersed in the electrolyte solution. The experimental data was referenced to the midpoint potential of the ferrocenium/ferrocene couple as an external reference (denoted as $Fc^{+/0}$).

A.1.4. *Synthetic Procedures*
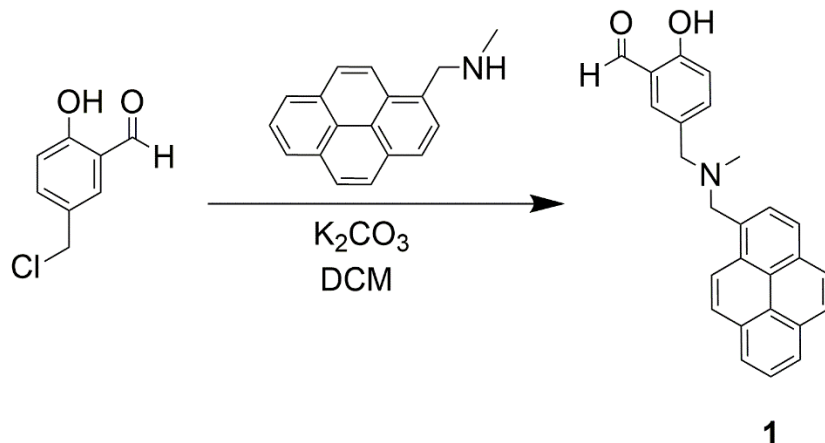
Synthesis of 1

In a 100 mL roundbottom flask, 5-(chloromethyl)-2-hydroxybenzaldehyde (1.00 g, 5.86 mmol) was added and dissolved in DCM. In a small vial, *N*-methyl-1-(pyren-1-yl)methanamine (1.51 g, 6.15 mmol) was dissolved in DCM and added to the solution of 5-(chloromethyl)-2-hydroxybenzaldehyde resulting in the formation of a colorless precipitate. K_2CO_3 was added to the flask in excess (5 equiv.). The reaction mixture was stirred at room temperature overnight. Methanol was added to the reaction flask and the resulting bright yellow solution was filtered over a medium porosity frit. Volatiles were removed *in vacuo*. DCM was then added to the flask and the resulting solution was filtered over a silica/Celite pad. The product eluted with DCM to give a yellow solution. Upon removal of volatiles, a viscous yellow oil was obtained that solidified upon standing. The product was then dried overnight at reduced pressure before proceeding to the next step. (1.98 g, 89% yield) ^{1}H NMR (400 MHz, CDCl$_3$) δ 10.92 (s, 1H), 9.83 (d, *J* = 1.9 Hz, 1H), 8.49 (dd, *J* = 9.2, 1.6 Hz, 1H), 8.26 – 7.90 (m, 8H), 7.50 (dd, *J* = 7.3, 2.4 Hz, 2H), 6.96 – 6.88 (m, 1H), 4.22 (d, *J* = 2.5 Hz, 2H), 3.58 (d, *J* = 3.1 Hz, 2H), 2.28 (d, *J* = 1.7 Hz, 3H).

1　　　　　　　　　　　　　　　　**LTP**
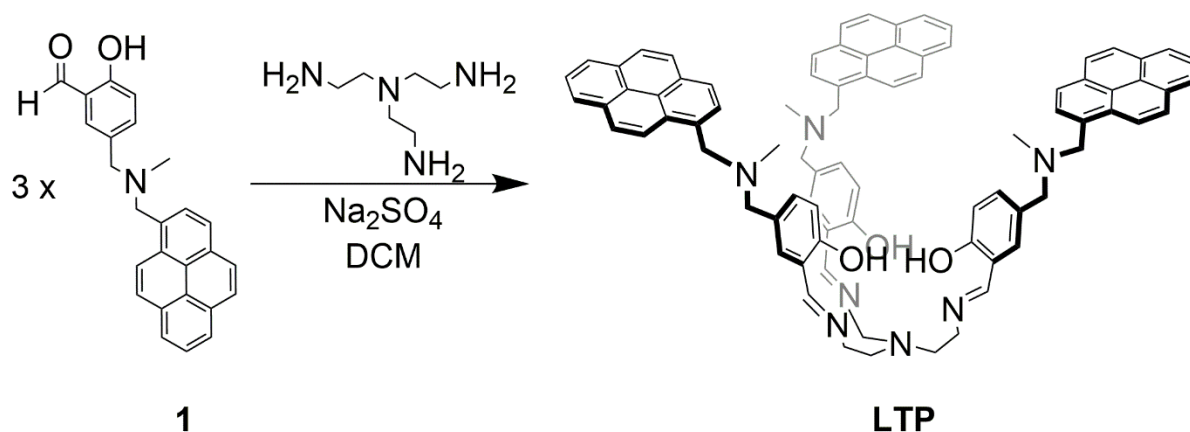
*Synthesis of **LTP***

In a 100 mL roundbottom flask, aldehyde **1** (1.001 g, 2.64 mmol) was dissolved in DCM.

Sodium sulfate (5 equiv.) was added to the flask, and tris(2-aminoethyl)amine (0.111 g, 0.765

mmol) was then added dropwise to the solution. Upon addition of the tris(2-aminoethyl)amine,

the solution's yellow color darkened. The mixture was stirred at room temperature overnight,

and the sodium sulfate removed via filtration through a Celite pad. The volatiles were removed

in vacuo to give a thick yellow oil. The yellow oil was then purified by column chromatography

by washing the excess aldehyde starting material off with DCM and then eluting the product

with a 80:20 mixture of DCM:NEt$_3$. Extensive drying at reduced pressure eventually led to

foaming of the oil to give a solid material (2.89 g, 90% yield). ^{1}H NMR (400 MHz, CDCl$_3$) δ

13.69 (s, 3H), 8.39 (d, *J* = 9.3 Hz, 3H), 8.26 – 7.71 (m, 24H), 7.13 (dd, *J* = 8.4, 2.2 Hz, 3H), 6.87

(d, *J* = 8.4 Hz, 3H), 6.51 (d, *J* = 2.2 Hz, 3H), 3.94 (s, 3H), 3.54 (t, *J* = 5.4 Hz, 6H), 3.23 (s, 3H),

2.92 – 2.74 (m, 6H), 2.05 (s, 9H).
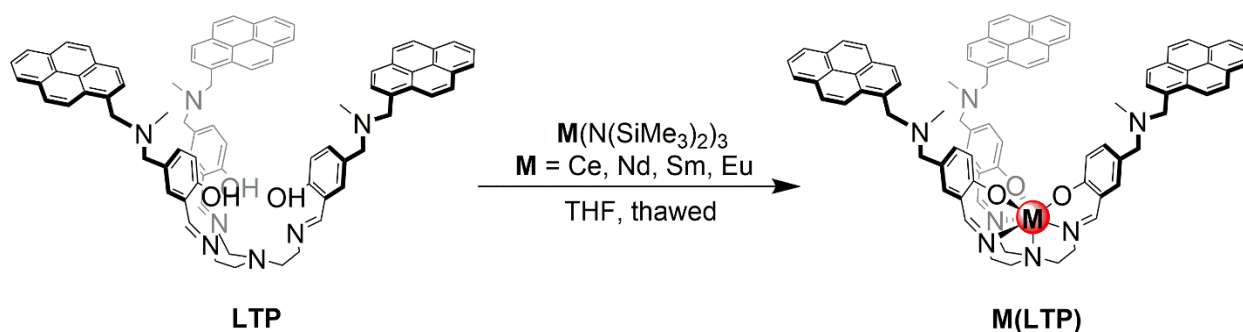
*General procedure for synthesis of **M(LTP)** complexes*

To metallate the ligand, THF solutions of **LTP** and the desired M(N(SiMe3)2)3 precursor (1:1 stoichiometry) were frozen in a LN2-refrigerated cold well. Upon thawing, the solution of the metal precursor was added dropwise to the solution of ligand. The reaction mixture was stirred at room temperature until a precipitate formed. The mixture was then filtered on a medium-porosity glass frit, and the solid washed extensively with THF or MeCN. The solid was then collected and dried *in vacuo* to remove any volatiles.

Ce(LTP)

Isolated as a light orange solid (85%). ^{1}H NMR (400 MHz, CD_2Cl_2): δ 16.7 (br s), 10.5 (br s), 9.1 (s), 8.7 – 7.7 (m), 4.8 (d, *J* = 57.6 Hz), 3.7 (s), 2.9 (s), 1.81 (s), 0.1 (s), -7.5 (br s).

Nd(LTP)

Isolated as an off-white solid (72%). ^{1}H NMR (400 MHz, CD_2Cl_2): δ 28.1 (s), 11.9 (s), 9.3 (dd, *J* = 16.0, 7.8 Hz), 8.8 – 7.8 (m), 5.1 (d, *J* = 40.4 Hz), 4.6 (s), 3.1 (s), -9.3 (s). Anal. Calcd. for $C_{84}H_{78}NdN_7O_6$ [Nd(LTP)+3H2O]: C 70.76, H 5.51, N 6.88; Found: C 70.67, H 5.38, N 6.49.

Sm(LTP)

Isolated as an off-white solid (86%). ^{1}H NMR (400 MHz, CD$_2$Cl$_2$): δ 8.7 (d, J = 9.3 Hz), 8.3 –

7.9 (m), 7.6 (s), 7.2 – 7.0 (m), 6.2 (d, J = 8.2 Hz), 4.4 (s), 3.8 (s), 2.6 – 2.2 (m), 1.3 (s), 0.05 (s), -

1.6 (s).

Eu(LTP)

Isolated as an off-white solid (83%). ^{1}H NMR (400 MHz, CD$_2$Cl$_2$): δ 21.8 (br s), 10.2 (d, J =

8.5 Hz), 8.5 – 7.0 (m), 4.0 (d, J = 7.8 Hz), 3.1 (s), 2.0 (s), 1.6 – 0.8 (m), 0.05 (d, J = 4.2 Hz), -

26.4 (s). Anal. Calcd. for C$_{84}$H$_{78}$EuN$_7$O$_6$ [Eu(LTP)+3H$_2$O]: C 70.38, H 5.48, N 6.84; Found: C

70.48, H 5.60, N 6.71.

A.2. *X Ray Photoelectron Spectroscopy (XPS)*

A.2.1 *Al-Kα Source XPS Spectra*
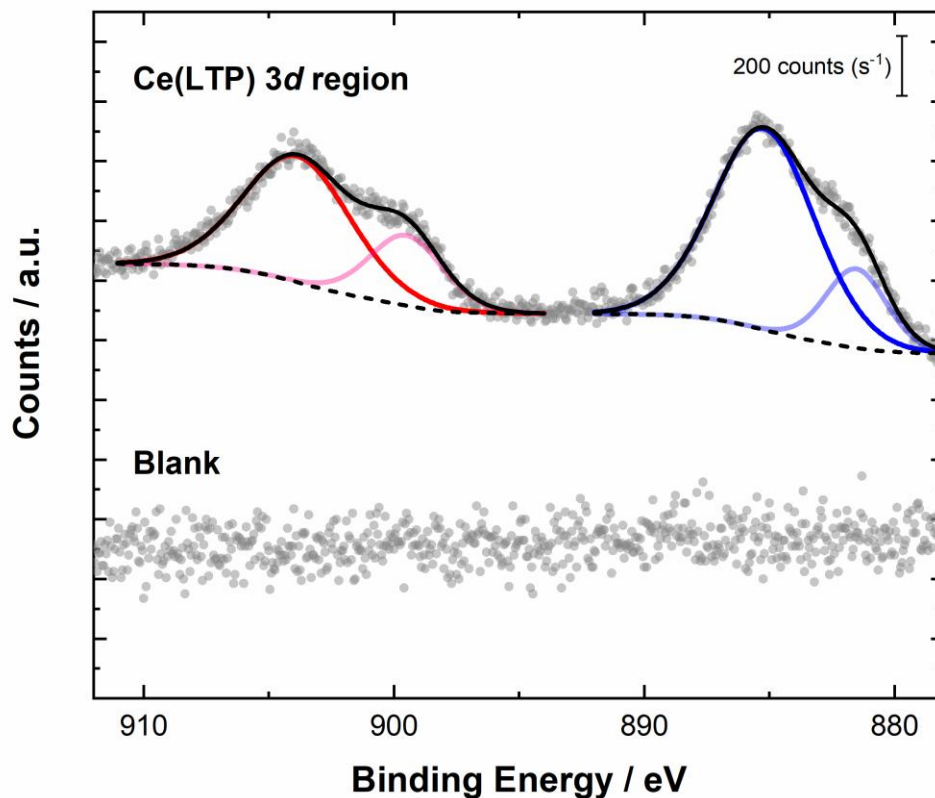
Figure A1. Spectrum of **Ce(LTP)** 3d region overlaid with a blank Ketjen black electrode for Al-source data. Legend: gray dots: data; dashed black line: fitting background; dark blue line: Ce $3d_{5/2}$ peak fit; dark red line: Ce $3d_{3/2}$ peak fit (constrained to 2/3 area with respect to Ce $3d_{5/2}$); light blue line: contribution from Ce(IV) $3d_{5/2}$; light red line: contribution from the Ce(IV) $3d_{3/2}$ (constrained to a 2/3 area with respected to Ce(IV) $3d_{5/2}$); continuous black line: overall fit.
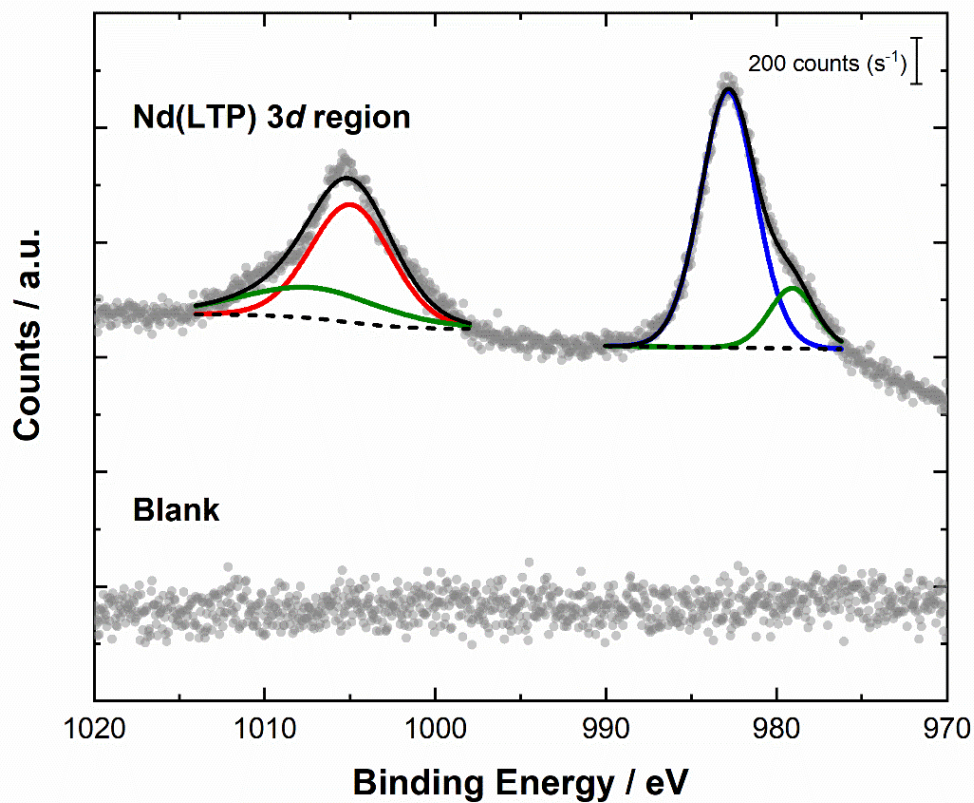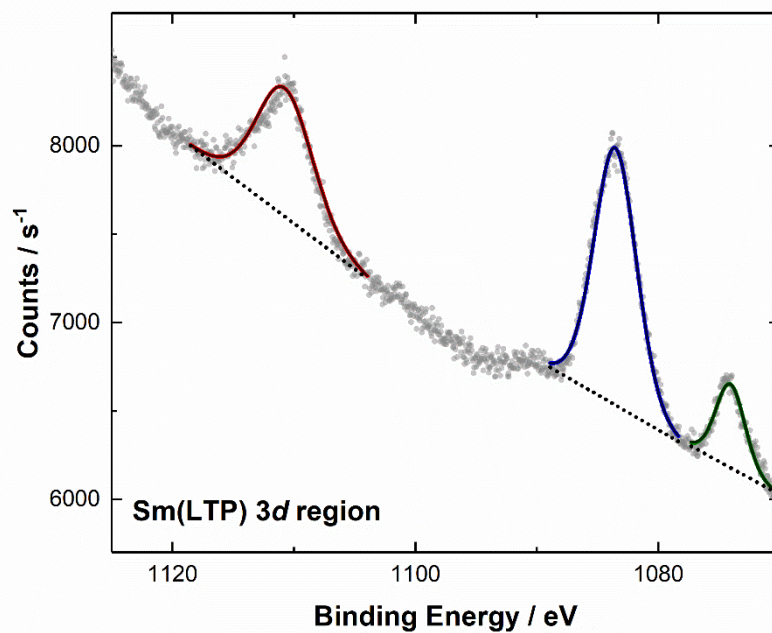
Figure A2. Spectrum of **Nd(LTP)** 3d region overlaid with a blank Ketjen black electrode from Al-source data. Legend: gray dots: data; dashed black line: fitting background; blue line: Nd $3d_{5/2}$ peak fit; red line: Nd $3d_{3/2}$ peak fit (constrained to 2/3 area with respect to Nd $3d_{5/2}$); green lines: shake-up and shake-down peaks fit; continuous black line: overall fit.
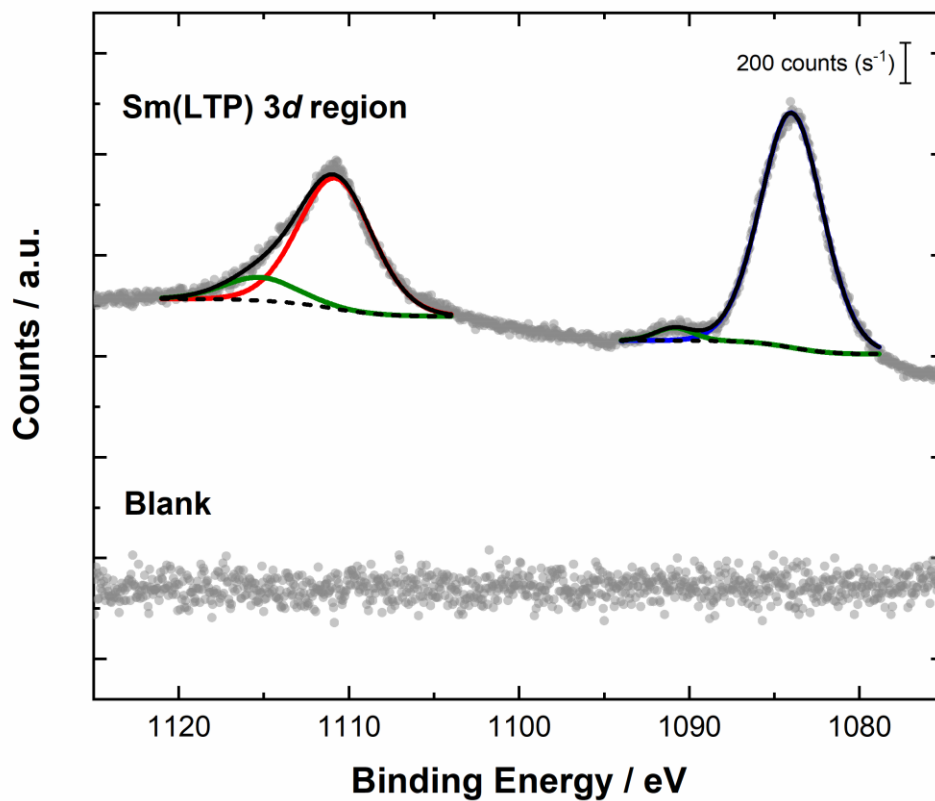
Figure A3. Spectrum of **Sm(LTP)** 3d region overlaid with a blank Ketjen black electrode from Al-source data. Legend: gray dots: data; dashed black line: fitting background; blue line: Sm $3d_{5/2}$ peak fit; red line: Sm $3d_{3/2}$ peak fit (constrained to 2/3 area with respect to Sm $3d_{5/2}$); green lines: shake-up and shake-down peaks fit; continuous black line: overall fit.
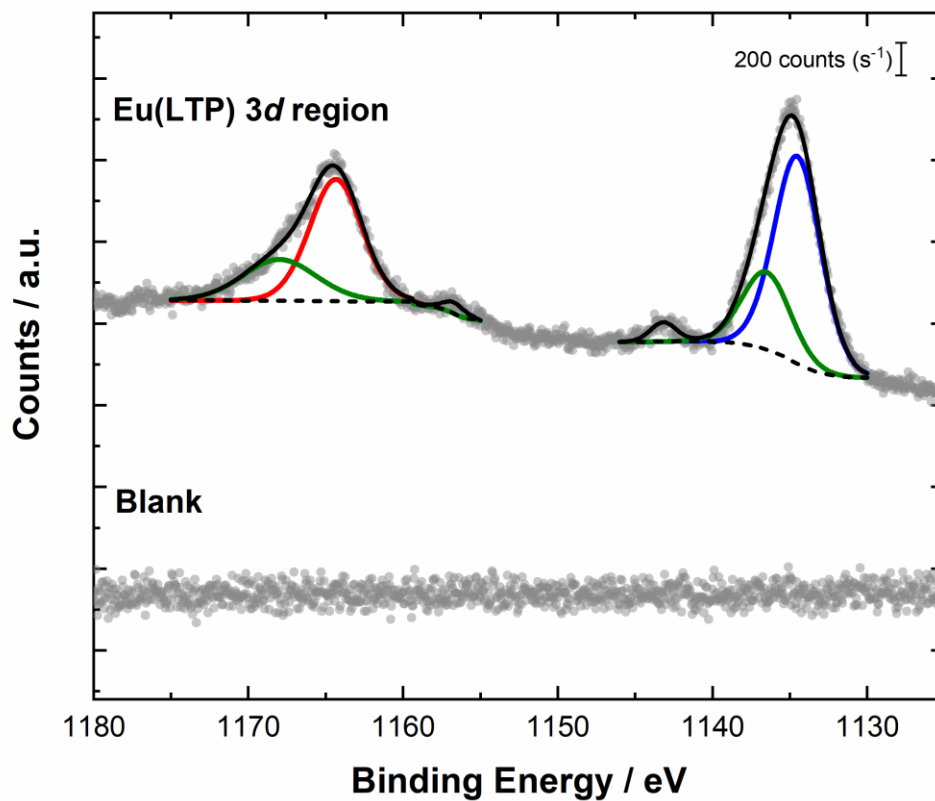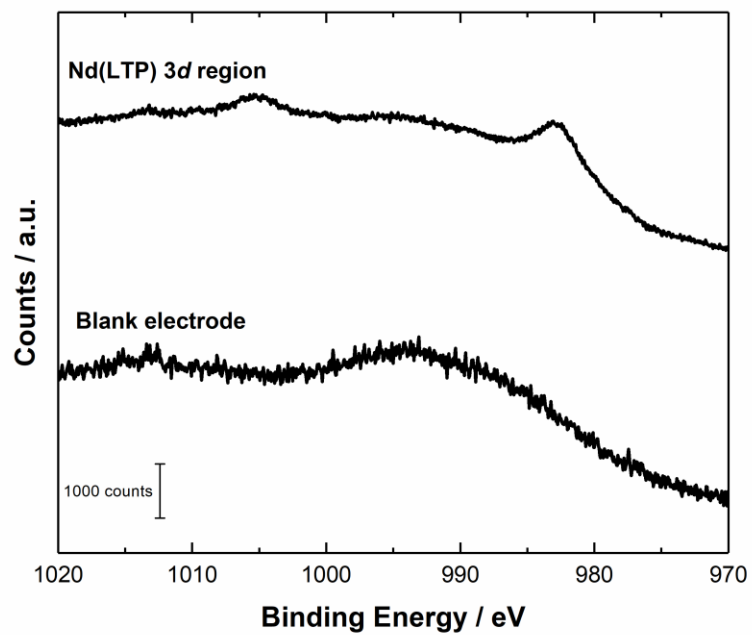
Figure A4. Spectrum of **Eu(LTP)** 3d region overlaid with a blank Ketjen black electrode from Al-source data. Legend: gray dots: data; dashed black line: fitting background; blue line: Eu $3d_{5/2}$ peak fit; red line: Eu $3d_{3/2}$ peak fit (constrained to 2/3 area with respect to Eu $3d_{5/2}$); green lines: shake-up and shake-down peaks fit; continuous black line: overall fit.
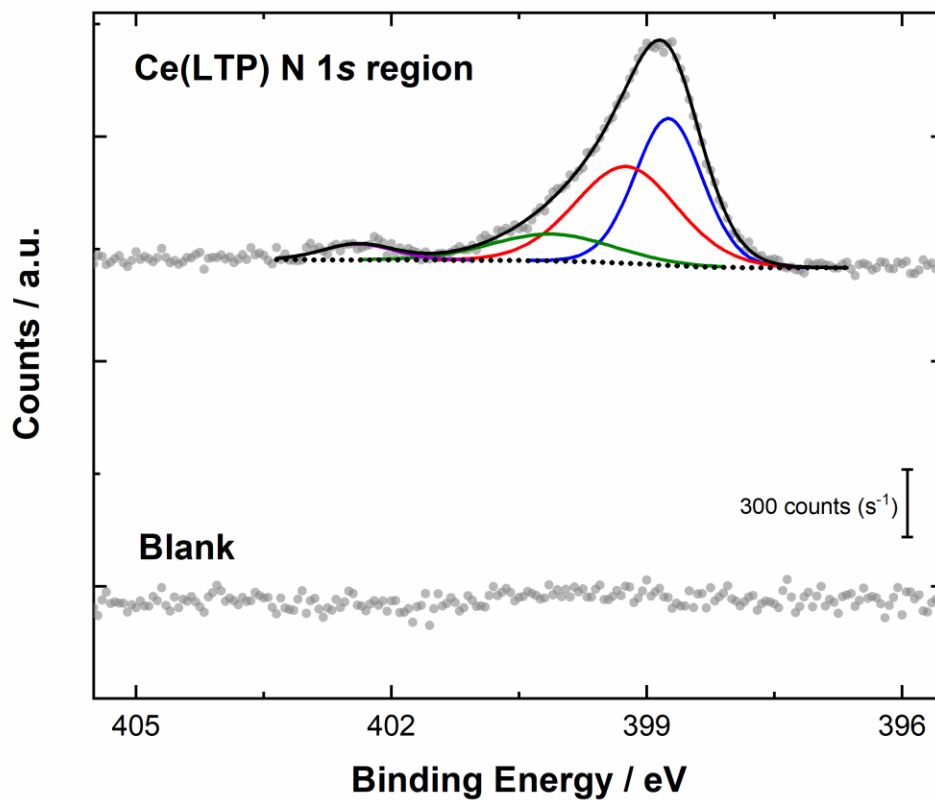
Figure A5. Spectrum of the **Ce(LTP)** N 1*s* region overlaid with a blank ketjen black electrode spectrum from Al-source data. Legend: gray dots: data; dashed black line: fitting background; blue, red, and green lines: N 1s contributions from the nitrogens of the complex (areas constrained to a 3:3:1 area, respectively); purple line: N 1s contribution from a protonated amine species; black solid line: overall fit.
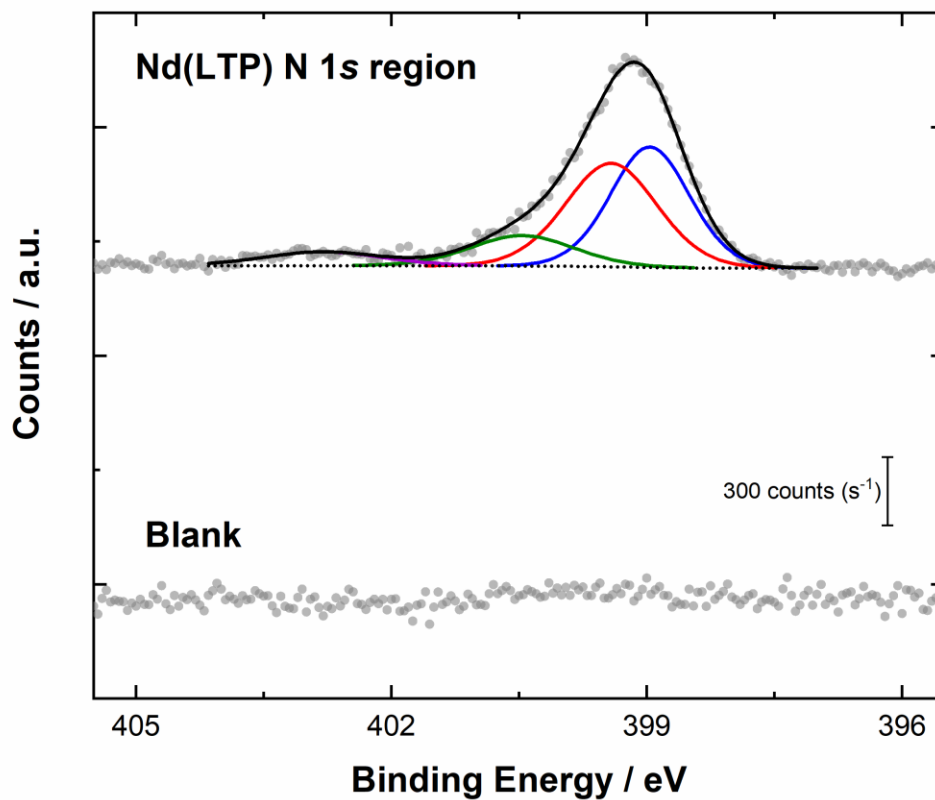
Figure A6. Spectrum of the **Nd(LTP)** N 1*s* region overlaid with a blank ketjen black electrode spectrum from Al-source data. Legend: gray dots: data; dashed black line: fitting background; blue, red, and green lines: N 1s contributions from the nitrogens of the complex (areas constrained to a 3:3:1 area, respectively); purple line: N 1s contribution from a protonated amine species; black solid line: overall fit.
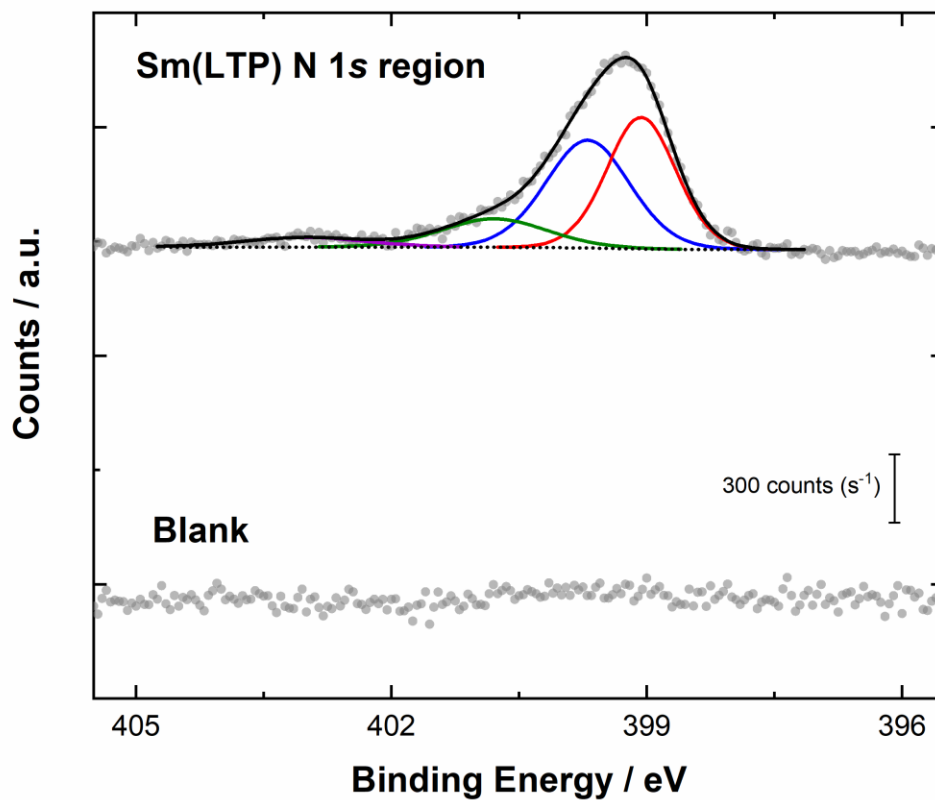
Figure A7. Spectrum of the **Sm(LTP)** N 1*s* region overlaid with a blank ketjen black electrode spectrum from Al-source data. Legend: gray dots: data; dashed black line: fitting background; blue, red, and green lines: N 1s contributions from the nitrogens of the complex (areas constrained to a 3:3:1 area, respectively); purple line: N 1s contribution from a protonated amine species; black solid line: overall fit.
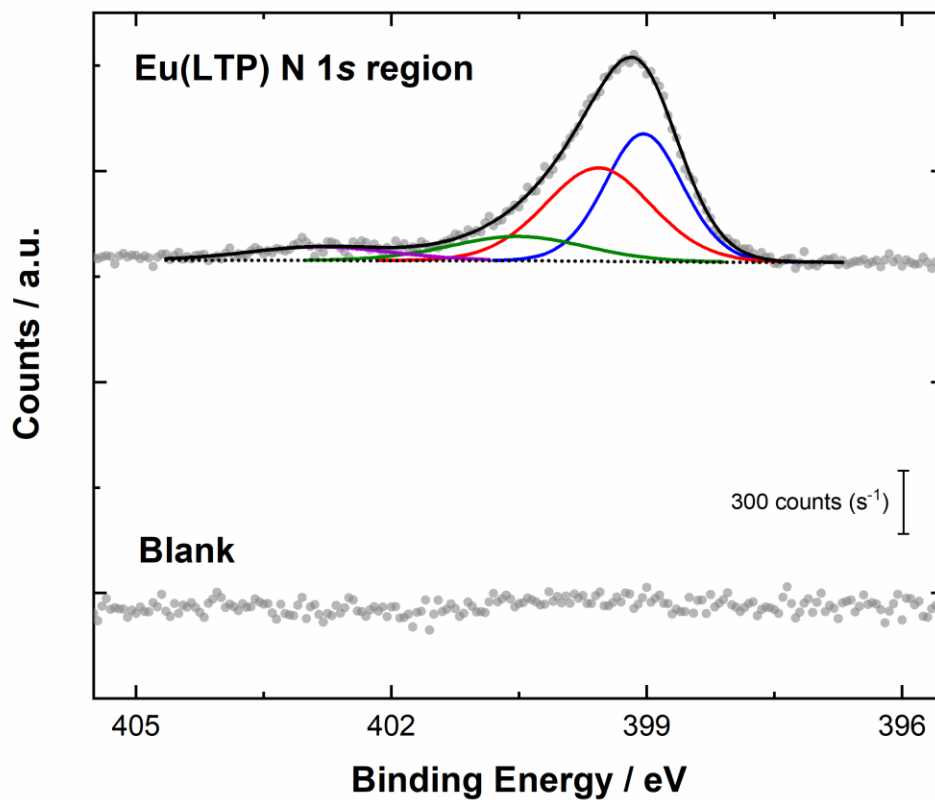
Figure A8. Spectrum of the **Eu(LTP)** N 1*s* region overlaid with a blank ketjen black electrode spectrum from Al-source data. Legend: gray dots: data; dashed black line: fitting background; blue, red, and green lines: N 1s contributions from the nitrogens of the complex (areas constrained to a 3:3:1 area, respectively); purple line: N 1s contribution from a protonated amine species; black solid line: overall fit.
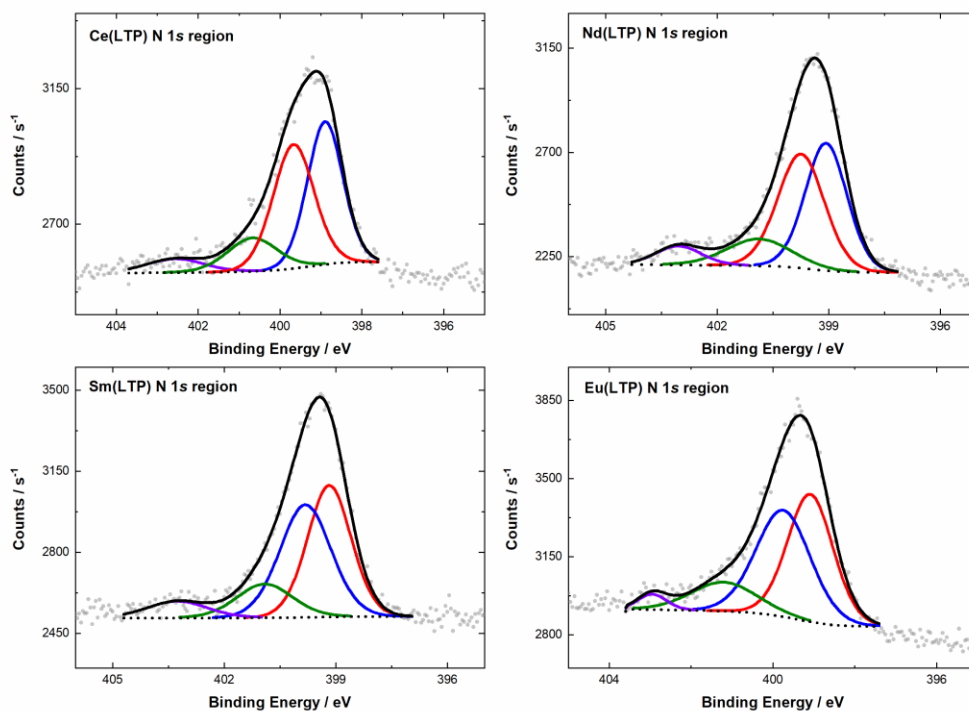
Figure A9. Mg-source X-ray photoelectron spectra for the N 1s region for electrodes functionalized with **M(LTP)** complexes. Legend: gray dots: data; dashed black lines: fitting background; blue, red and green lines: fitting curves for three distinct nitrogen environments (constrained to 3:3:1 area ratio); continuous black line: overall fit.
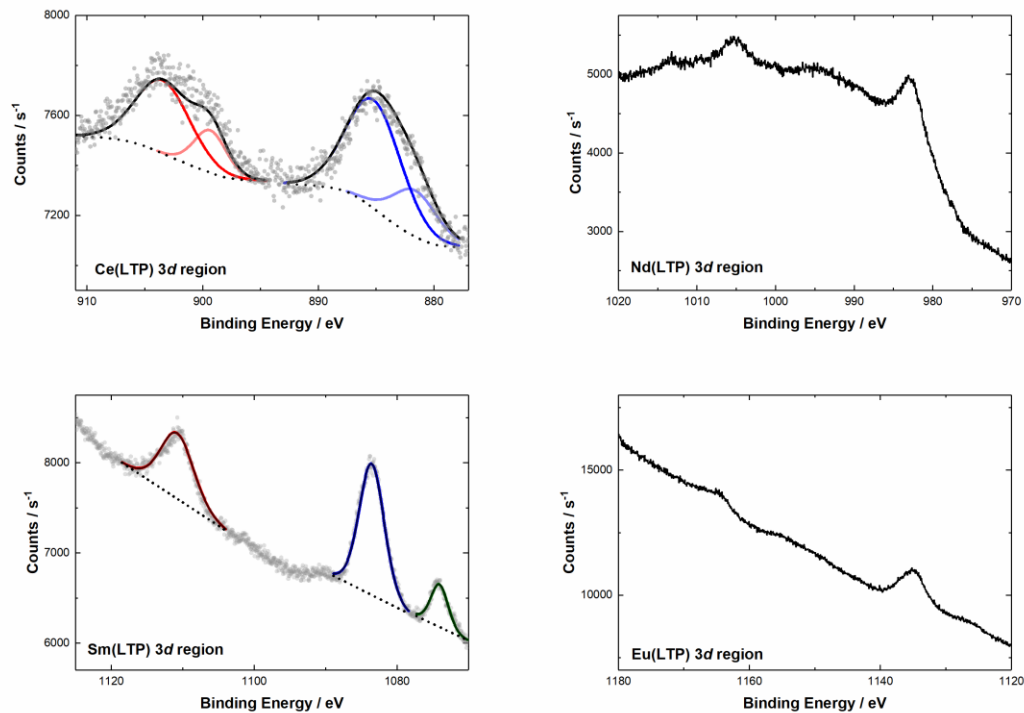
Figure A10. Mg-source XPS specta of the M 3d region of the **M(LTP)** complexes. Legend: gray dots: data; dashed black lines: fitting background; dark blue lines: M $3d_{5/2}$ peak fit; dark red lines: M $3d_{3/2}$ peak fit (constrained to 2/3 area with respect to M $3d_{5/2}$); green lines: shake-up and shake-down peaks fit; continuous black line: overall fit. For the **Ce(LTP)** 3d region, contributions from the Ce(III) $3d_{3/2}$ and $3d_{5/2}$ peaks have been represented by a lighter red line and lighter blue line, respectively. M 3d peaks for **Nd(LTP)** and **Eu(LTP)** were present, but fits could not be reliably assigned due to the high background from the Mg source.
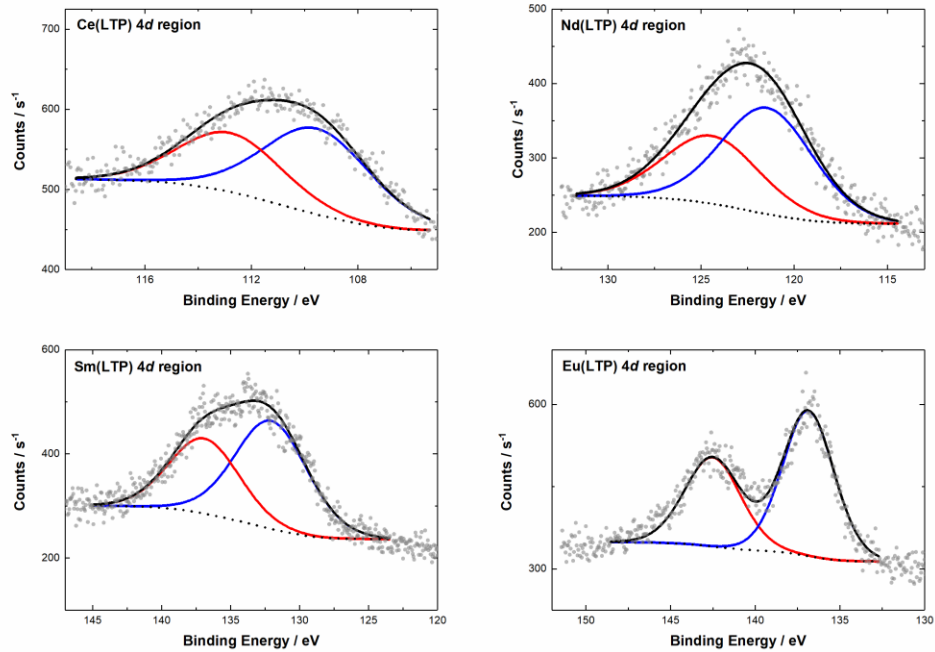
Figure A11. Mg-source X-ray photoelectron spectra for the respective M 4d regions for **M(LTP)** complexes. Legend: gray dots: data; dashed black lines: fitting background; blue lines: M $4d_{5/2}$ peak fit; red lines: M $4d_{3/2}$ peak fit (constrained to 2/3 area with respect to M $4d_{5/2}$); continuous black line: overall fit.
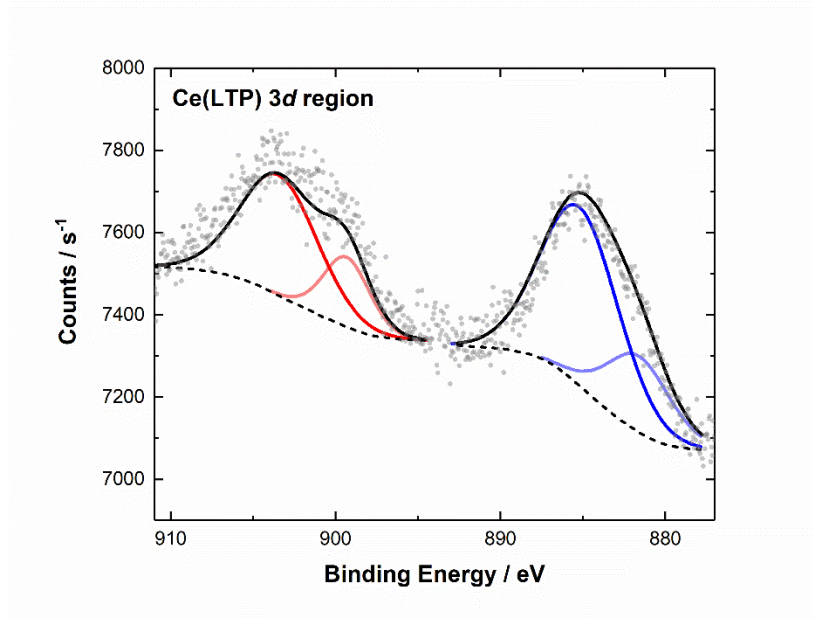
Figure A12. Spectrum of **Ce(LTP)** M 3d region from Mg-source data. Legend: gray dots: data; dashed black line: fitting background; dark blue line: Ce $3d_{5/2}$ peak fit; dark red line: Ce $3d_{3/2}$ peak fit (constrained to 2/3 area with respect to Ce $3d_{5/2}$); light blue line: contribution from Ce(III) $3d_{5/2}$; light red line: contribution from the Ce(III) $3d_{3/2}$ (constrained to a 2/3 area with respected to Ce(III) $3d_{5/2}$); continuous black line: overall fit.

Figure A13. Spectrum of **Sm(LTP)** M 3d region overlaid with a blank Ketjen black electrode from Mg-source data. Legend: gray dots: data; dashed black line: fitting background; blue line: Sm $3d_{5/2}$ peak fit; red line: Sm $3d_{3/2}$ peak fit (constrained to 2/3 area with respect to Sm $3d_{5/2}$); green lines: shake-up and shake-down peaks fit; continuous black line: overall fit.

Figure A14. Overlaid spectra of **Nd(LTP)** M 3d region with a blank Ketjen black electrode from Mg-source data.
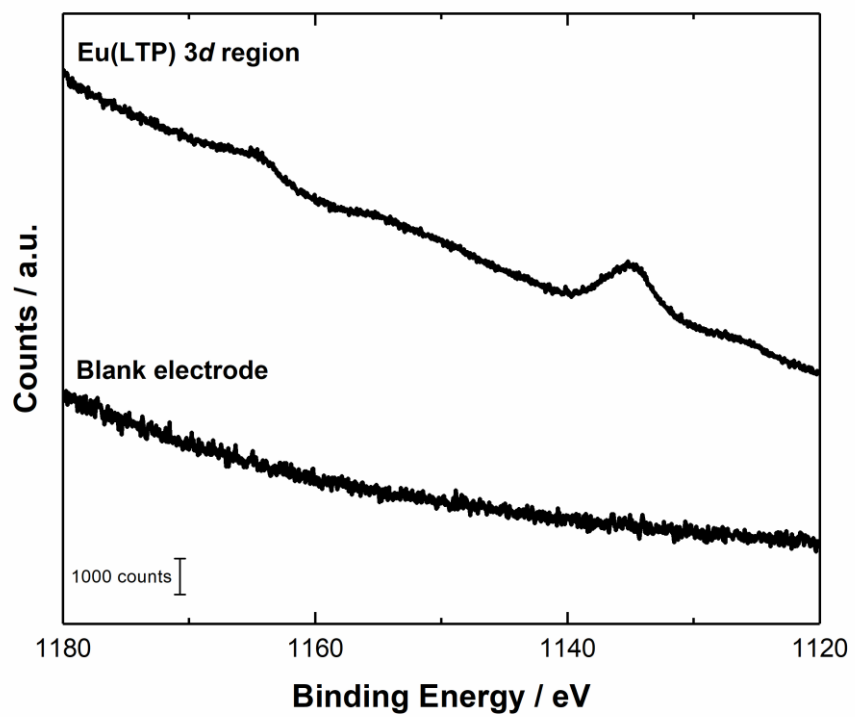
Figure A15. Overlaid spectra of **Eu(LTP)** M 3d region with a blank Ketjen black electrode from Mg-source data.
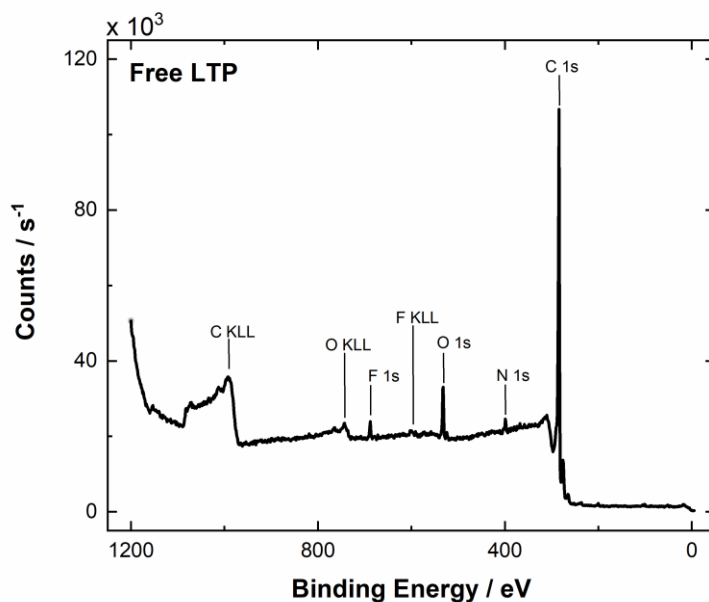
Figure A16. Mg Kα source XP spectrum of a Ketjen black electrode functionalized with free **LTP**.
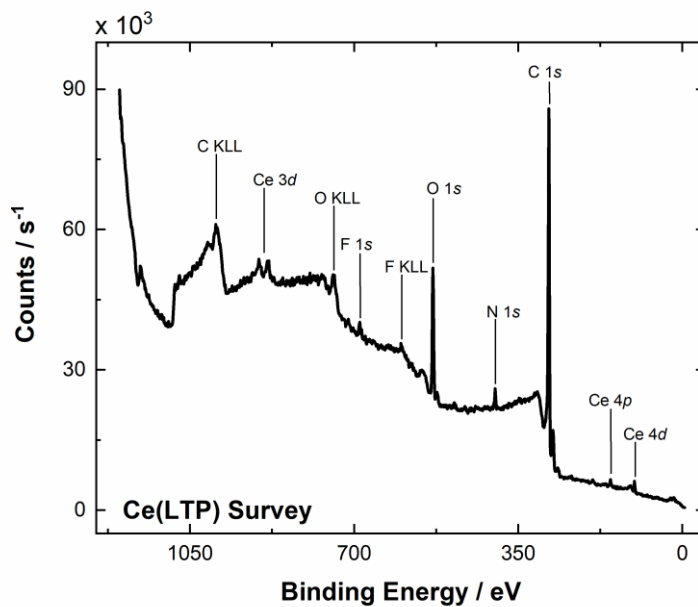
Figure A17. Mg Kα source XP spectrum of a Ketjen black electrode functionalized with **Ce(LTP)**.
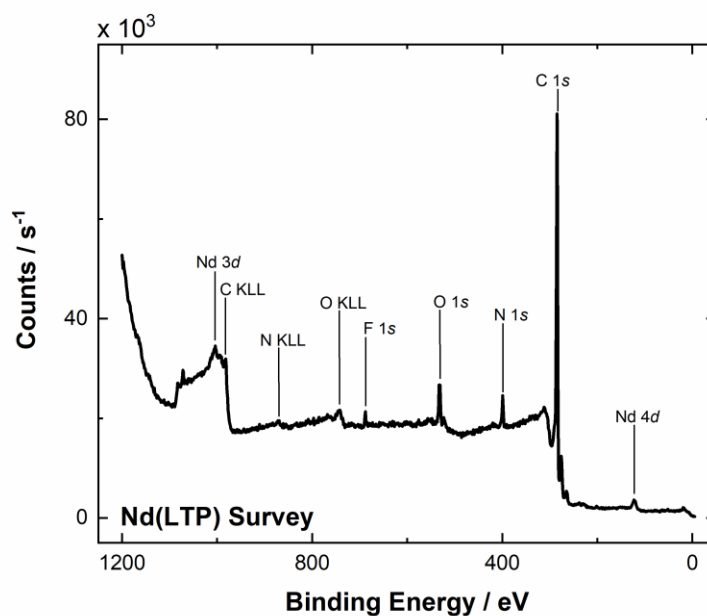
Figure A18. Mg Kα source XP spectrum of a Ketjen black electrode functionalized with **Nd(LTP)**.
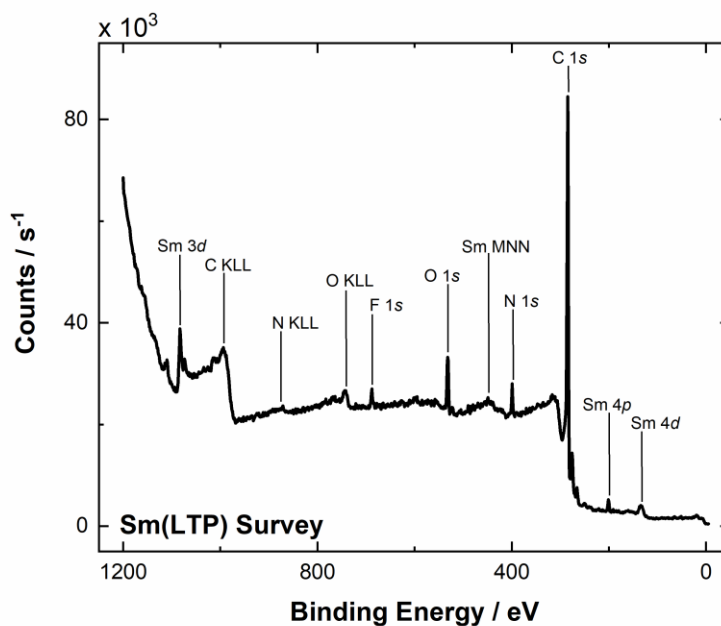
Figure A19. Mg Kα source XP spectrum of a Ketjen black electrode functionalized with **Sm(LTP)**.
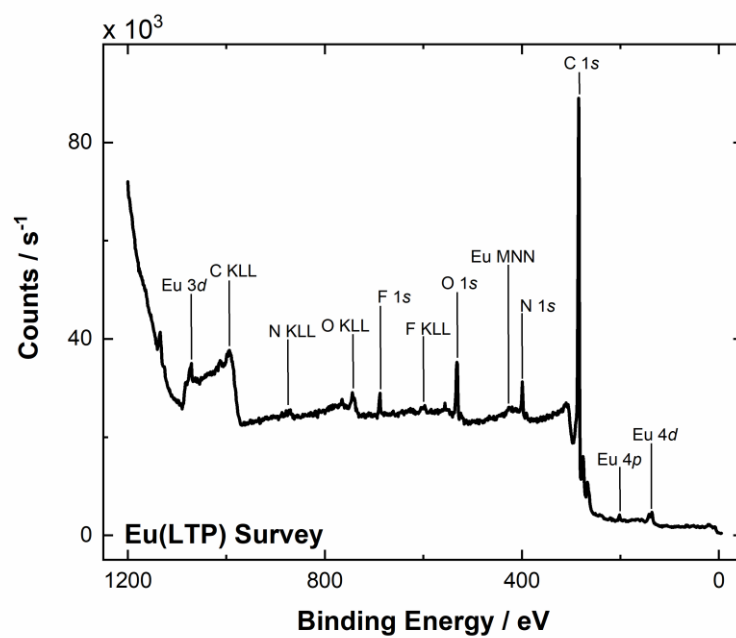
Figure A20. Mg Kα source XP spectrum of a Ketjen black electrode functionalized with **Eu(LTP)**.
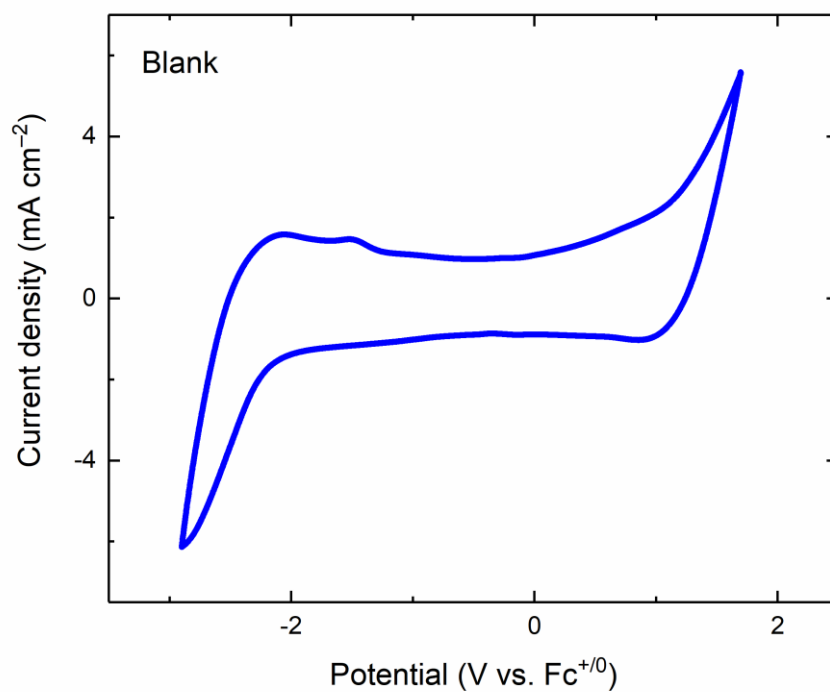
Figure A21. Cyclic voltammetry of a blank Ketjen black electrode (CH_3CN, 0.1 M [$^nBu_4N$][PF_6]) at a scan rate of 100 mV/s.
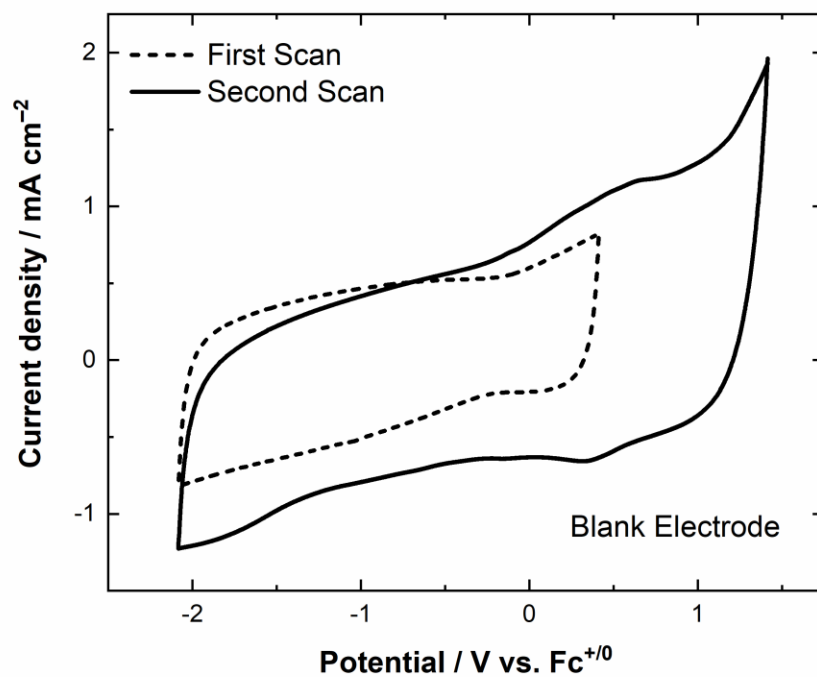
Figure A22. Cyclic voltammetry of a blank Ketjen black electrode at various potential ranges at a scan rate of 100 mV/s (CH_3CN, 0.1 M [$^nBu_4N$][PF_6]).
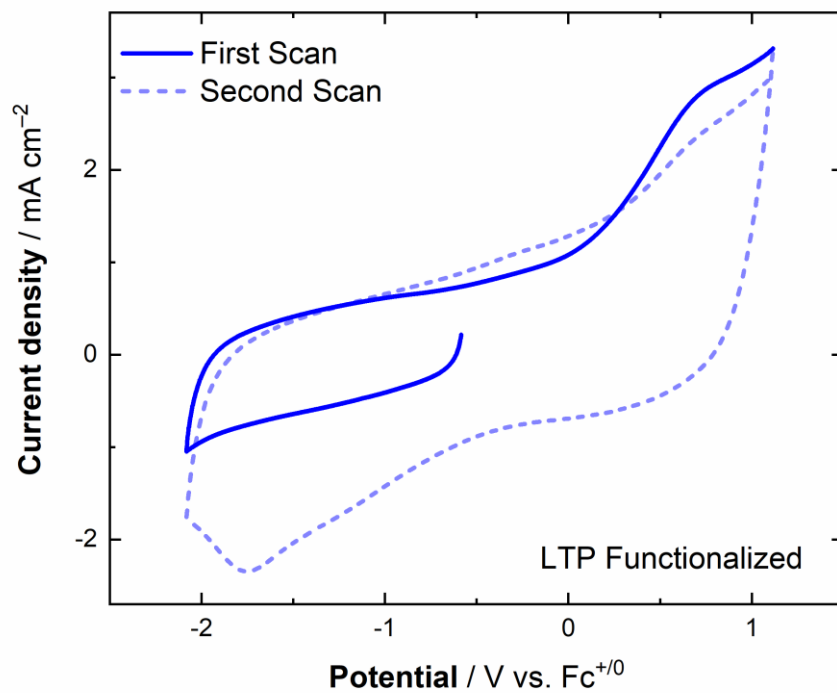
Figure A23. Cyclic voltammetry of free **LTP** immobilized on a Ketjen black electrode at a scan rate of 100 mV/s (CH_3CN, 0.1 M [$^nBu_4N$][PF_6]).
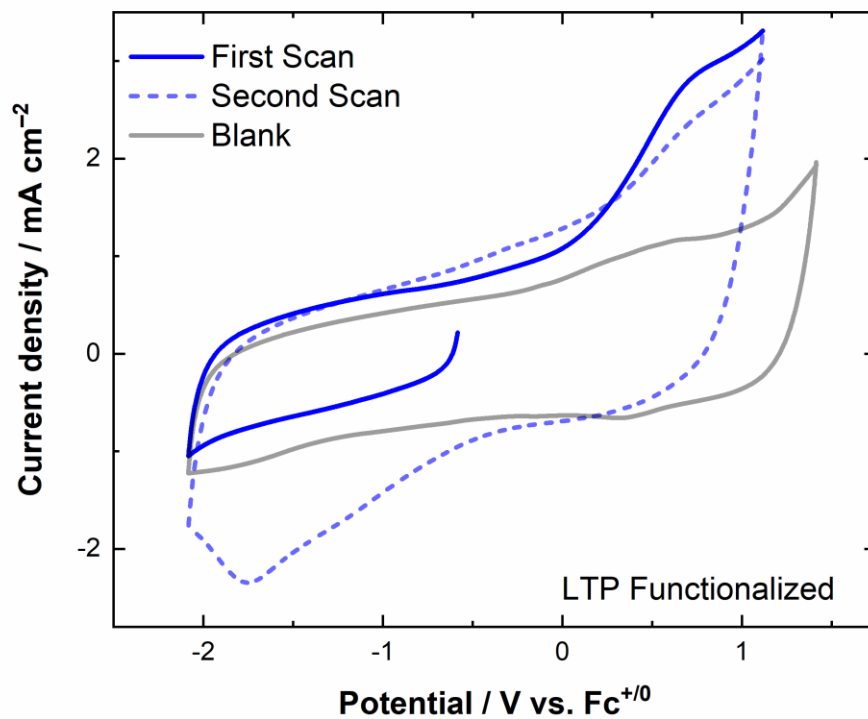
Figure A24. Overlay data of the cyclic voltammetry associated with a blank Ketjen black electrode and a Ketjen black electrode functionalized with free **LTP** (CH_3CN, 0.1 M [$^{n}Bu_4N$][PF_6]) at scan rates of 100 mV/s.

154
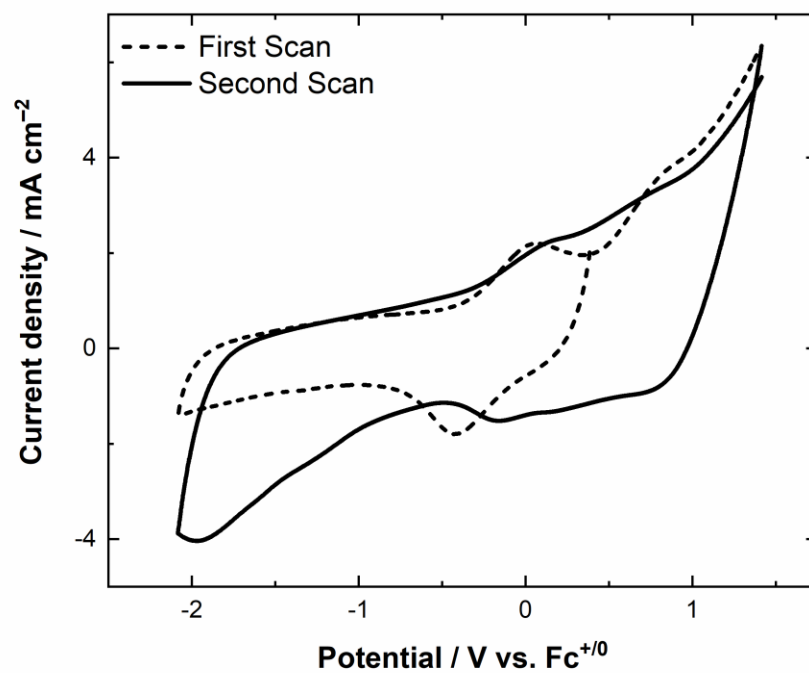
Figure A25. Cyclic voltammetry for the **Ce(LTP)** complex at various potential ranges (CH_3CN, 0.1 M [$^nBu_4N$][PF_6]) at a scan rate of 100 mV/s.
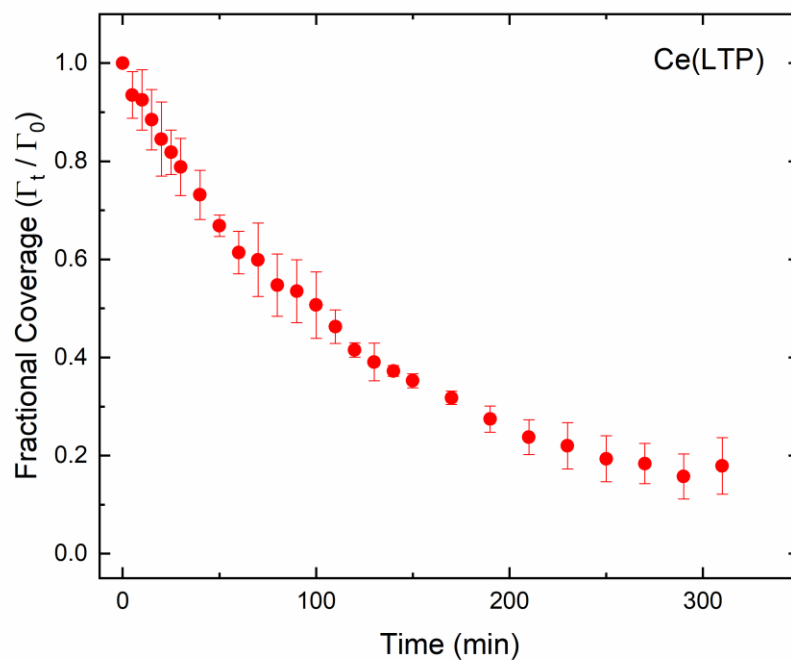
Figure A26. Fractional coverage plot of **Ce(LTP)** over time. Measurements were made by taking a cyclic voltammogram at distinct time points. The currents of the anodic and cathodic peaks were then integrated and converted to moles of **Ce(LTP)**. Fractional coverage was calculated by taking the amount of **Ce(LTP)** (in moles) at time (t) and dividing by the starting amount of **Ce(LTP)** (in moles).
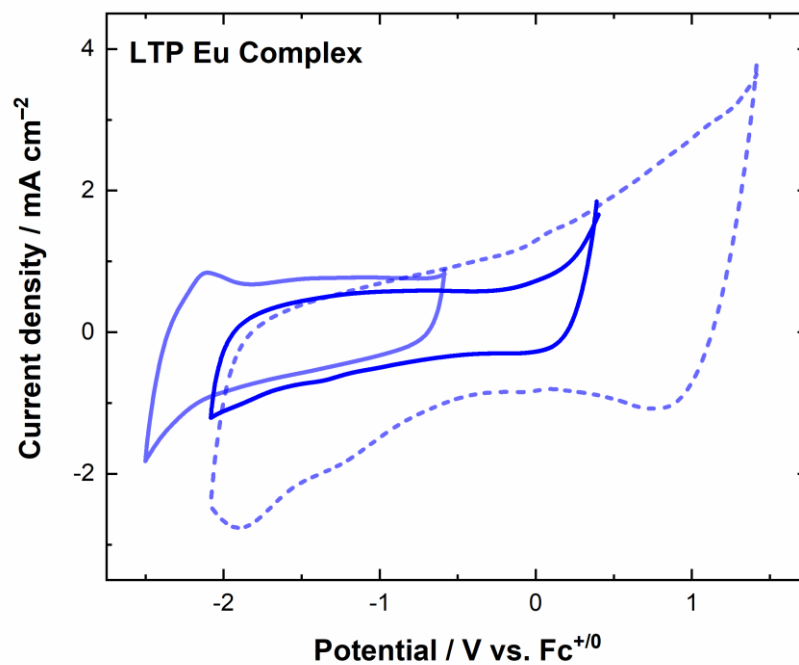
Figure A27. Cyclic voltammetry studies of a Ketjen black electrode functionalized with the **Eu(LTP)** complex to probe for the presence of the potentially accessible Eu(III/II) couple (CH_3CN, 0.1 M [$^nBu_4N$][PF_6]) at a scan rate of 100 mV/s.
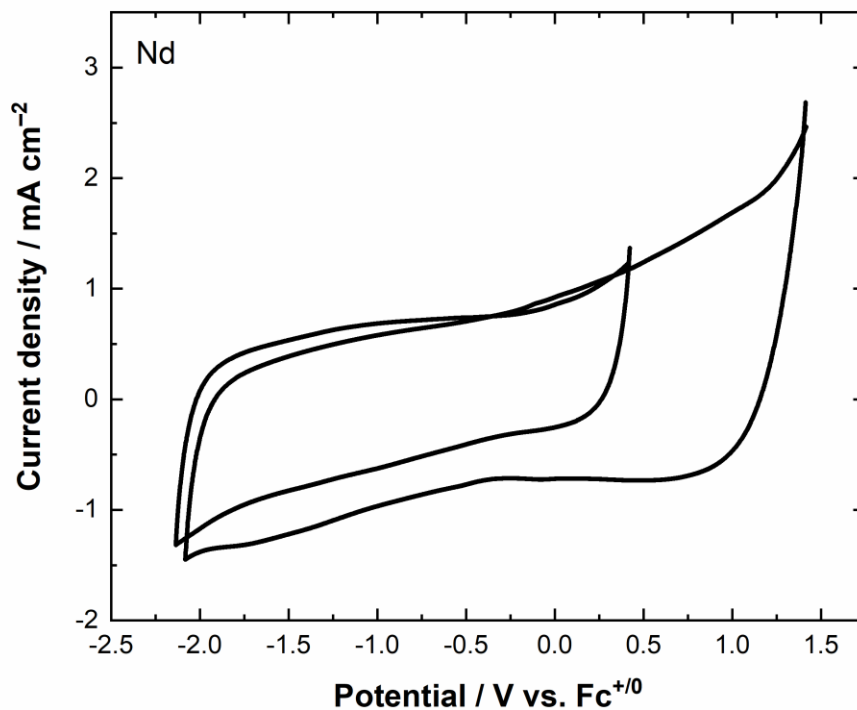
Figure A28. Cyclic voltammetry study of a Ketjen black electrode functionalized with the **Nd(LTP)** complex to probe for the presence of a potentially accessible redox couple (CH_3CN, 0.1 M [$^nBu_4N$][PF_6]) at a scan rate of 100 mV/s.
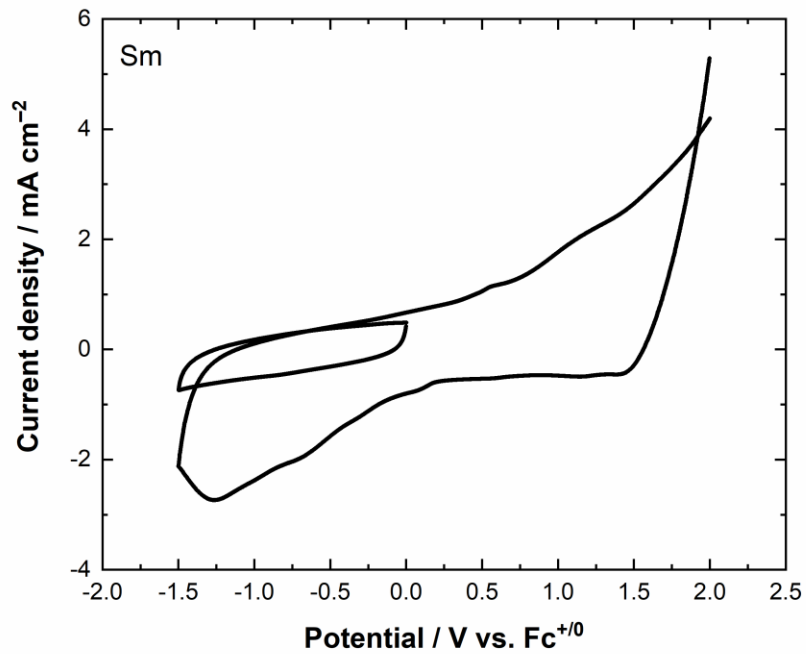
Figure A29. Cyclic voltammetry study of a Ketjen black electrode functionalized with the **Sm(LTP)** complex to probe for the presence of a potentially accessible redox couple (CH_3CN, 0.1 M [$^nBu_4N$][PF_6]) at a scan rate of 100 mV/s.
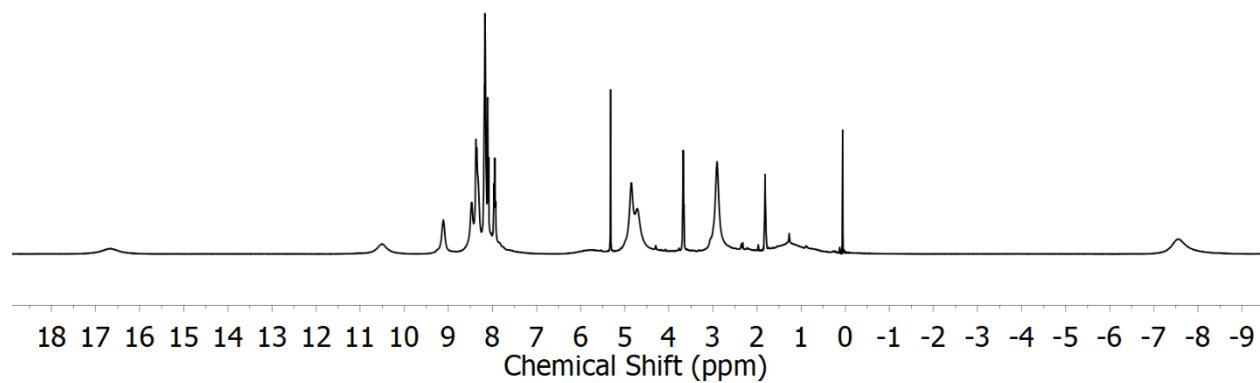
Figure A30. 400 MHz ^{1}H NMR spectrum of **Ce(LTP)** in CD$_2$Cl$_2$.
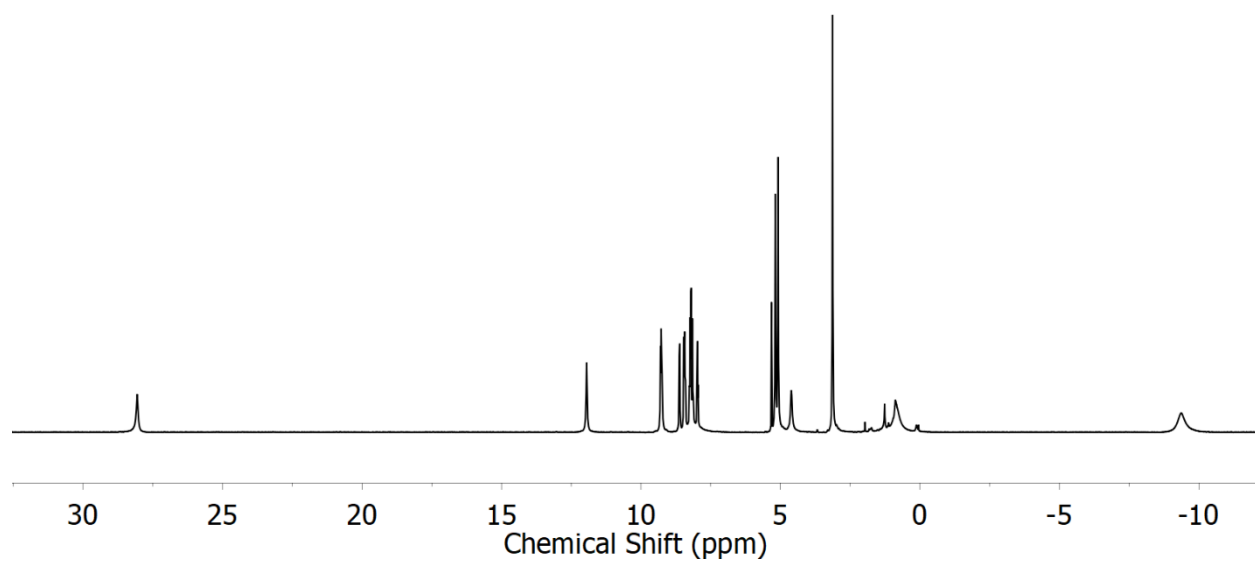
Figure A31. 400 MHz ^{1}H NMR spectrum of **Nd(LTP)** in CD$_2$Cl$_2$.
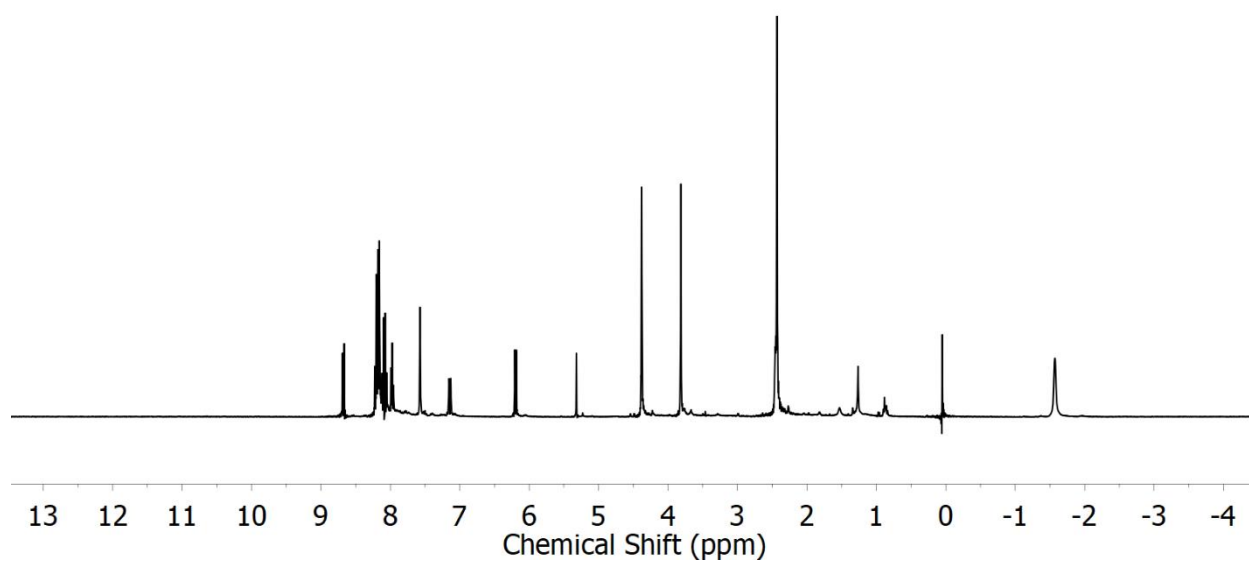
Figure A32. 400 MHz ^{1}H NMR spectrum of **Sm(LTP)** in CD_2Cl_2.
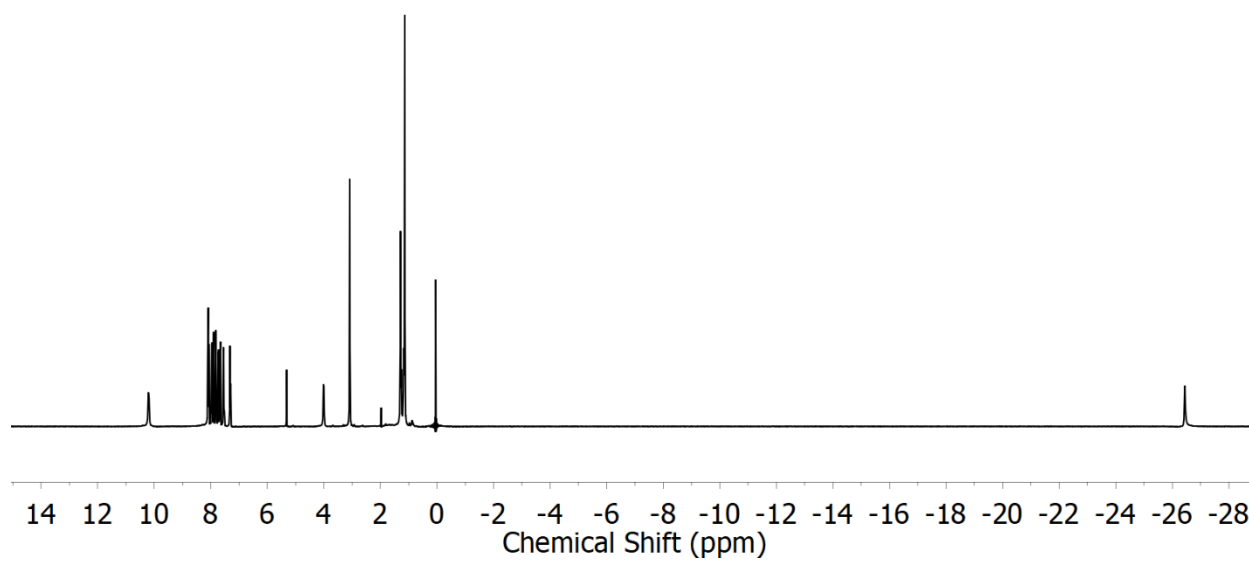
Figure A33. 400 MHz ^{1}H NMR spectrum of **Eu(LTP)** in CD_2Cl_2.
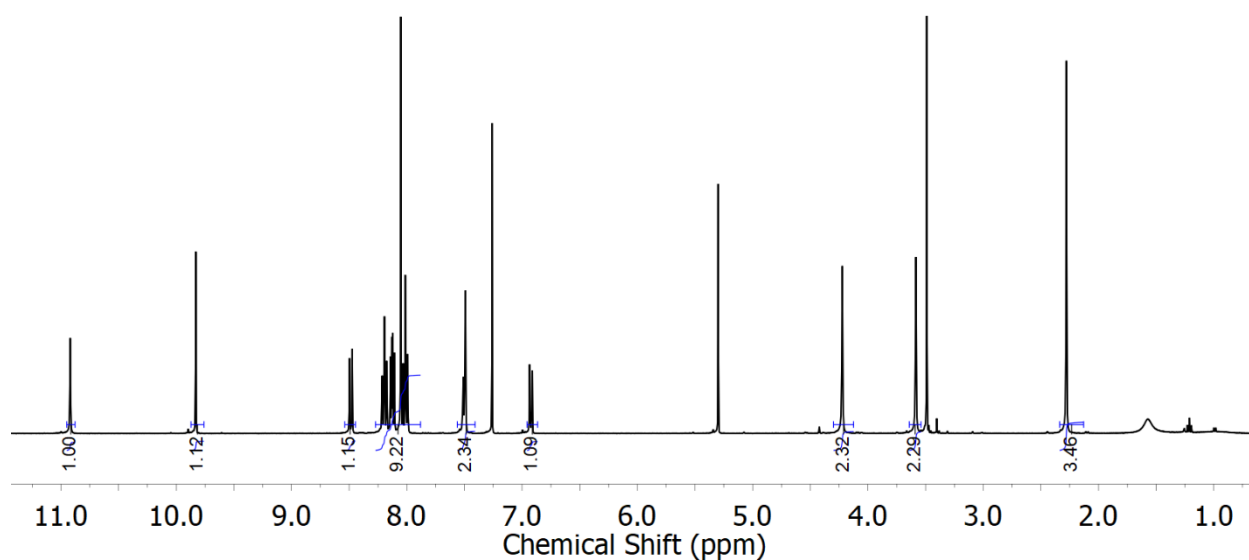
Figure A34. 400 MHz ^{1}H NMR spectrum of **1** in CDCl$_3$.
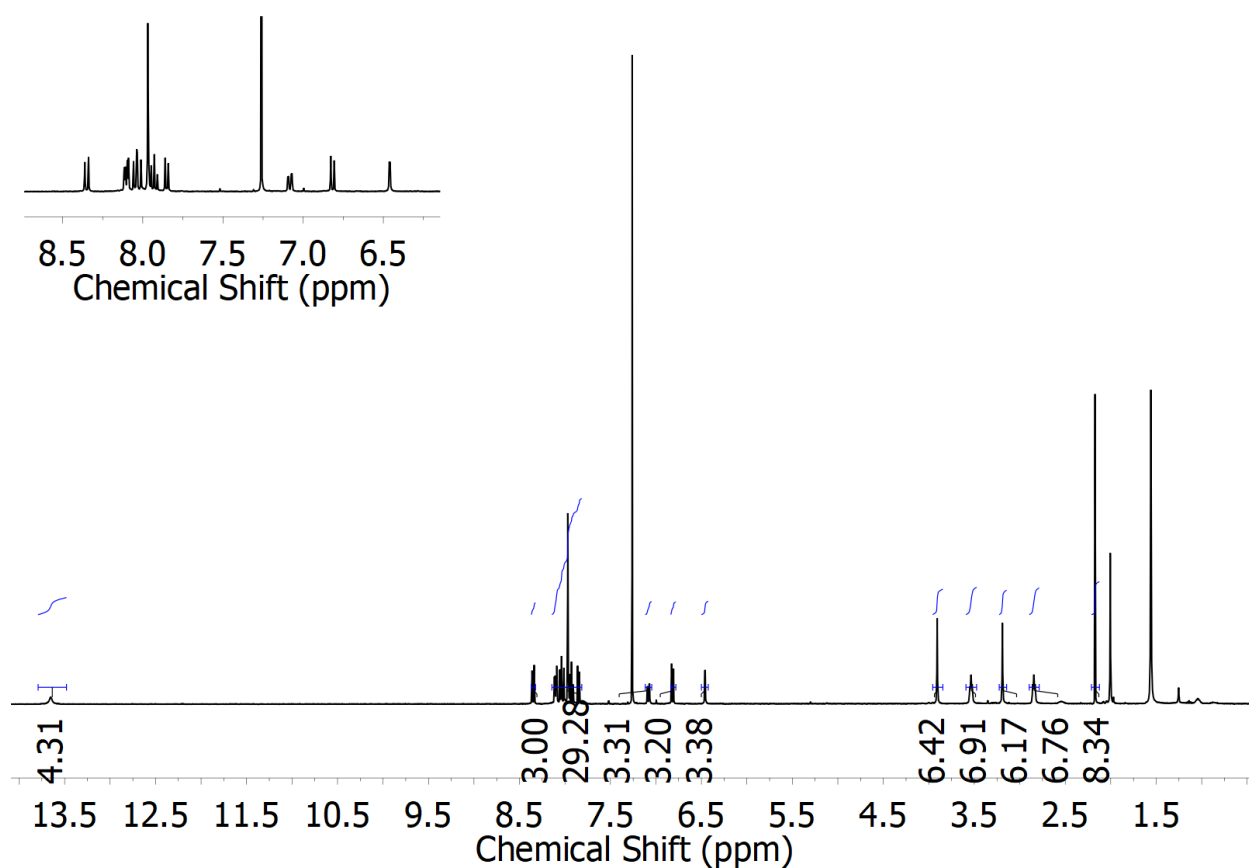
Figure A35. 400 MHz ^{1}H NMR spectrum of **LTP** in CDCl$_3$.

A.6. *References*

1.   Fennie, M. W.; DiMauro, E. F.; O'Brien, E. M.; Annamalai, V.; Kozlowski, M. C., *Tetrahedron* **2005,** *61*, 6249-6265.

2.   Chirakul, P.; Hampton, P. D.; Bencze, Z., *J. Org. Chem.* **2000,** *65*, 8297-8300.

3.   Birmingham, J. M.; Wilkinson, G., *J. Am. Chem. Soc.* **1956,** *78*, 42-44.

4.   Orchard, A. F., *Handbook of X-ray and ultraviolet photoelectron spectroscopy*. Heyden: London, 1977.

Appendix B

Supplemental Information for Chapter 3:

Electrochemical Properties of Molecular Uranyl Complexes

on Carbon Electrodes

Appendix B

Supplemental Information for Chapter 3:

Electrochemical Properties of Molecular Uranyl Complexes on Carbon Electrodes

Contents

B.1. *Experimental Details*

Caution! *Depleted uranium (primary isotope ^{238}U) is a weak α-emitter (4.197 MeV) with a half-life of 4.47 × 10^9 years. Manipulations and reactions should be performed by trained personnel in monitored fume hoods or in an inert atmosphere glovebox in a radiation laboratory equipped with α-counting equipment.*

B.1.1. *General considerations*

All manipulations were carried out in dry N_2-filled gloveboxes (Vacuum Atmospheres Co., Hawthorne, CA) or under N_2 atmosphere using standard Schlenk techniques unless otherwise noted. All solvents were of commercial grade and dried over activated alumina using a PPT Glass Contour (Nashua, NH) solvent purification system prior to use, and were stored over molecular sieves. All chemicals were purchased from major commercial suppliers and used as received after extensive drying. Deuterated NMR solvents were purchased from Cambridge Isotope Laboratories: CD_2Cl_2 was dried over CaH_2. 5-(chloromethyl)-2-hydroxybenzaldehyde, 3-(chloromethyl)-2-hydroxy-5-methylbenzaldehyde, *N*-methyl-1-(pyren-1-yl)methanamine, and **A** were synthesized according to adapted published procedures.[1-2] **1-L**, **1-U**, **3-L**, and **3-U** complexes were prepared according to literature procedure.[3-5] ^1H and ^{13}C NMR spectra were collected on 400 or 500 MHz Bruker spectrometers and referenced to the residual protio-solvent signal in the case of ^1H and ^{13}C. Chemical shifts (δ) are reported in units of ppm and coupling constants (*J*) are reported in Hz.

B.1.2. *Electrochemistry*

Electrochemical experiments were carried out in a dry N_2-filled glovebox. Measurements were made with a Gamry Reference 600 Plus Potentiostat/Galvanostat utilizing a standard three electrode set-up using 0.10 M tetra(n-butylammonium) hexafluorophosphate (Sigma-Aldrich; electrochemical grade) in dimethylformamide or acetonitrile as the supporting electrolyte.

For homogeneous experiments, basal plane of highly oriented pyrolytic graphite (HOPG) (GraphiteStore.com, Buffalo Grove, Ill.; surface area: 0.09 cm^2) was used as the working electrode, a platinum wire (Kurt J. Lesker, Jefferson Hills, PA; 99.99%, 0.5 mm diameter) was used as the counter electrode, and a platinum wire served as the pseudo-reference electrode (Kurt J. Lesker, Jefferson Hills, PA; 99.99%, 0.5 mm diameter). At the end of each experiment, ferrocene (Sigma Aldrich; twice-sublimed) was added to the electrolyte solution as the external reference. The experimental data was referenced to the midpoint potential for the ferrocenium/ferrocene couple (denoted as $Fc^{+/0}$).

For immobilized electrochemical measurements, all experiments were carried out in an inert atmosphere N_2-filled glovebox utilizing a custom-made Teflon cell with an O-ring seal used as the geometric area of the exposed electrode (0.28 cm^2). The platinum counter and the platinum quasi-reference electrodes were immersed in the electrolyte solution. The experimental data was referenced to the midpoint potential of the ferrocenium/ferrocene couple as an external reference.

B.1.3. *Synthetic Procedures*

A
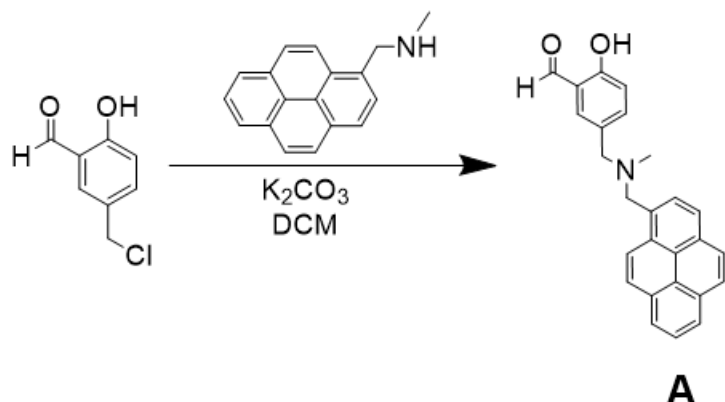
Synthesis of A

See synthesis of **1** in **Appendix A** for synthetic procedure and corresponding ^{1}H NMR spectrum.

2 L

A
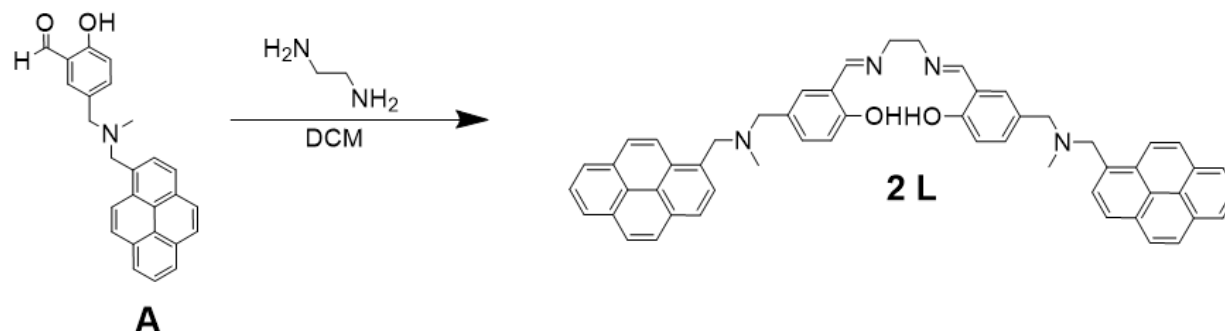
Synthesis of 2-L

In a 100 mL roundbottom flask, 2.05 equivalents of compound **A** (1.001 g, 2.64 mmol) was

dissolved in DCM. Sodium sulfate (5 equiv.) was added to the flask along with 1 equivalent of

ethylenediamine (0.077 g, 1.28 mmol) added dropwise. Upon addition of the ethylenediamine,

the solution's yellow color darkened. The mixture was stirred at room temperature overnight,

and the sodium sulfate removed via filtration through a Celite pad. The volatiles were removed

in vacuo to give a yellow oil. The yellow oil was then purified by column chromatography by

washing the excess aldehyde starting material off with DCM and then eluting the product with a

90:10 mixture of DCM:NEt₃. Extensive drying at reduced pressure led to foaming of the oil to give a solid material (0.90 g, 87% yield). ^{1}H NMR (400 MHz, CDCl₃) δ 13.14 (s, 2H), 8.41 (d, J = 9.2 Hz, 2H), 8.28 (s, 2H), 8.21 – 7.93 (m, 18H), 7.24 (d, 2H), 7.17 (d, J = 2.1 Hz, 2H), 6.88 (d, J = 8.4 Hz, 2H), 4.12 (s, 4H), 3.88 (s, 4H), 3.50 (s, 4H), 2.18 (s, 6H). ^{13}C NMR (125 MHz, CDCl₃) δ 166.41, 159.99, 133.24, 131.85, 131.16, 130.78, 130.64, 129.77, 128.12, 127.30, 127.01, 126.96, 125.71, 124.92, 124.88, 124.83, 124.66, 124.22, 124.06, 118.06, 116.62, 61.27, 60.08, 60.06, 59.62, 42.11.
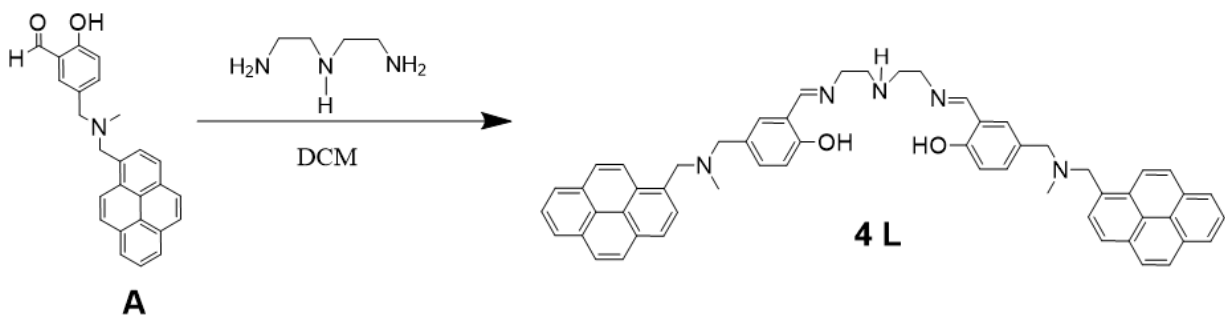
*Synthesis of **4-L***

In a 100 mL roundbottom flask, 2.05 equivalents of compound **A** (1.001 g, 2.64 mmol) was dissolved in DCM. Sodium sulfate (5 equiv.) was added to the flask along with 1 equivalent of diethylenetriamine (0.132 g, 1.28 mmol) added dropwise. Upon addition of the diethylenetriamine, the solution's yellow color darkened. The mixture was stirred at room temperature overnight, and the sodium sulfate removed via filtration through a Celite pad. The volatiles were removed *in vacuo* to give a yellow oil. The yellow oil was then purified by column chromatography by washing the excess aldehyde starting material off with DCM and then eluting the product with a 90:10 mixture of DCM:NEt₃. Extensive drying at reduced pressure led to foaming of the oil to give a solid material (0.80 g, 73% yield). ^{1}H NMR (400 MHz, CD₂Cl₂) δ

13.22 (s, 2H), 8.46 (d, J = 9.2 Hz, 2H), 8.29 (s, 2H), 8.21 – 7.93 (m, 18H), 7.27 (dd, J = 8.4, 2.2

Hz, 2H), 7.20 (d, J = 2.1 Hz, 2H), 6.84 (d, J = 8.4 Hz, 2H), 4.13 (s, 4H), 3.65 (m, 4H), 3.52 (s,

4H), 2.94 (t, J = 6.0 Hz, 4H), 2.17 (s, 6H), 1.02 (t, J = 7.2 Hz, 1H). ^{13}C NMR (125 MHz,

CD$_2$Cl$_2$) δ 166.59, 160.75, 133.77, 133.74, 133.63, 132.42, 131.83, 131.46, 131.29, 130.44,

130.41, 129.99, 128.93, 128.89, 128.01, 127.94, 127.60, 127.53, 127.43, 127.39, 127.34, 126.43,

125.63, 125.60, 125.57, 125.51, 125.46, 125.43, 125.38, 125.36, 125.23, 124.96, 124.87, 124.83,

124.77, 124.74, 124.71, 118.92, 117.02, 61.95, 60.82, 60.16, 50.25, 46.76, 42.51.
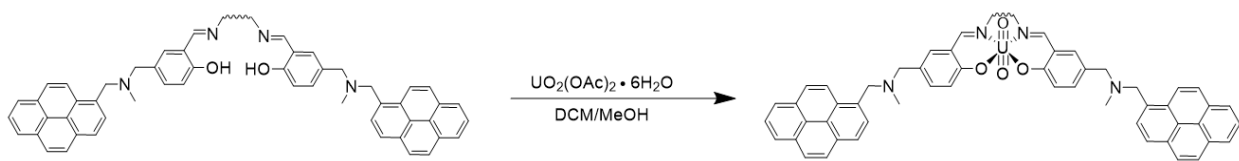
*General procedure for synthesis of **2-U** and **4-U** complexes*

To metallate, 1 equivalent of the free ligands **2-L** and **3-L** were dissolved in a 50:50 mixture of

DCM:MeOH to encourage the solubility of the free ligand. The solution of free ligand was

stirred until the solution became homogeneous. While the solution of free ligand was stirring, 1

equivalent of uranyl acetate hexahydrate (UO$_2$(OAc)$_2$ ● 6H$_2$O) was weighted out and

subsequently dissolved in a minimal amount of neat MeOH. The solution of uranyl acetate

hexahydrate was added slowly and dropwise to the solution of free ligand. Upon addition of the

uranyl solution, the yellow color of the ligand solution immediately darkened to a red-orange and

small amounts of orange precipitate could be observed. The container holding the uranyl solution

was rinsed with minimal amounts of neat MeOH to ensure all uranyl acetate hexahydrate had

been added to the ligand solution. The reaction mixture was allowed to stir overnight at room temperature, during which time more orange precipitate was formed. The reaction mixture was then filtered over a medium porosity frit and the collected red-orange solid was rinsed with cold MeOH. Extensive drying at reduced pressure yielded a red-orange powder corresponding to the **2-U** and **4-U** complexes.

2-U

Isolated as a dark orange solid (80%).^{1}H NMR (500 MHz, d_6-DMSO): δ 9.46 (br s, 2H), 8.53 (br d, $J = 9.3$ Hz, 2H), 8.3 – 8.0 (br m, 16H), 7.58 (br s, 4H), 6.94 (br s, 2H), 4.48 (br s, 4H), 4.21 (br s, 4H), 3.67 (br s, 4H), 2.88 (s, 3H), 2.73 (s, 3H).

4-U

Isolated as light orange solid (70%). ^{1}H NMR (500 MHz, CD_2Cl_2): δ 9.32 (s, 2H), 8.52 (d, $J = 9.2$ Hz, 2H), 8.24 – 7.96 (m, 16H), 7.67 (dd, $J = 8.5, 2.4$ Hz, 2H), 7.45 (s, 2H), 7.11 (d, $J = 8.4$ Hz, 2H), 4.69 (t, $J = 13.7$ Hz, 2H), 4.52 (d, $J = 14.3$ Hz, 3H), 4.21 (d, $J = 17.8$ Hz, 6H), 3.69 (d, $J = 18.7$ Hz, 6H), 2.26 (s, 6H).

B.2.   *NMR Spectra*
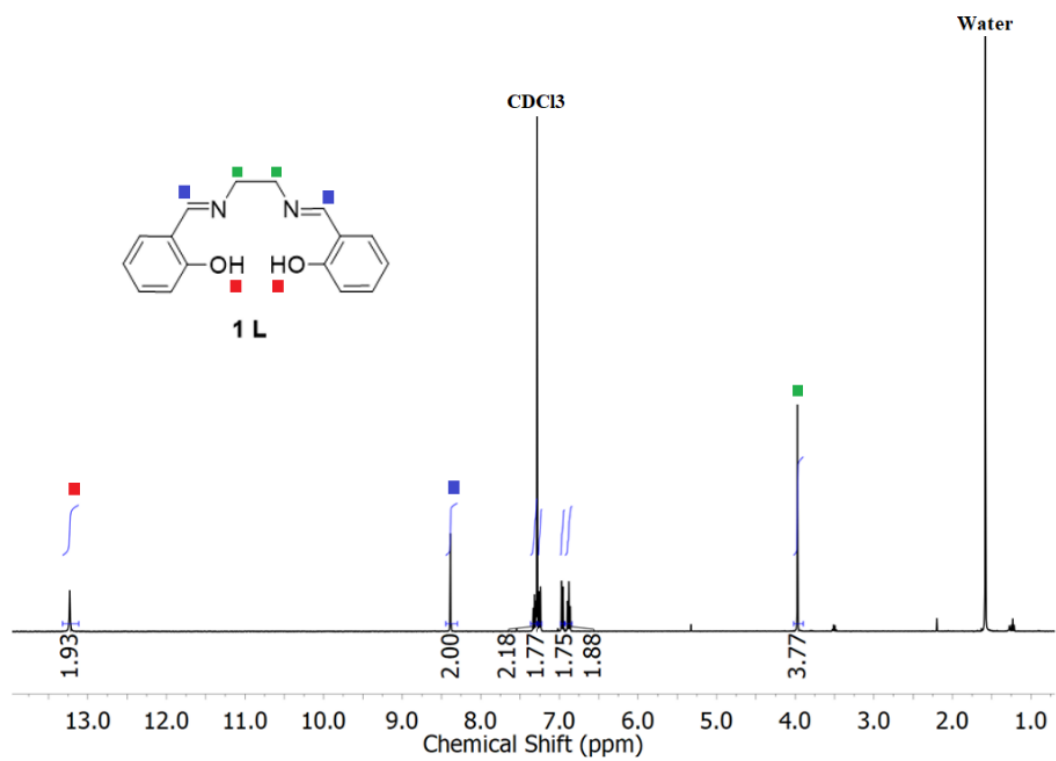
Figure B1. 400 MHz ^{1}H NMR spectrum of **1-L** in CDCl$_3$.
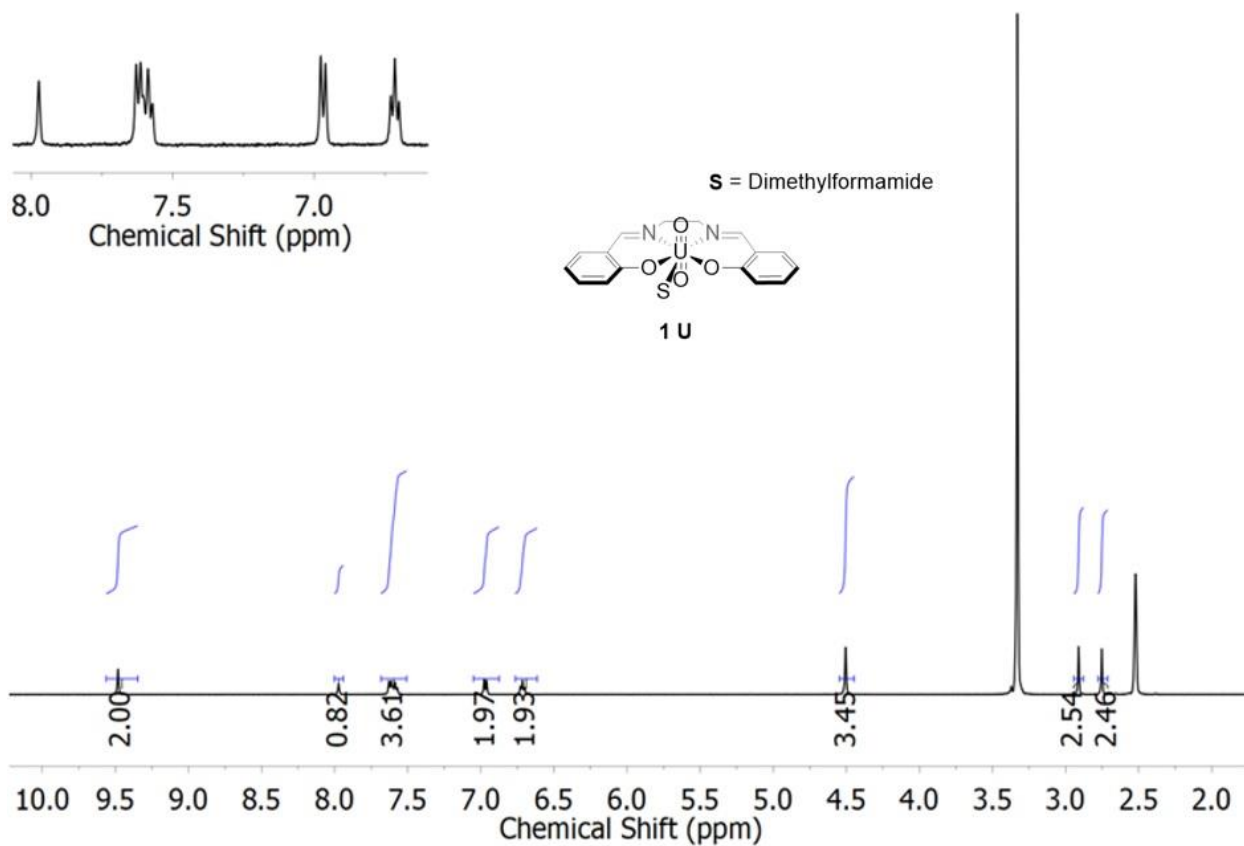
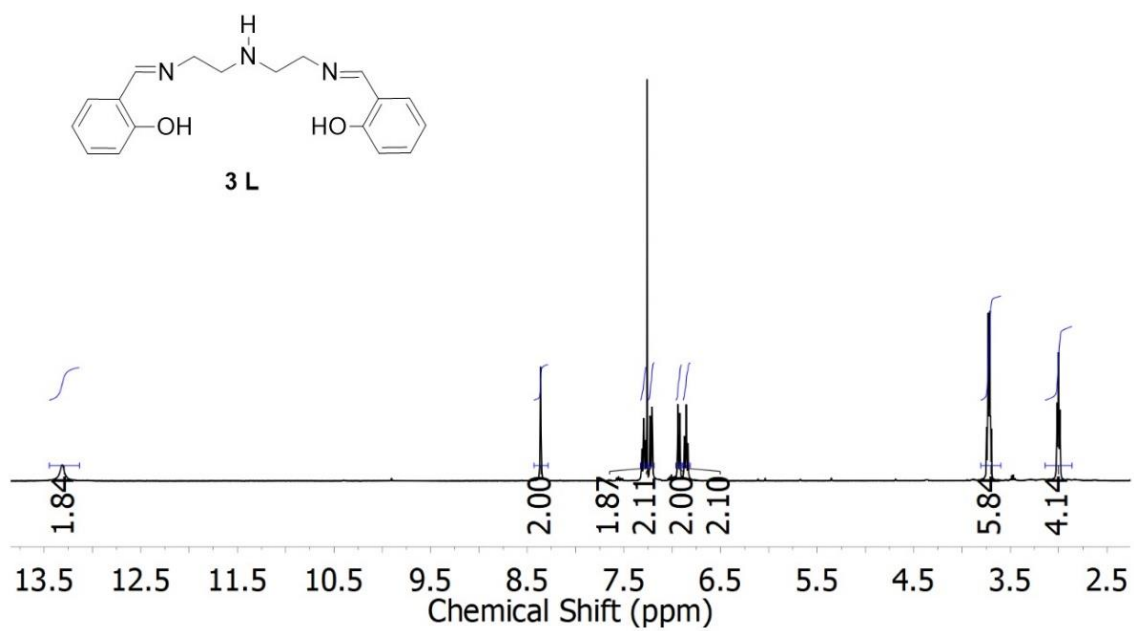**Figure B2.** 500 MHz ^{1}H NMR spectrum of the **1-U** complex in d_6-DMSO at 298 K.

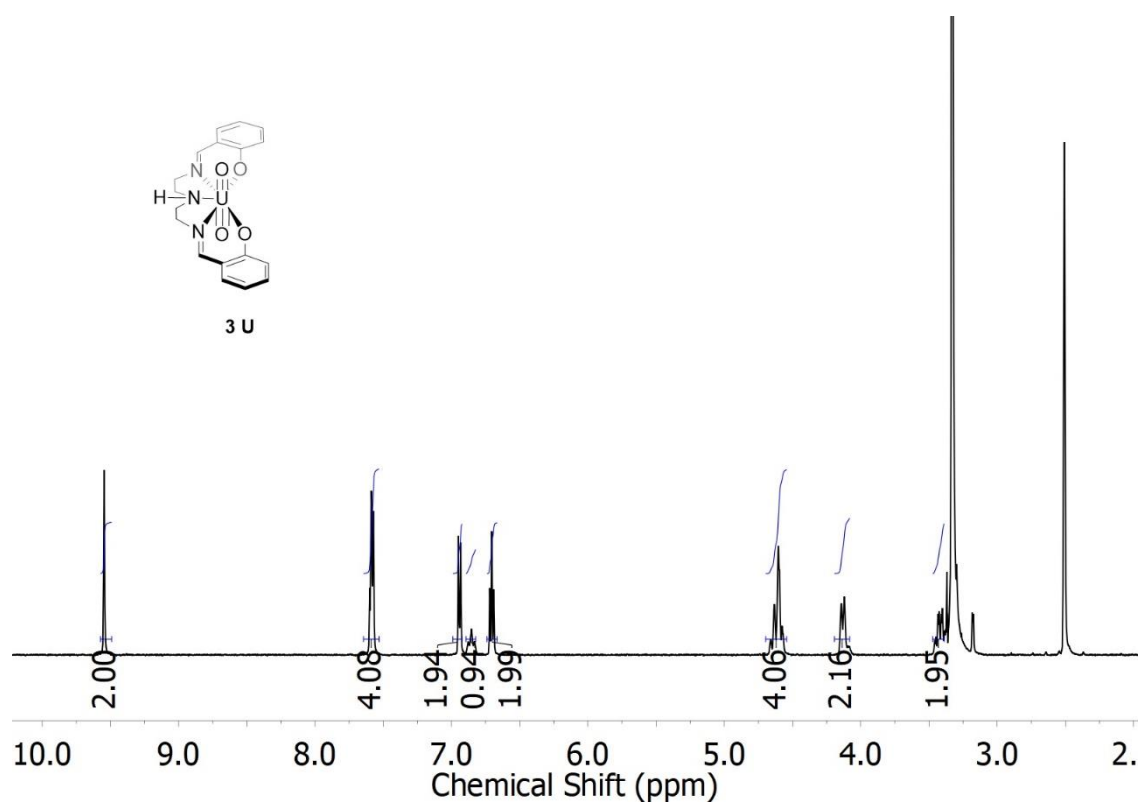**Figure B3**. 400 MHz ^{1}H NMR spectrum of **3-L** in CDCl$_3$.

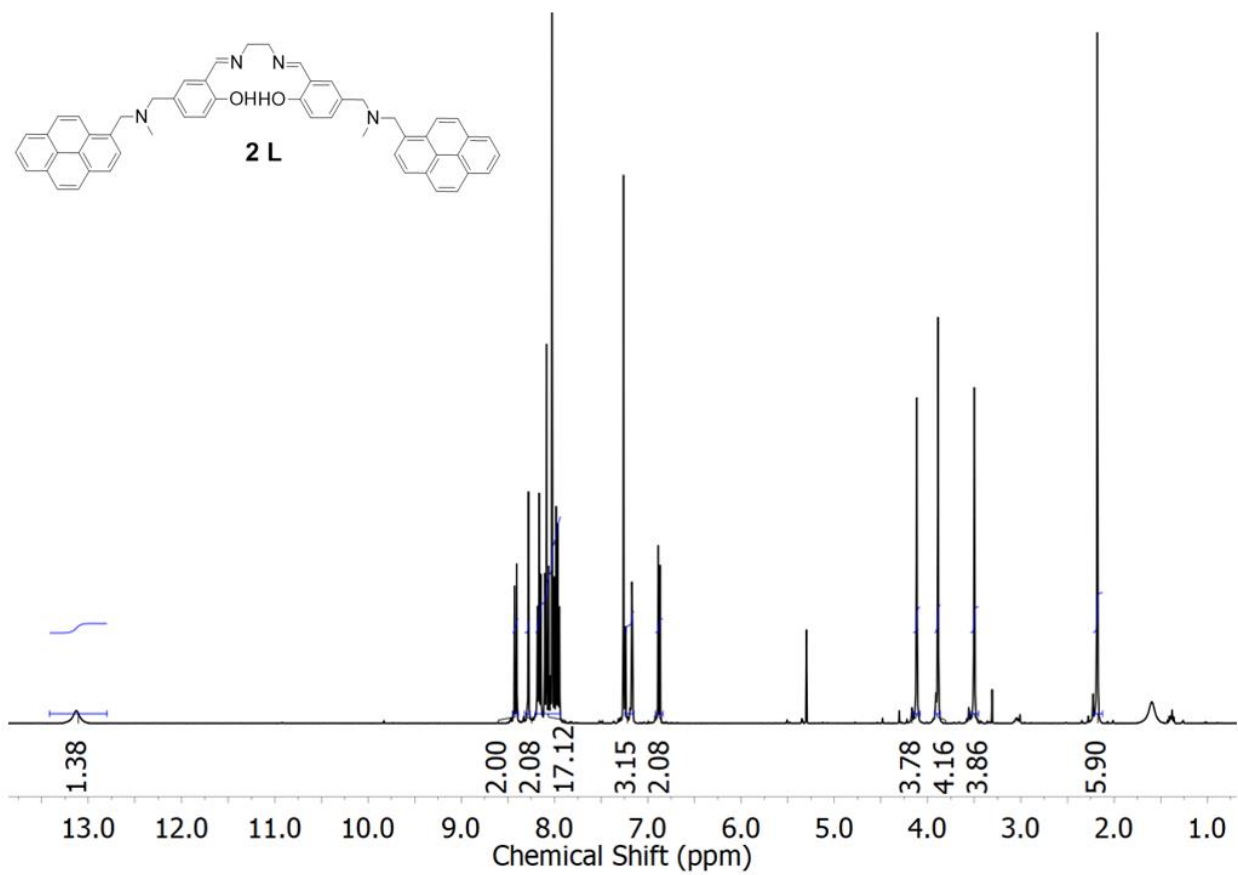**Figure B4**. 500 MHz ^{1}H NMR spectrum of **3-U** in d_6-DMSO.

Figure B5. 400 MHz ^{1}H NMR spectrum of **2-L** in CDCl$_3$.
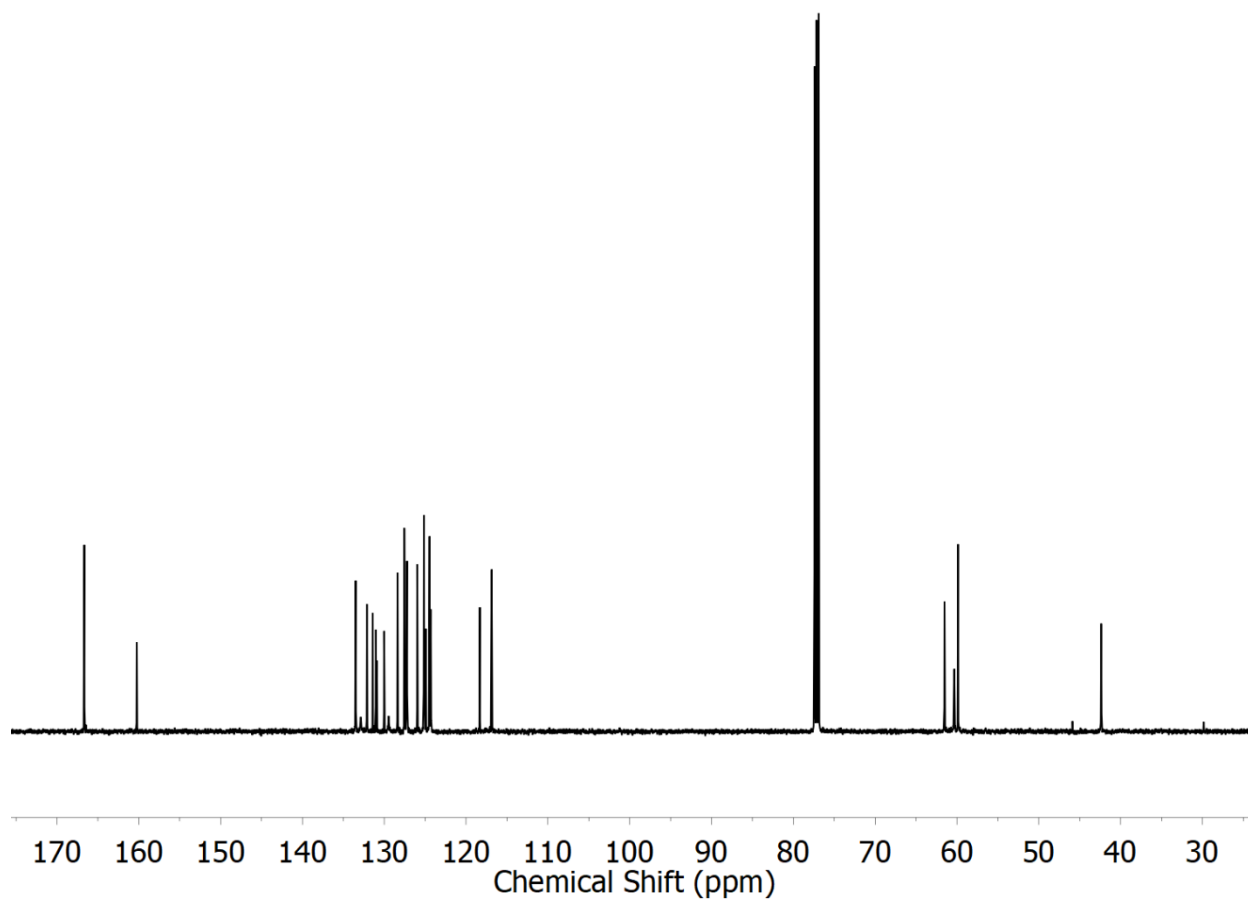
Figure B6. 125 MHz ^{13}C NMR spectrum of **2-L** in CDCl$_3$.
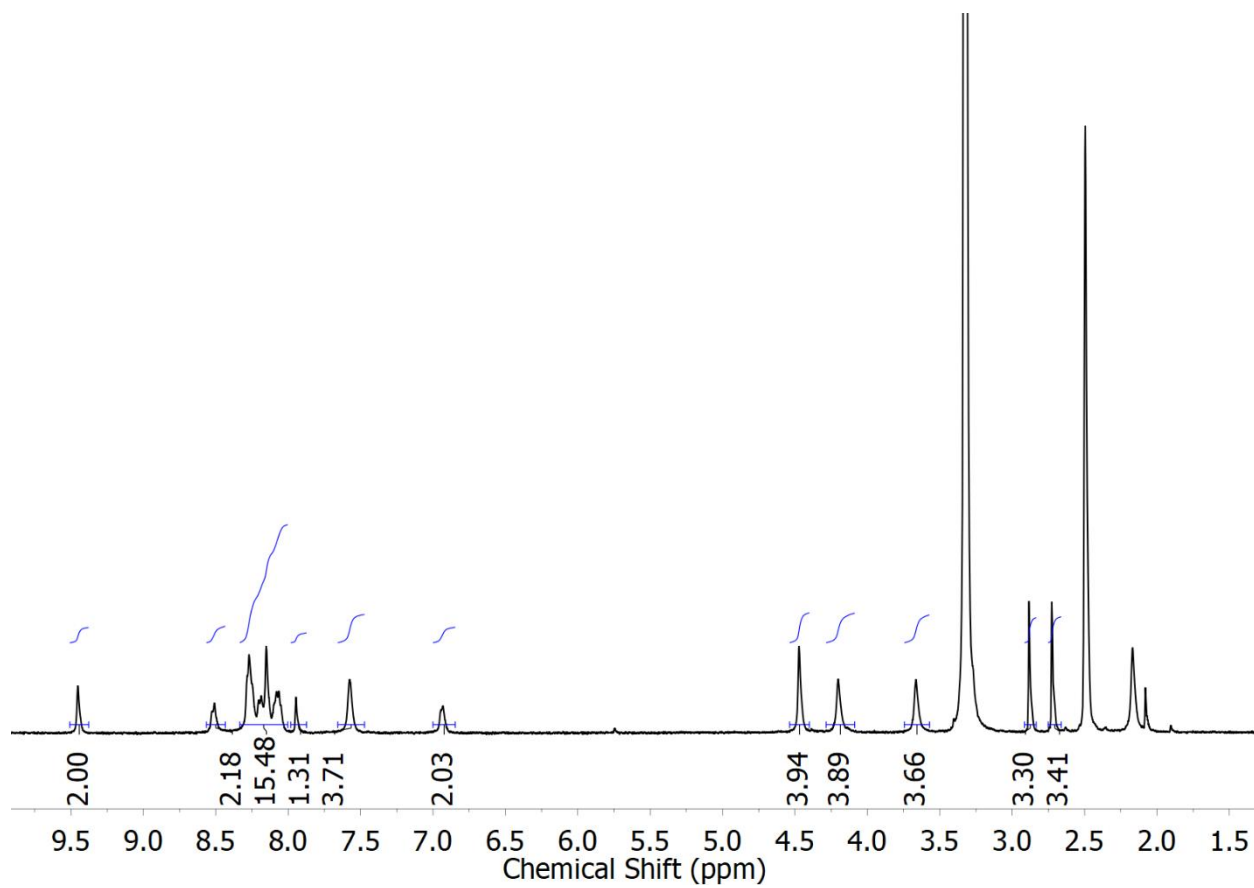
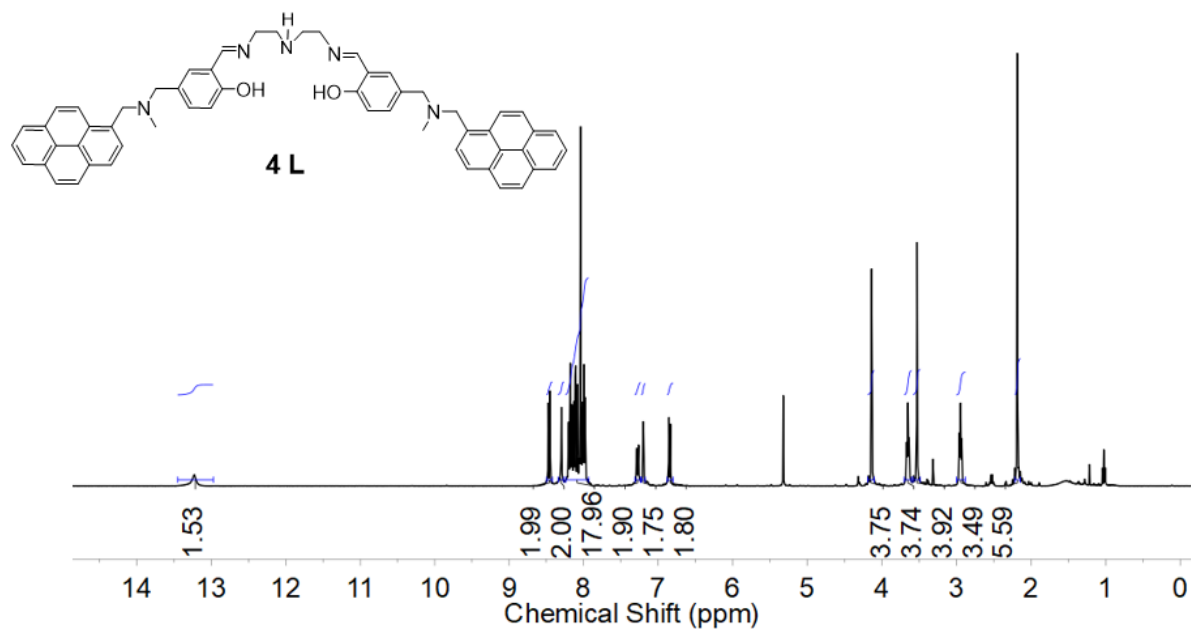**Figure B7**. 500 MHz ^{1}H NMR spectrum of **2-U** in d_6-DMSO.
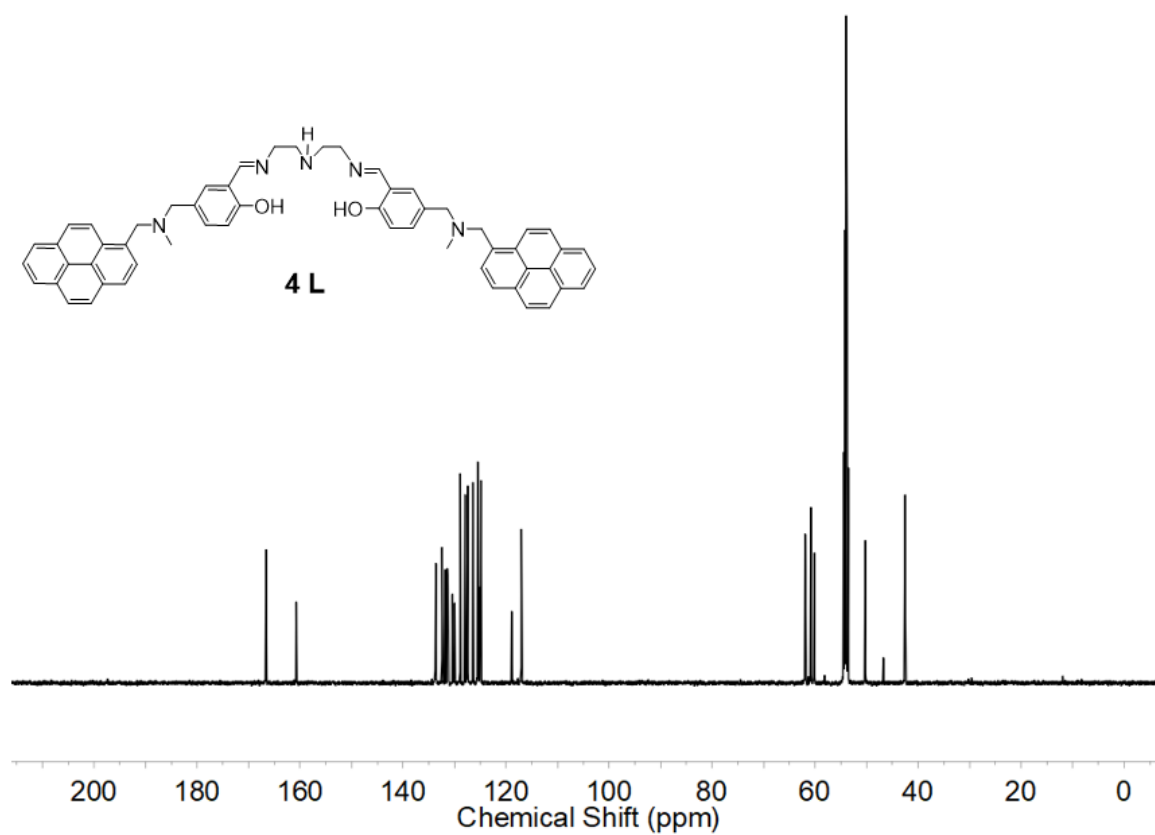
Figure B8. 400 MHz ^{1}H NMR spectrum of **4-L** in CD$_2$Cl$_2$.

Figure B9. 125 MHz ^{13}C NMR spectrum of **4-L** in CD$_2$Cl$_2$.
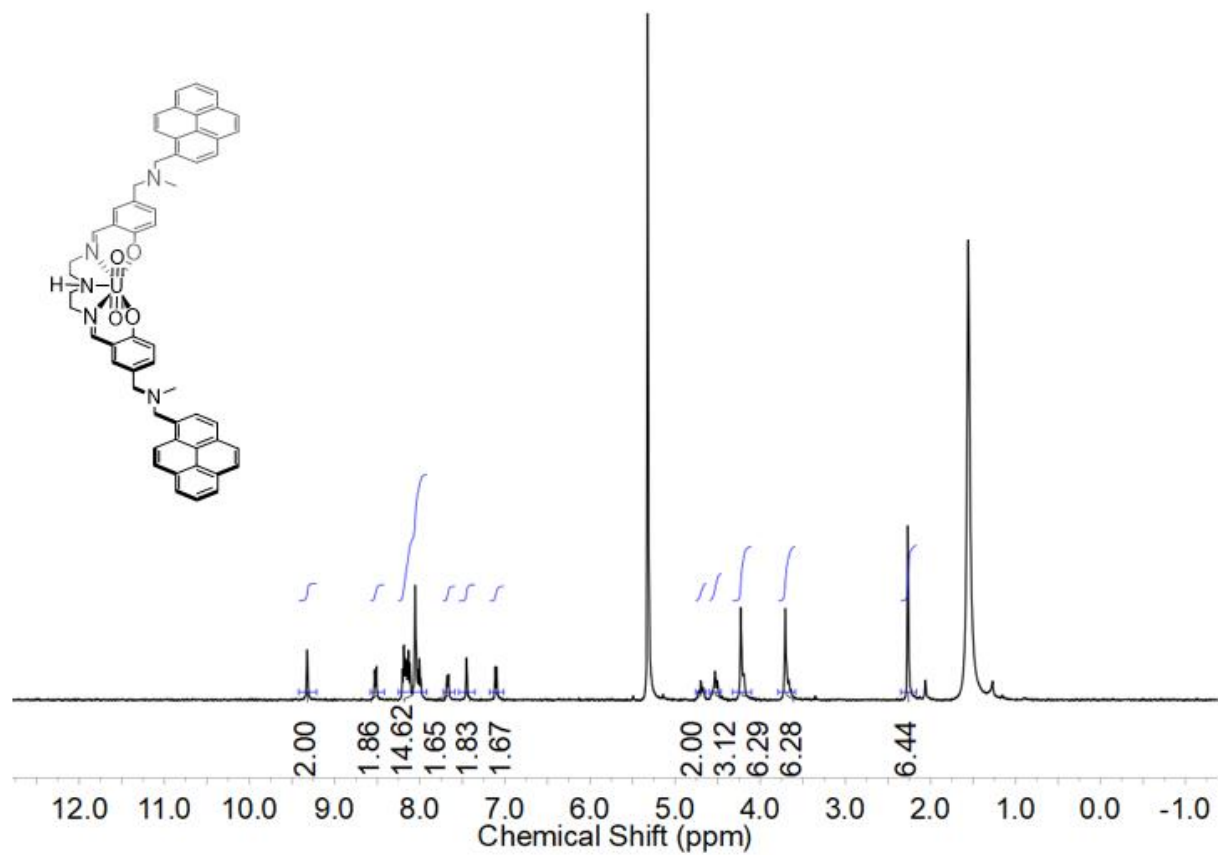
Figure B10. 500 MHz ^{1}H NMR spectrum of **4-U** in CD$_2$Cl$_2$.

B.4. *References*

1. Fennie, M. W.; DiMauro, E. F.; O'Brien, E. M.; Annamalai, V.; Kozlowski, M. C., *Tetrahedron* **2005,** *61*, 6249-6265.

2. Chirakul, P.; Hampton, P. D.; Bencze, Z., *J. Org. Chem.* **2000,** *65*, 8297-8300.

3. Takao, K.; Kato, M.; Takao, S.; Nagasawa, A.; Bernhard, G.; Hennig, C.; Ikeda, Y., *Inorg. Chem.* **2010,** *49*, 2349-2359.

4. Asadi, Z.; Shorkaei, M. R., *Spectrochim. Acta A* **2013,** *105*, 344-351.

5. Evans, D. J.; Junk, P. C.; Smith, M. K., *Polyhedron* **2002,** *21*, 2421-2431.